Atom-by-Atom Assembly and Investigation of Small Fe Clusters with High-Resolution Atomic Force Microscopy

Dissertation zur Erlangung des Doktorgrades der Naturwissenschaften (Dr. rer. nat.) der Fakultät für Physik der Universität Regensburg

vorgelegt von

Julian Berwanger

aus München

im Jahr 2019

Das Promotionsgesuch wurde am 25. November 2019 eingereicht.
Die Arbeit wurde von Prof. Dr. Franz J. Gießibl angeleitet.

Prüfungsausschuss:

Vorsitzender:	Prof. Dr. Klaus Richter
Erstgutachter:	Prof. Dr. Franz J. Gießibl
Zweitgutachter:	Prof. Dr. Rupert Huber
weiterer Prüfer:	Prof. Dr. Christian Schüller

Das Promotionskolloquium fand am 21. Februar 2020 statt.

Contents

1. Introduction

The invention of scanning tunneling microscopy (STM) [1, 2] and atomic force microscopy (AFM) [3] enabled investigations of electrically conducting and isolating surfaces in real space with atomic resolution. Both techniques allow probing the surfaces in a non-destructive manner. STM fulfills contact-free probing of the sample surface by definition. The introduction of non-contact AFM (nc-AFM) [4] and the development of a quartz-based force sensor [5] which prevents jump-to-contact due to its high stiffness are key to facilitate AFM studies in the contactless and intermediate distance regime.

A couple of years after the invention of STM, the very first atomic positioning experiments using single Xe atoms on Ni(110) were conducted by Eigler and Schweizer [6]. Thereafter, atomic manipulation became a widely used technique and different manipulation modes were investigated [7, 8]. Afterwards, continuous lateral manipulation of single atoms (i.e. Co atoms) allowed imaging the Cu(111) surface including its hcp and fcc hollow sites with atomic resolution [9] and mapping the magnetic order of Mn/W(110) on the atomic scale [10]. Celotta *et al.* presented an autonomous atom assembler which allows creating pre-defined nanostructures automatically using lateral manipulation in STM at low temperatures [11]. This technique was extended to liquid nitrogen temperatures ($T = 77\,\mathrm{K}$) by atomically manipulating chlorine vacancies on the Cu(100) surface which allows writing down a passage from Feynman's lecture *There's Plenty of Room at the Bottom* [12]. Ternes *et al.* [13] applied simultaneous STM/AFM to measure the lateral force thresholds to manipulate single atoms and molecules on the Cu(111) surface. Furthermore quantum corrals [14–16], logical operators [17] and nanomagnets [18] were created by arranging individual Fe atoms on Cu(111) in a specific order. Hereby, the magnetic properties of compact Fe clusters and nanoislands on Cu(111) [19] could be used in spin-based technologies in the future [20–22]. However, the atomic structure of the artificially created nanomagnets which is highly relevant for the magnetic properties

was inaccessible due to the use of metal tips [20]. Hence, the combination of lateral manipulation with the ability to resolve artificially created nanostructures on the atomic scale is missing, so far.

Furthermore, Fe is an essential catalytic material which is frequently utilized in nature as a bio-catalyst and, thus, is very important in organic synthesis [23, 24]. Here, Fe has the advantage that it is relatively non-toxic, affordable, abundantly available and sustainable compared to many transition metals [23, 25]. So far, the catalytic properties of Fe clusters were mainly studied in the gas phase [26–28] and only as a function of the cluster size [29]: Essentially, the rate of catalytic events or chemical reactions increases with cluster size, i.e. the number of Fe atoms in the investigated cluster. However, none of the studies were able to determine the chemical reactivity, i.e. the *active sites* [30] of small Fe clusters on the atomic scale.

The functionalization of the scanning tunneling microscope's [31] and atomic force microscope's [32] tip with a single CO molecule enabled atomic resolution on small Fe clusters [33], next to outstanding atomically resolved measurements on molecular systems [32, 34–36], two-dimensional materials [37, 38], ionic surfaces [39] and interfacial water [40, 41]. Moreover, it was shown that a CO-terminated tip (CO tip) transitions from physisorption to chemisorption when approaching the center of a single Fe adatom on the Cu(111) surface [42].

Within this thesis, the high-resolution capability of CO tips on small Fe clusters is combined with lateral manipulation in order to atom-by-atom assemble small Fe clusters with atomic precision. Furthermore, the chemical reactivity of the created Fe clusters is studied on the atomic scale by using the ability of CO tips of forming a chemical bond with single Fe adatoms at close distances.

The remainder of this thesis is structured as follows. In chapter 2, the basic concepts of STM and AFM and their operating principles are introduced. Additionally, the simultaneous operation of STM and frequency modulation AFM (FM-AFM) [4], including the different imaging modes, are described within this chapter.

Chapter 3 starts with a description of the custom-built low temperature STM/FM-AFM that is used to conduct all experiments. Afterwards, the sample preparation and the quartz-based force sensor including the preparation and functionalization of its tip are presented.

In chapter 4, the lateral manipulation of single Fe adatoms with monoatomic metal and CO-terminated monoatomic metal tips is described. Here, the lateral manipulation mechanism is studied in detail and the manipulation behavior of the two different types of tips is investigated. Additionally, an analytic model describing the experimental observations including the influence of small tip tilts is developed. At last, the lateral manipulation capability of CO tips is combined with their ability to resolve small Fe clusters on the atomic scale by assembling small Fe clusters atom by atom with atomic precision.

The combination of the high-resolution capability of CO tips with their property of transitioning from physi- to chemisorption when approaching the center of a single Fe adatom [42] is utilized in the fifth chapter: This chapter investigates the chemical reactivity of small, atom-by-atom assembled Fe clusters on the atomic scale and, furthermore, the physical origin of the atomic contrast of small Fe clusters in AFM using CO tips. In a final step, changes in the appearance of small Fe clusters over time are attributed to the adsorption of hydrogen on the clusters.

To conclude, chapter 6 summarizes all the results of this thesis.

2. Fundamentals of Scanning Tunneling and Atomic Force Microscopy

This chapter discusses the basic principles of STM (section 2.1) and AFM (section 2.2). Section 2.3 describes the simultaneous operation of STM and AFM including various imaging modes and the determination of the relative and absolute tip-sample distances.

2.1. Scanning Tunneling Microscopy

The scanning tunneling microscope was realized by Binnig *et al.* in 1982 [43] and established itself as one of the most important tools to atomically resolve electrical conducting surfaces in real space. The basic mechanism in STM is quantum mechanical tunneling of electrons through a potential barrier (e.g. a vacuum gap) between a sharp metallic tip and an electrically conducting sample [1] (see Fig. 2.1). If the metal tip is positioned few hundreds of picometers apart of an electric conducting sample and a small bias voltage V is applied between tip and sample, classically electrons cannot overcome the potential barrier Φ_t and, hence, no classical ohmic current can be detected. However, if the tip is close enough so that the wave functions of tip and sample overlap, electrons can tunnel through the vacuum gap from tip to sample and vice versa. At $V = 0$ the net tunneling current will be zero. As long as $V \neq 0$, the quantum mechanical tunneling of electrons leads to a non-zero tunneling direct current I between tip and sample (see Fig. 2.1(a)). Applying the bias voltage V to the tip and by grounding the sample increases the quasi Fermi level of the tip, $E_{\mathrm{F,t}}$, by eV compared to $E_{\mathrm{F,s}}$. Hence, electrons will tunnel from

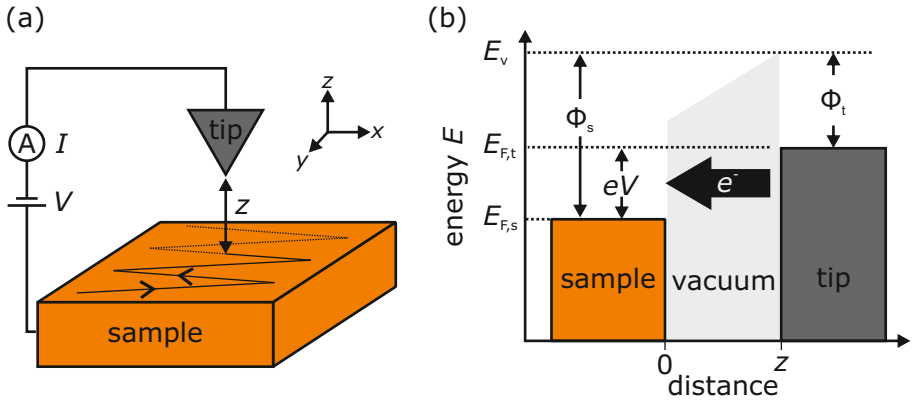

Figure 2.1. (a) In STM, a sharp metal tip is positioned few hundreds of picometer apart from an electrical conducting sample. Classically, no electron can overcome the potential barrier between tip and sample. However, in quantum mechanics, electrons can tunnel through the vacuum gap. As long as a bias voltage $V \neq 0$ between tip and sample is applied, a tunneling current I can be measured. By moving the tip in the xy plane across the sample, the lateral dependent tunneling current can be recorded. (b) By applying a bias voltage V between tip and sample, the quasi Fermi levels of the tip $E_{\mathrm{F,t}}$ and sample $E_{\mathrm{F,s}}$ are shifting with respect to each other. Throughout this work, the bias voltage V is applied to the tip and is labeled as V_{tip} in chapters 3 to 5. Hence, if a negative bias voltage V is applied to the tip, electrons will tunnel from occupied states of the tip into unoccupied states of the sample. In panel (b), it is assumed that the materials of tip and sample are identical (i.e. $\Phi_{\mathrm{s}} = \Phi_{\mathrm{t}}$). The vacuum energy E_{V} is used as reference point.

occupied states of the tip into unoccupied states of the sample (see Fig. 2.1(b)). By reversing the polarity of the bias voltage V the unoccupied states of the tip can be accessed as well [1, 44, 45].

An exponential distance dependence of the tunneling current I can be found by solving the time-independent Schrödinger equation in one dimension using a rectangular potential barrier of $\Phi = \frac{\Phi_{\mathrm{t}}+\Phi_{\mathrm{s}}}{2}$ (while $eV \ll \Phi$) [1]:

$$I(z) = I_0 \exp\left(-2\kappa z\right) \quad \text{with} \quad \kappa = \sqrt{2m_{\mathrm{e}}\Phi/\hbar^2} \tag{2.1}$$

Hereby, m_{e} is the mass of a free electron, $\hbar$ is the Planck constant, κ refers to a material dependent decay constant and I_0 describes the current at point contact. Within this work, the sample and tip material mainly consists of Cu, which possesses a work function of $\Phi = 5.0\,\mathrm{eV}$ (for the (111)-plane) [46]. This results in a value of $\kappa = 1.1 \cdot 10^{10}\,\mathrm{m}^{-1}$, yielding a drop of the tunneling current by one order of magnitude

when reducing the tip-sample distance z by the atomic radius of Cu $r_{\mathrm{Cu}} = 135\,\mathrm{pm}$. This high vertical sensitivity of the tunneling current is responsible for the atomic resolution capability of STM.

However, the approach described above does not take the wave character of tip and sample into account. Tersoff and Hamann assume s type wave functions for describing the STM tip[1] and use the matrix element for quantum mechanical tunneling of electrons [47]. Thereby, an expression of the tunneling current which includes the local density of states (LDOS) of tip ρ_{t} and sample ρ_{s} at the Fermi level at the location $\vec{r_0}$ can be derived [48, 49]:

$$I \propto V \cdot \rho_{\mathrm{t}}\left(E_{\mathrm{F}}\right) \cdot \rho_{\mathrm{s}}\left(\vec{r_0}, E_{\mathrm{F}}\right) \tag{2.2}$$

Using metal tips, STM mainly images the LDOS of the sample, since the DOS of s type tips do not change significantly within the energy range of E_{F} and $E_{\mathrm{F}} + eV$ [48]. Moreover, the electron tunneling through non-metallic tips (e.g. CO tips [50]), can be described by further considering the p and d type states of the tip [51, 52].

2.2. Atomic Force Microscopy

In 1986, Binnig, Quate and Gerber introduced AFM. With this technique atomic forces acting between a sharp tip mounted on a cantilever and a sample can be probed [3]. While STM is limited in probing electrically conductive surfaces, AFM allows investigating both electrically conductive and non-conductive samples and, hence, AFM has established itself in research and industry. The forces acting between tip and sample can be classified in long-range and short-range forces.

2.2.1. Long-Range Forces

Long-range forces possess decay lengths in the order of nanometers and do typically not enable atomic resolution in AFM. In ultra-high vacuum (UHV) conditions, long-range forces consist of van-der-Waals (vdW) and electrostatic forces.

[1] This is in general sufficient for metal tips.

Van-der-Waals Force The vdW interaction, which invariably leads to attraction, mainly consists of the dispersion force for non-polar or weakly polar atoms and molecules. The attractive force is a result of dipole-dipole interactions on the atomic or molecular scale: Spontaneous fluctuations of the dipole moment of an atom or molecule lead to a non-permanent dipole moment whose electric field induces a second dipole in another atom or molecule. This leads to electrostatic attraction between the spontaneous and induced dipole. The corresponding distance-dependent vdW potential U_{vdW} and the vdW force F_{vdW} between two atoms are given by [53]:

$$U_{\mathrm{vdW}}(z) = -\frac{C_6}{z^6} \tag{2.3}$$

$$F_{\mathrm{vdW}}(z) = -\frac{\partial U_{\mathrm{vdW}}(z)}{\partial z} = -\frac{6C_6}{z^7} \tag{2.4}$$

Here, C_6 is an elemental-specific constant which depends on the atomic species of the two interacting atoms. It can be calculated for various atomic combinations [54]. In order to determine the total vdW interaction between tip and sample, either pairwise summation between each tip and sample atom needs to be done (see e.g. chapter 4) or the exact geometry of the tip can be used to determine the analytic vdW potential $U_{\mathrm{vdW}}(z)$ by describing the sample by a semi-infinite space and integrating over the tip volume [55]. Taking the exact shape of the tip into account, the power law of the short-range force in equation 2.4 ($\propto 1/z^7$) turns long-range (pyramidal and conical tips $F_{\mathrm{vdW}} \propto 1/z$, parabolic tips $F_{\mathrm{vdW}} \propto 1/z^2$ [56]).

Electrostatic Force If tip and sample are electrically connected and their material differs, the difference in work function of tip Φ_{t} and sample Φ_{s} leads to a contact potential difference $V_{\mathrm{CPD}} = \Phi_{\mathrm{s}} - \Phi_{\mathrm{t}}$. Tip and sample can be described as a capacitor and its electrostatic potential $U_{\mathrm{es}}(z)$ and force $F_{\mathrm{es}}(z)$ is given by [57]

$$U_{\mathrm{es}}(z) = \frac{1}{2} C(z) \left(V_{\mathrm{CPD}} - V\right)^2 \tag{2.5}$$

$$F_{\mathrm{es}}(z) = -\frac{\partial U_{\mathrm{es}}}{\partial z} = -\frac{1}{2}\frac{\partial C(z)}{\partial z} \left(V_{\mathrm{CPD}} - V\right)^2 \tag{2.6}$$

while e is the elementary charge, V the applied bias voltage and $C(z)$ the distance-dependent capacitance of the capacitor. The long-range electrostatic force can be

compensated by applying a bias voltage of $V = V_{\mathrm{CPD}}$.

2.2.2. Short-Range Forces

Short-range forces between the tip's apex and the sample decay on length scales of tens or hundreds of picometer and are typically responsible for atomic resolution in AFM. Physical and chemical bonding forces and short-range electrostatic forces are the most important short-range forces.

Physical Bonding - Physisorption If two chemically inert atoms are positioned relatively far away from each other, they are attracted by the vdW force which increases with the power of 7 with decreasing distance z (see equation 2.4). However, at close distances, the Pauli exclusion principle becomes important. It states that two electrons must not possess the same quantum numbers, i.e. they can never occupy the same quantum mechanical state [58]. Hence, if two chemically inert atoms are close enough such that their orbitals overlap, a repulsive force arises leading to Pauli repulsion. The interplay between the attractive vdW interaction and repulsive Pauli repulsion can be described by the Lennard-Jones potential $U_{\mathrm{LJ}}(z)$ [59]:

$$U_{\mathrm{LJ}}(z) = -U_0 \left[2 \left(\frac{\sigma}{z} \right)^6 - \left(\frac{\sigma}{z} \right)^{12} \right] \tag{2.7}$$

Here, the repulsive part is expressed by an empirical $\left(\frac{\sigma}{z}\right)^{12}$ term. The corresponding force is given by $F_{\mathrm{LJ}}(z) = -\partial U_{\mathrm{LJ}}(z)/\partial z$. The binding energy U_0 is typically in the range of 1 meV to 10 meV such as for two CO molecules approaching each other [60].

Intramolecular resolution in AFM using CO tips mainly arises due to the Pauli repulsion between the tip's chemically inert O atom and the investigated molecular structure [61–63].

Chemical Bonding - Chemisorption If the atoms of the tip apex and the investigated sample atoms are not chemically inert, a chemical bond can form by approaching the tip towards the sample or sample's adsorbate. The chemical bond can be of covalent, metallic or ionic character. In covalent bonding, hybridization occurs upon overlapping of the atomic orbitals of two interaction partner and new bonding as well as anti-bonding atomic orbitals develop resulting in a chemical

bond. The distance dependence of the potential during covalent bond formation can be described by the semi-empirical Morse potential [64]

$$U_{\mathrm{M}}(z) = -U_b \left[2e^{-\frac{(z-\sigma)}{\lambda}} - e^{-\frac{(z-\sigma)}{\lambda/2}} \right] \tag{2.8}$$

with the equilibrium distance σ, the binding energy U_0 and the decay constants λ and $\lambda/2$ of the attractive and repulsive part of the interaction, respectively. In chemisorption, the binding energies U_0 can reach eV such as described for two Si atoms by the Stillinger-Weber potential [65]. Hence, the binding energies in chemisorption are typically much stronger as in the case of physisorption.

In metals, the metallic bonds are formed by sharing of the atoms' valence electrons throughout the solid resulting in the appearance of nearly free electrons which are distributed over the whole crystal. In ionic bonds, the electrostatic attraction between anions and cations is competing against the Pauli repulsion at small distances, leading to an equilibrium bonding distance.

Throughout this thesis, single Fe adatoms or small Fe clusters adsorbed on Cu(111) are investigated. To simplify the analysis and enhance comparability between different tips, the long-range force contributions are removed. This is achieved by acquiring the interaction on the bare Cu(111) surface and the investigated adsorbate subsequently. Assuming additivity, the contribution on the bare Cu(111) surface can be subtracted from the interaction on the adsorbate such that only the short-range contribution between tip and adsorbate remains (see also subsection 2.3.3).

Besides the above discussed forces, various other force contributions exist (see e.g. Ref. [66–69]). However, they are not relevant in the context of this thesis.

2.2.3. Frequency-Modulation Atomic Force Microscopy

AFM can be performed in different modes. In the static mode, the force F_{ts} between tip and sample leads to a static deflection s of the cantilever with stiffness k. The force can be retrieved by measuring the static deflection s and by using $F_{\mathrm{ts}} = ks$. Throughout this work, AFM is conducted in a dynamic mode, where the tip-sample

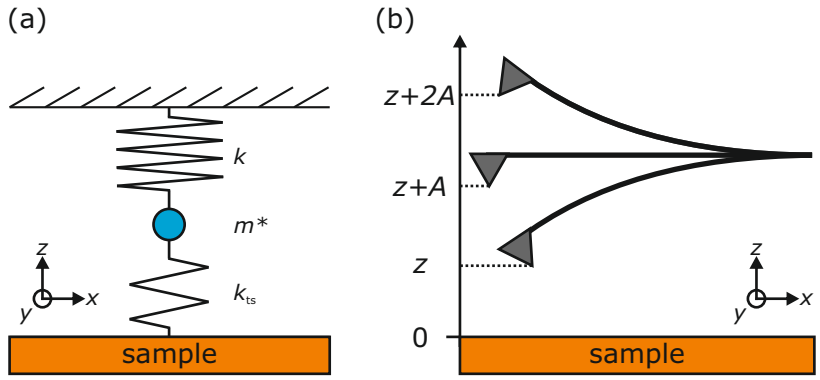

Figure 2.2. (a) Corresponding mass and spring model for FM-AFM. A cantilever with effective mass m^* and stiffness k is oscillating above a sample surface. The tip-sample force F_{ts} and its corresponding force gradient $k_{\mathrm{ts}}(z) = -\partial F_{\mathrm{ts}}(z)/\partial z$ induces a change of the eigenfrequency f_0 of the driven harmonic oscillator. (b) In FM-AFM, a sharp tip, mounted on a cantilever, oscillates with constant amplitude A above a surface. The lower and upper turnaround points are given by z and $z+2A$, respectively.

force F_{ts} is measured indirectly via the frequency shift Δf. In frequency-modulation atomic force microscopy (FM-AFM) [4], the cantilever oscillates at its resonance frequency f with constant amplitude A. A feedback loop is used to obtain a constant amplitude A which excites the cantilever phase-shifted by 90° to its oscillation (see subsection 3.3). In the absence of any tip-sample interaction, the oscillation of the cantilever can be described as a driven, damped harmonic oscillator with an eigenfrequency f_0 which is given by:

$$f_0 = \frac{1}{2\pi}\sqrt{\frac{k}{m^*}} \tag{2.9}$$

Here, m^* is the effective mass of the cantilever and k its stiffness. If the tip is separated by the distance z from the sample, a force between tip and sample F_{ts} is present. The corresponding force gradient $k_{\mathrm{ts}}(z)$ is given by $k_{\mathrm{ts}}(z) = -\partial F_{\mathrm{ts}}(z)/\partial z$ (see Fig. 2.2(a)). Hence, the resonance frequency of the cantilever changes from the unperturbed eigenfrequency f_0 to

$$f = \frac{1}{2\pi}\sqrt{\frac{k + k_{\mathrm{ts}}}{m^*}}. \tag{2.10}$$

Atomic resolution is achieved in a distance regime where short-range forces are dominating (see subsection 2.2.2) and, hence, the force gradient k_{ts} is typically not constant over the oscillation cycle[1] from z to $z + 2A$ (see Fig. 2.2(b)). To cover this case, Giessibl derived, by using a Taylor expansion and applying the Hamilton-Jacobi formalism [56] (employing the tip-sample interaction potential $U_{\mathrm{ts}} \ll U$ as a small perturbation to the harmonic potential $U = kA^2/2$ of the cantilever), a formula describing the frequency shift Δf from the unperturbed resonance frequency f_0 of the cantilever [70]:

$$\Delta f\left(z\right) = \frac{f_0}{2k}\left\langle k_{\mathrm{ts}}\left(z\right)\right\rangle \tag{2.11}$$

Here, $\langle k_{\mathrm{ts}}\left(z\right)\rangle$ is the force gradient averaged over the oscillation cycle of the cantilever. It can be expressed by [70]:

$$\left\langle k_{\mathrm{sp}}\left(z\right)\right\rangle = \frac{2}{\pi A^2}\int_{-A}^{A} k_{\mathrm{ts}}\left(z + A - q\right)\sqrt{A^2 - q^2}\mathrm{d}q \tag{2.12}$$

Alternatively it can be written using the tip-sample force F_{ts} [70]:

$$\left\langle k_{\mathrm{sp}}\left(z\right)\right\rangle = \frac{2}{\pi A^2}\int_{-A}^{A} F_{\mathrm{ts}}\left(z + A - q\right)\frac{q}{\sqrt{A^2 - q^2}}\mathrm{d}q \tag{2.13}$$

To obtain the tip-sample force F_{ts} from the measured frequency shift Δf data, equation 2.13 needs to be inverted. For this purpose, various methods were developed [70–73]. Throughout this work, the deconvolution method proposed by Sader and Jarvis [74] is utilized based on a MATLAB[2] script introduced in Ref. [75]. The force deconvolution of F_{ts} using the Sader-Jarvis method can be a mathematical ill-posed problem if the amplitude of the cantilever lies within a critical amplitude range [76, 77]. A MATLAB script to test whether the chosen amplitude of the cantilever A lies within the potential ill-posed amplitude regime is presented and utilized in the PhD thesis of Huber [78]. A further restriction for the oscillation amplitude selection arises when considering the optimal signal-to-noise ratio (SNR). Throughout this work, the main focus lies on the investigation of short-range forces which possess decay lengths λ of tens and few hundreds of picometers. To maximize the SNR, it was found that the optimal ratio between amplitude A and decay length

[1] Oscillation amplitudes A used throughout this thesis lie in a range from 10 pm to 100 pm.
[2] The MathWorks Inc., MATLAB R2016b, Natick, MA, USA

λ, assuming an exponential decaying tip-sample force, is given by [79]:

$$A/\lambda \approx 1.55 \tag{2.14}$$

During the acquisition and analysis of the data presented in chapter 4, the occurrence of potentially ill-posed force deconvolution scenarios described in Refs. [76, 77] was still unknown and, therefore, not considered. Instead, an amplitude of $A = 50\,\mathrm{pm}$ was chosen. In the second part of this work (see chapter 5), the inflection point test according to Refs. [76–78] is conducted for all presented tip-sample force F_{ts} and corresponding energy $E_{\mathrm{ts}} = -\int F_{\mathrm{ts}}\mathrm{d}z$ data and the amplitude is chosen in a range of 10 pm to 100 pm depending on the output of the inflection point test.

2.3. Simultaneous Scanning Tunneling and Atomic Force Microscopy

Combining FM-AFM with STM enables a more detailed investigation of the tip and sample as both frequency shift Δf and tunneling current I data are accessible at the same time. However, as the tip is oscillating sinusoidally in z with $z = z + A\left(1 + \cos\left(2\pi f t\right)\right)$ for FM-AFM purposes, the tunneling current I varies in time t. The distance-dependent direct current $I\left(z\right)$ (see equation 2.1) in simultaneous STM/FM-AFM is a time-average over the oscillation cycle of the tip and given by [66]:

$$\langle I\left(z\right)\rangle = I_0 \exp\left(-2\kappa z\right) \exp\left(-2\kappa A\right) \mathrm{I}_0\left(2\kappa A\right) \tag{2.15}$$

Here, $\mathrm{I}_0\left(x\right)$ is the modified Bessel function of the first kind. To obtain a bias voltage V independent measure, it is suitable to define the tunneling conductance $\langle G\rangle = \langle I\rangle / V$ which is a time-average over the oscillation cycle of the tip. The tunneling conductance $\langle G\rangle$ is then given by [66, 67]:

$$\begin{aligned} \langle G\left(z\right)\rangle &= \frac{\langle I\left(z\right)\rangle}{V} \overset{(2.15)}{=} \frac{I_0}{V} \exp\left(-2\kappa z\right) \exp\left(-2\kappa A\right) \mathrm{I}_0\left(2\kappa A\right) \\ &= G_0 \exp\left(-2\kappa z\right) \exp\left(-2\kappa A\right) \mathrm{I}_0\left(2\kappa A\right) \end{aligned} \tag{2.16}$$

Here, $G_0 = 2e^2/h = \left(12906\,\Omega\right)^{-1}$ is the conductance at point contact [13, 67].

2.3.1. Determination of the Relative and Absolute Tip-Sample Distance

The distance between tip and sample can be described in a relative and absolute manner. In combined STM/FM-AFM, the absolute tip-sample distance d can be determined by combining either the tunneling conductance $G(z)$ or the frequency shift $\Delta f(z)$ signal with Density Functional Theory (DFT)-based calculations.

The tunneling conductance $G(z)$ decays exponentially with the relative tip-sample distance z while at $z = 0$, the conductance at point contact G_0 is present. In experiment, the time-averaged conductance $\langle G \rangle$ is measured. In order to determine the relative distance z of the lower turnaround point of the sensor's oscillation to the reference point defined by the conductance at point contact (see Fig. 2.2(b)), the non-averaged conductance $G(z)$ at the lower turnaround point z needs to be derived. This is achieved by re-arranging equation 2.16:

$$G(z) = \frac{\langle G(z) \rangle}{\exp(-2\kappa A)\, \mathrm{I}_0(2\kappa A)} = G_0 \exp(-2\kappa z) \tag{2.17}$$

In case of monoatomic metal tips[1] G_0 is given by the single-channel, spin-degenerated quantum conductance $G_0 = 2e^2/h = (12906\,\Omega)^{-1}$ [13, 67]. If a monoatomic metal tip is terminated with a single CO molecule, the conductance at point contact (i.e. $z = 0$) shrinks to $G_0^{\mathrm{CO}} = (404497\,\Omega)^{-1}$ [81]. Using equation 2.17 the relative tip-sample distance z can be determined for both types of tips. Gustafsson *et al.* [80] found that, in case of a monoatomic metal tip experiencing a conductance of $G(z = 0) = G_0$ above the Cu(111) surface, the shell of the frontmost atom is still separated by $\Delta = \Delta_{\mathrm{DFT}} = 172\,\mathrm{pm}$ from the shell of a Cu atom of the topmost layer (see Fig. 2.3(a)). The same holds true for CO-terminated monoatomic metal tips [82] (see Fig. 2.3(b)). Applying this knowledge and measuring the decay length κ of the conductance curve $G(z)$ allows determining absolute distances d between e.g. the center of the tip's frontmost O atom and the center of a single Fe atom adsorbed on the Cu(111) surface [82]: The decay length κ and the relative tip-sample distance z can be determined by fitting equation 2.17 to a conductance versus distance $G(z)$ curve (see also subsection 2.3.3). DFT-based calculations

[1] Monoatomic metal tips are metal tips which are terminated by a single metal atom.

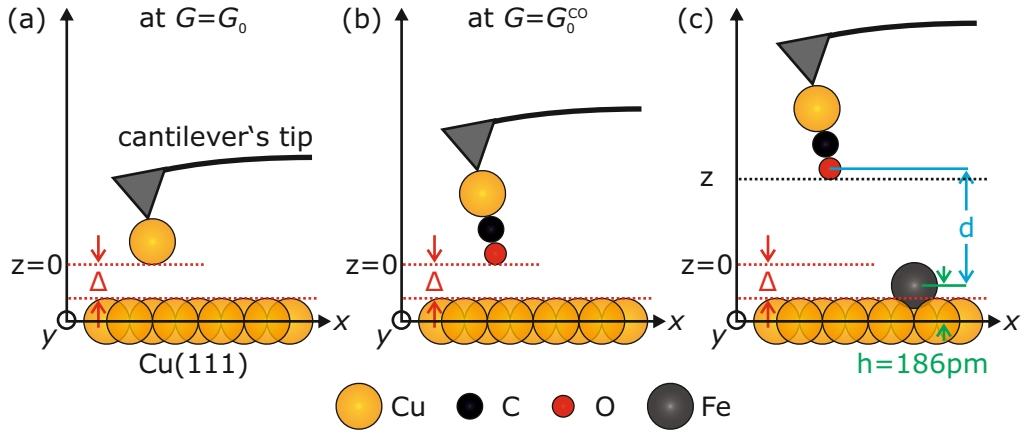

Figure 2.3. The cantilever including its tip is shown at its lower turnaround point z for three different cases. (a) If a monoatomic metal tip experiences a conductance of $G\,(z=0) = G_0 = 2e^2/h = (12906\,\Omega)^{-1}$ at $z = 0$, the shell of the frontmost atom is not touching the shell of an atom of the topmost Cu(111) layer [80]. (b) The same holds true for CO-terminated tips [42, 78], while the conductance G at $z = 0$ is only $G = G_0^{\mathrm{CO}} = (404497\,\Omega)^{-1}$ [81]. (c) Using the atomic radii of Cu ($r_{\mathrm{Cu}} = 135\,\mathrm{pm}$), O ($r_{\mathrm{O}} = 60\,\mathrm{pm}$) and the adsorption height h of the adsorbate, the absolute core-core distance d between the tip's O atom and e.g. a Fe adatom in dependence of z can be obtained [42, 82]. The cantilever and its tip are not sketched to scale.

resulted in an adsorption height h of the Fe adatom of 186 pm [83]. Using the atomic radii of Cu ($r_{\mathrm{Cu}} = 135\,\mathrm{pm}$) and O ($r_{\mathrm{Cu}} = 60\,\mathrm{pm}$) allows linking the core-core distance d between the tip's O atom and the Fe adatom with the relative tip-sample distance z:

$$z\,(d) = d - \Delta_{\mathrm{DFT}} - r_{\mathrm{Cu}} - r_{\mathrm{O}} + h = d - 181\,\mathrm{pm} \tag{2.18}$$

This relation is used to align the vertical distance between experiment and theory in chapter 4 in order to be consistent with Ref. [82].

Alternatively, FM-AFM can be used to determine absolute tip-sample distances. References [42, 78] describe a method which is based on the experimental measurement of the equilibrium distance σ between a CO molecule adsorbed on the Cu(111) surface and a CO molecule adsorbed on the tip [60], determined via force spectroscopy (see subsection 2.3.3). By using the equilibrium distance σ and taking into account the adsorption height of the CO molecule on the surface [84], the absolute distance between the tip's frontmost O atom and the Cu(111) surface can be calculated [42, 78]. By linking the absolute distance to the tunneling conductance above the

bare Cu(111) surface a reduced Δ value of $\Delta_{\mathrm{CO-CO}} = 48\,\mathrm{pm}$ compared to the STM and DFT-based result is obtained. This leads to a $z(d)$ relation which depends on the adsorption height h of:

$$z\,(d) = d + h - \Delta_{\mathrm{CO-CO}} - r_{\mathrm{Cu}} - r_{\mathrm{O}} = d + h - 243\,\mathrm{pm} \tag{2.19}$$

This $z\,(d)$ relation is used in chapter 5 in order to enable the comparison with the experimental and theoretical results described in Ref. [42].

2.3.2. Two-Dimensional Imaging Modes

So far, the tip's lateral position (x, y) was considered to be fixed. By scanning the tip laterally across the surface, the lateral dependencies of the measures can be studied. In combined STM/FM-AFM, this can be done in three different modes. Either, the tip is moved in constant-height across the surface and the frequency shift $\Delta f\,(x, y, z = \mathrm{const.})$ and conductance $\langle G\,(x, y, z = \mathrm{const.})\rangle$ is recorded simultaneously or a certain conductance setpoint $\langle G_{\mathrm{set}}\rangle$ (i.e. a tunneling current $\langle I_{\mathrm{set}}\rangle$ and a bias voltage V setpoint) or frequency shift setpoint Δf_{set}, respectively, can be used as an input parameter of a feedback loop controlling the tip's z position. Within this work, the constant-height mode and the constant-current mode (i.e. constant conductance setpoint $\langle G_{\mathrm{set}}\rangle$) are used.

Constant-Height Mode

In constant-height mode, the tip's vertical position z is fixed ($z = \mathrm{const.}$) and the tip is scanned laterally across the sample surface. Therefore, lateral variations of $\langle G\,(x, y, z = \mathrm{const.})\rangle$ and $\Delta f\,(x, y, z = \mathrm{const.})$ can be obtained. Using the constant-height mode excludes any potential influence of the z feedback loop (such as noise introduction) and, additionally, allows measuring the tunneling conductance $\langle G\rangle$ and the frequency shift Δf independent[1] from each other. On the other hand, this mode should only be used if the topography of the sample surface is known and if it is relatively flat. Otherwise, the tip can accidentally crash into local (unknown) protrusions.

[1] This holds true as long as crosstalk is suppressed by limiting the tunneling current [85, 86].

Constant-Current Mode

The monotonic behavior of the tunneling conductance $\langle G \rangle = \langle I \rangle / V$ with respect to the tip-sample distance z (see equation 2.16) allows controlling the tip's vertical position z with a feedback loop by using a pre-defined conductance setpoint $\langle G_{\mathrm{set}} \rangle = \langle I_{\mathrm{set}} \rangle / V$ as an input parameter. This method is called constant-current mode. By scanning the tip laterally across the sample surface, a topographic map $z(x, y)$ of constant conductance $\langle G_{\mathrm{set}} \rangle$ which is proportional to the LDOS of the sample and tip (see equation 2.2) can be acquired. Using the constant-current mode allows e.g. resolving in the simultaneously recorded $\Delta f(x, y, z)$ images small Fe clusters adsorbed on Cu(111) and the Cu(111) substrate on the atomic scale at the same time [33]. However, the $\Delta f(x, y, z)$ images are directly influenced by the active control of the z position via the feedback loop [87]. By acquiring the $\Delta f(x, y, z)$ images at different conductance setpoints $\langle G_{\mathrm{set}} \rangle$, maps of constant frequency shift Δf or constant z positions can be extracted manually afterwards [88].

2.3.3. Tip-Sample Distance Spectroscopy

In z spectroscopy, the tip is positioned at a fixed lateral position (x, y) and the tip-sample distance z is varied. This leads to the acquisition of conductance $\langle G(z) \rangle$ and frequency shift $\Delta f(z)$ versus distance z curves. By fitting equation 2.16 to the $\langle G(z) \rangle$ curve, the decay constant κ and the tip-sample distance z can be determined. The corresponding vertical short-range force curve $F_{z,\mathrm{SR}}(z)$ between an adsorbate and the tip can be received as follows by acquiring two $\Delta f(z)$ curves in FM-AFM: After recording a $\Delta f_{\mathrm{on}}(z)$ curve above the adsorbate of interest and a $\Delta f_{\mathrm{off}}(z)$ curve above the bare Cu(111) surface in the same z range the *so-called* short-range frequency shift curve ($\Delta f_{\mathrm{SR}}(z) = \Delta f_{\mathrm{on}}(z) - \Delta f_{\mathrm{on}}(z)$) can be derived. Subsequently, the vertical short-range force $F_{z,\mathrm{SR}}(z)$ curve can be deconvoluted by using e.g. the Sader-Jarvis method [74, 76, 77]. When using the Sader-Jarvis method, it is necessary that $\Delta f_{\mathrm{SR}}(z_{\max}) = 0$ for the furthest distance $z = z_{\max}$. Finally, the short-range potential $U_{\mathrm{SR}}(z) = -\int F_{z,\mathrm{SR}}(z)\,\mathrm{d}z$ can be calculated by integrating $F_{z,\mathrm{SR}}(z)$.

2.3.4. Three-Dimensional Imaging: Determination of Short-Range Vertical Forces, Short-Range Potentials and Lateral Forces

The constant-height mode allows acquiring a three-dimensional data set of the frequency shift ($\Delta f\left(x,y,z\right)$) through consecutively scanning the region of interest on the sample (e.g. an adsorbate on Cu(111)) while repeatedly incrementing the tip-sample distance z by e.g. 5 pm after each individual scan is finished. If the last acquired $\Delta f\left(x,y,z=z_{\mathrm{max}}\right)$ image at the largest distance $z=z_{\mathrm{max}}$ shows no contrast (i.e. no variation) anymore, the frequency shift value $\Delta f\left(z=\mathrm{const.}\right)$ averaged at the (x,y) positions above the substrate can be subtracted from each individual $\Delta f\left(x,y,z=\mathrm{const.}\right)$ image for all acquired z heights to obtain the short-range frequency shift cube $\Delta f_{\mathrm{SR}}\left(x,y,z\right)$. Afterwards, the three-dimensional vertical short-range force $F_{z,\mathrm{SR}}\left(x,y,z\right)$ can be deconvoluted using e.g. the Sader-Jarvis method [74, 76, 77]. The corresponding short-range interaction potential between tip and sample $U_{\mathrm{SR}}\left(x,y,z\right)$ can be determined by integrating the vertical short-range force $U_{\mathrm{SR}}\left(x,y,z\right)=-\int F_{z,\mathrm{SR}}\left(x,y,z\right)\mathrm{d}z$. Applying the lateral derivative to $U_{\mathrm{SR}}\left(x,y,z\right)$ allows deriving lateral forces e.g. in the x direction [13]:

$$F_{x}\left(x,y,z\right)=-\partial U_{\mathrm{SR}}\left(x,y,z\right)/\partial x. \tag{2.20}$$

3. Experimental Setup

This chapter describes the experimental setup of this work. All experimental data are recorded with a custom-built combined scanning tunneling and atomic force microscope operating in ultra-high vacuum (UHV) at low temperatures (LT) (see section 3.1). The machine consists of a preparation chamber and an analysis chamber. The purpose of the preparation chamber is the preparation of various samples such as the Cu(111) sample by Argon-sputtering and annealing (see section 3.2). The preparation chamber was designed by Schneiderbauer and is described in his PhD thesis [89]. The analysis chamber consists of a bath cryostat including an outer liquid nitrogen and an inner liquid helium tank and, in front of the bath cryostat, of a stage allowing the evaporation of single atoms on the cold sample. The base temperature of the microscope head which is mounted at the bottom part of the liquid helium tank is $T_{\mathrm{mic}} \approx 5.7\,\mathrm{K}$. The microscope head was originally designed and assembled by Emmrich (see PhD thesis [90]) and further optimized by Huber during his PhD thesis [78]. It is equipped with a qPlus sensor [5] which allows performing simultaneous STM and FM-AFM (see section 3.3). The tip preparation and functionalization is described in section 3.4.

3.1. Ultra-High Vacuum and Low Temperature Setup

Performing experiments at low temperatures in UHV conditions allows studying fundamental properties with minimal influence of external perturbations: In UHV conditions, sample surfaces can be studied, depending on their chemical reactivity, for days or weeks without any noticeable change of their surface termination. Conducting the measurements at liquid helium temperatures reduces the average thermal energy to $3/2 k_{\mathrm{B}} T_{\mathrm{mic}} = 0.74\,\mu\mathrm{eV}$, so that typically all adsorbates, except

hydrogen and helium, are immobilized[1]. Furthermore, thermal drift is minimized as most thermal expansion coefficients shrink with decreasing temperatures.

The analysis and preparation chamber which both operate at UHV conditions are linked by a gate valve which allows transferring samples and single atom evaporators from the preparation to the analysis chamber and vice versa without breaking the UHV. Samples and single atom evaporators can be introduced into the preparation chamber via an additional load lock which is attached to the preparation chamber. After closing the system, the initial UHV is generated with a turbo molecular pump while baking the system at $T \approx 140\,^{\circ}\mathrm{C}$ for approximately 48 hours. Once a pressure regime of about $1 \cdot 10^{-8}\,\mathrm{mbar}$ to $1 \cdot 10^{-7}\,\mathrm{mbar}$ is achieved, the ion getter pumps of the preparation and analysis chamber and the corresponding titanium sublimation pumps are switched on, the gate valve to the turbo molecular pump is closed and the turbo molecular pump is switched off. The resulting base pressure p_{base} ranges from $1 \cdot 10^{-10}\,\mathrm{mbar}$ to $1 \cdot 10^{-11}\,\mathrm{mbar}$. The microscope head is mounted at the bottom part of the liquid helium tank. To minimize radiative heating, an additional shield is mounted around the microscope head and is also fixed at the bottom part of the liquid helium tank. To further reduce the liquid helium consumption, another shield which covers the liquid helium shield is attached to the bottom part of the liquid nitrogen tank. The pressure within the shields of the cryostat ($\approx 10^{-15}\,\mathrm{mbar}$) is typically much lower than the base pressure within both chambers as most of the residual gas adsorbs on the cold shields. The temperature difference between the microscope ($T_{\mathrm{mic}} \approx 5.7\,\mathrm{K}$) and the boiling temperature of liquid Helium at ambient pressure ($4.15\,\mathrm{K}$) is mainly caused by the power dissipation of the internal AFM preamplifier which is also mounted at the bottom part of the liquid helium cryostat (see Ref. [91] for a detailed description of the used AFM preamplifier).

A more detailed description of the preparation and analysis chamber including the microscope head can be found in Refs. [89, 90].

3.2. Sample Preparation

All experiments presented in this work are conducted on the (111) surface of a single copper crystal. As copper is electrically conductive, simultaneous STM and

[1] This holds true as long as the corrugation of the surface potential is much bigger than the thermal energy of the adsorbates.

AFM can be conducted on its surface. Furthermore, the usage of copper as sample material allows reliably cleaning and sharpening the apex of the used tungsten tip on the atomic scale [92, 93] (see section 3.4). Cu(111) is a face-centered cubic (fcc) crystal and the distance between two nearest-neighbored layers along the [111] direction is $d_{111} = 208\,\text{pm}$ [94]. Single CO molecules adsorb on top positions on the hexagonal Cu(111) surface [31, 95, 96] (see Fig. 3.1(a)). When transferred to a monoatomic metal tip, the CO molecule also binds with its carbon atom to the tip's frontmost metal atom. Single Fe adatoms adsorb in fcc hollow sites[1] of Cu(111) [97, 98] as it is energetically more favorable than adsorption in hcp hollow sites by $\Delta E = 1.9\,\text{meV}$ [98] (see Fig. 3.1(b)). Each copper atom possesses six equivalent neighboring atoms at a distance of $a_{\text{NN}} = 255\,\text{pm}$ within the (111) planes [94].

The copper crystal is treated by repeated Ar^+ sputtering[2] and anneal[3] cycles in the preparation chamber in order to generate a clean Cu(111) surface with few defects. The sputtering results in the removal of several layers along the [111] direction while the annealing leads to almost defect-free large terraces of about $(100\,\text{nm})^2$. After transferring the prepared Cu(111) sample into the microscope

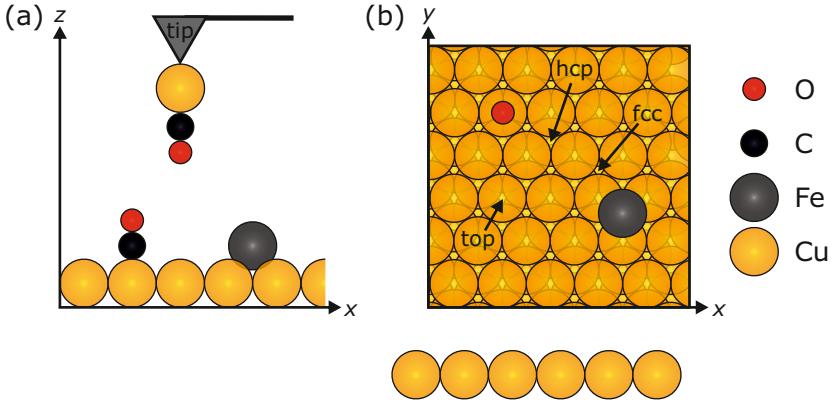

Figure 3.1. (a) Side view of the Cu(111) surface and a CO tip. CO molecules adsorb with their C atom on top sites on the Cu(111) surface and on the apexes of monoatomic metal tips [31, 95, 96]. Single Fe atoms adsorb on Cu(111) in fcc hollow sites [97, 98]. The cantilever and its tip are not sketched to scale. (b) The fcc, hcp and top sites are indicated in the top view of the Cu(111) surface, respectively.

[1] Adsorption in the fcc hollow sites follows the ABC stacking of Cu(111) while adsorption in a hcp hollow site would follow ABAB stacking.
[2] The kinetic energy of the Ar^+ ions is $E_{\text{kin}} = 1.2\,\text{keV}$.
[3] The annealing temperature is set to $T = 880\,\text{K}$.

head, about 0.005 to 0.01 monolayers (ML) of single CO molecules are dosed onto the cold sample by exposing it to a partial pressure of CO of $p_{\mathrm{CO}} = 2 \cdot 10^{-9}$mbar for about 1.5 min. The usage of a single CO molecule for tip characterization and functionalization will be discussed in section 3.4. Afterwards, single Fe adatoms are evaporated onto the cold surface by using a single atom evaporator (see also PhD thesis of Huber [78]). The single Fe atom evaporator consists of a 3 mm long Fe wire with a diameter of 1 mm which is placed inside a tungsten filament. By passing about 2.3 A to 3.0 A through the tungsten filament[1] and opening the doors of the liquid nitrogen and liquid helium shields for about 15 s, about 0.005 to 0.01 ML of Fe is evaporated on the Cu(111) surface. During the evaporation, the microscope temperature increases to about $T_{\mathrm{mic}} \approx 12$ K. If the evaporation time is extended, more Fe atoms are deposited and thermally activated self-assembly of small Fe clusters emerges [33, 90].

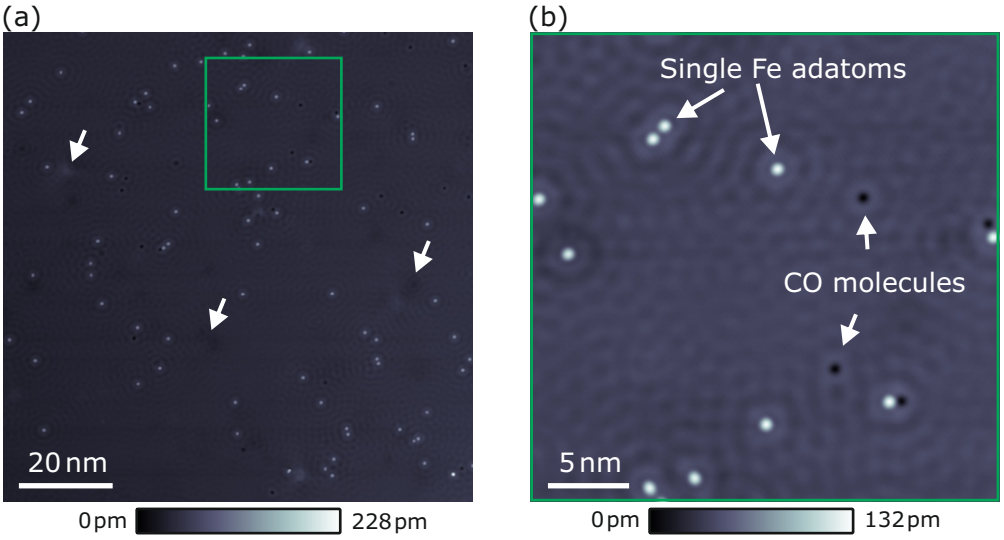

Figure 3.2. (a) The topographic image $z(x, y)$ shows the Cu(111) surface after dosing single CO molecules and evaporating single Fe adatoms onto the surface. The white arrows indicate remaining defects on the surface. (b) The zoomed $z(x, y)$ image (green square in panel (a)) shows individual Fe adatoms as protrusions (bright) and single CO molecules as depressions (dark). Both images were acquired in constant-current mode using a tunneling current setpoint of $\langle I_{\mathrm{set}} \rangle = 20$ pA, a bias voltage of $V_{\mathrm{tip}} = -20$ mV and a scan speed of 15 nm/s.

[1] The actual setpoint of the filament current strongly depends on the exact shape of the tungsten coil and needs to be determined experimentally.

Figure 3.2(a) shows a topographic image $z(x, y)$ of a 100 nm by 100 nm area of a Cu(111) surface after its preparation, including the dosing of single CO molecules and the evaporation of single Fe adatoms. The $z(x, y)$ image which was acquired in constant-current mode shows no step edges. The white arrows indicate remaining defects on the surface. The zoomed image (see Fig. 3.2(b)) shows single Fe adatoms and single CO molecules adsorbed on the Cu(111) surface. Single CO molecules appear in STM at small bias voltages as depressions (dark features), as the tunneling efficiency through the CO molecule is smaller compared to the bare Cu(111) surface [31]. Single Fe adatoms are imaged as protrusions (bright features) [14]. The Cu(111) surface possess at the Fermi level E_{F} a two-dimensional electron gas, which scatters at defects, adatoms and step edges. This leads to an interference pattern which is imaged in STM [99] (see Fig. 3.2(b)).

3.3. qPlus Sensor

The qPlus sensor, developed by Giessibl [5], allows performing simultaneous STM/FM-AFM. Since its invention it experienced different stages of evolution. The first qPlus sensor design is based on a standard quartz-based tuning fork which is also used in quartz-based watches. One of the two symmetric prongs is fixed to a substrate while the free oscillating prong is equipped with a sharp tip. Custom-designed and custom-built quartz sensors[1][2] feature an asymmetric layout of the two prongs, as the quality factor Q increases if the prong's mass which is later fixed to the substrate is much larger than the mass of the free oscillating prong. All different versions of the qPlus sensor, its detailed physical properties and many examples of its applications are described in Ref. [69]. One key advantage of the qPlus sensor is its variability with respect to the selection of the tip material: By choosing a non-conductive tip atomic resolution in ambient conditions on various sample systems is achieved using the pure AFM mode [68, 100]. Attaching a conductive, magnetic tip allows obtaining magnetic spin resolution without the need of applying an external magnetic field [101].

An optical photograph of the custom-built qPlus sensor used in this work is shown in Fig. 3.3. The qPlus sensor consists of an insulating ceramic plate with its

[1] Statek Corporation, Orange 92868, CA, USA
[2] Micro Crystal AG, CH-2540 Grenchen, Switzerland

mounting hole in the center for fixation in the microscope head (see Fig 3.3(a)). The custom-built tuning fork exhibits three electrodes which are used for the deflection detection and for the electrical connection of the tip. The custom-designed tuning fork is fixed with non-conductive glue[1] to the base plate (see orange colored glue indicated by black arrow in Fig. 3.3(a)). The glue should be located at the bottom left area between substrate and tuning fork. If the tuning fork is glued asymmetrically to the substrate by adding additional glue in the upper right part between tuning fork and substrate, experience has shown that it tends to crack during the cooldown from room to low temperature. The likely cause for the cracking are the different thermal expansion coefficients of quartz and ceramic. A crack could potentially cause side resonances that compromised the reliability of FM-AFM measurements. The electrical connections between the individual gold pads of the tuning fork and the conducting paths of the substrate are realized with electrical conductive glue[2] (see Fig. 3.3(b)). In case of the tip connection (gold pad C), an additional gold wire is required to enable the electrical connection. The current induced by the

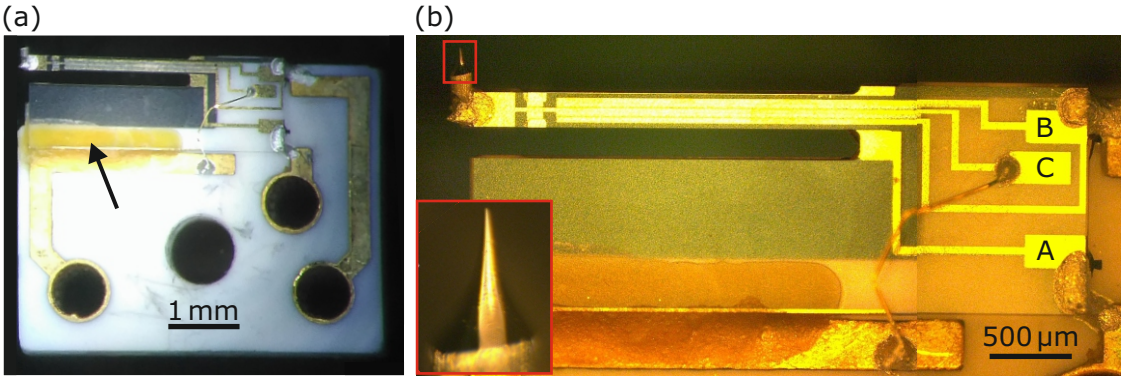

Figure 3.3. (a) The custom-built qPlus sensor consists of a ceramic base plate (white) and an asymmetric Statek tuning fork (transparent) which is made of quartz [5, 69]. The larger base of the tuning fork is fixed to the alumina base plate using a non-conductive glue (orange colored, indicated by black arrow). (b) The tuning fork features three gold plated contact pads for deflection detection (A and B) and for the electrical connection of the tip (C). If the free prong of the tuning fork is bent statically, the piezoelectric effect leads to a potential difference between contact pad A and B. The inset of this panel shows a zoomed image of the electrochemically etched tungsten tip which is glued using electrically conductive glue to the end of the free prong of the sensor. The diameter of the tip wire is 125 μm.

[1]EPO-TEK H70E from Epoxy Technology Inc., Billerica 01821-3972 MA, USA
[2]Polytec EC101 from Polytec PT GmbH, Waldbronn, Germany

deflection of the qPlus sensor is assembled at gold pads A and B. Here, gold pad B is electrically connected to gold electrodes on the top and back side of the free prong, while gold pad A is connected to gold electrodes at the side faces of the free prong oriented perpendicular to the top and back gold electrodes. If the free prong of the qPlus sensor oscillates at an amplitude of A and frequency of f, the piezoelectric effect results in a time-dependent generation of charges $Q(t)$ described by $Q(t) = Q_0 \exp(i(2\pi f t + \phi))$ at the gold pads A and B with phase Φ shifted by 180° with respect to each other. The induced current at gold pads A ($\phi = 0$) and B ($\phi = \pi$) can be written as $I(t) = \partial Q(t)/\partial t = i2\pi f Q_0 \exp(i(2\pi f t + \phi))$. The current $I(t)$ is direct proportional to the deflection A of the qPlus sensor. Using a differential current-to-voltage amplifier [91], the amplitude A and frequency f of the oscillation is measured. Here, the differential measurement enhances the signal to noise ratio (SNR) by a factor of $\sqrt{2}$ with respect to a single ended measurement [67, 69, 102, 103].

To perform FM-AFM, the free prong of the qPlus sensor needs to oscillate at a constant amplitude A along the z axis (see subsection 2.2.3). To obtain a constant amplitude A, the qPlus sensor is driven mechanically at its resonance frequency f in the used setup while the amplitude A is measured in real time[1]. The qPlus sensor intrinsically loses energy per oscillation cycle of $\Delta E_{\text{cycle}} = 2\pi \frac{E}{Q}$ [66] which depends on the quality factor Q and the stored energy in the tuning fork $E = \frac{1}{2}kA^2$. Here k is the stiffness of the qPlus sensor. Additionally, dissipative forces (i.e. non-conservative forces) between tip and sample can cause further energy loss. In FM-AFM, a feedback loop ensures that the dissipated energy loss is compensated by mechanically driving the sensor at its resonance frequency f, while the phase relation between drive signal and sensor oscillation is kept constant using a phase-locked loop (PLL).

The eigenfrequency of the used qPlus sensor dropped from about 33 000.0 Hz to $f_0 = 20\,430.4$ Hz after attaching the tip of mass Δm as the effective mass of the harmonic oscillator m^* increases to $m^* + \Delta m$. The eigenfrequency is then given by:

$$f_0 = 2\pi \sqrt{\frac{k}{m^* + \Delta m}} \tag{3.1}$$

[1] Nanonis, SPECS Zurich GmbH, Zurich, Switzerland

Using this equation, the eigenfrequency f_0 of the sensor can be tuned by selecting a tip with a certain mass. This is explicitly considered when building the qPlus sensor shown in Fig. 3.3 using an electrochemically etched tungsten tip ($\rho_W = 19.25\,\mathrm{g/cm^3}$) as the microscope head (i.e. probably the motor for the coarse approach[1]) shows resonances in a frequency regime between about 26 kHz to 31 kHz. Hence, a thicker W wire (diameter of 125 μm) is used instead of the standard 50 μm thick wire and is electrochemically etched to a total tip length of 300 μm to achieve a resonance frequency of the qPlus sensor well below the resonances of the coarse motor.

Another advantage of the qPlus sensor is its robustness with respect to jump-to-contact. Jump-to-contact describes a sudden contact between tip and sample which can occur if the stiffness of the cantilever k is smaller than the maximum force gradient k_{ts} between tip and sample [79]. As the stiffness of the used qPlus sensor ($k = 1800\,\mathrm{N/m}$) is much larger than typical force gradients between tip and sample which are in the order of tens to hundreds of N/m jump-to-contact is avoided [66]. However, jump-to-contact can also be prevented when using soft Si-cantilevers[2] by selecting a large amplitude A such that the restoring force of the cantilever $F_{\mathrm{restore}} = kA$ is greater than the attractive force between tip and sample $F_{ts} = -\int k_{\mathrm{ts}}\mathrm{d}z$ [56].

3.4. Tip Preparation and Functionalization

Characterized and functionalized tips enhance the resolution in STM and FM-AFM and allow reproducing the experiments in a controlled manner. In this section, the tip characterization, preparation and functionalization is briefly described.

The qPlus sensor used in this work is equipped with a tungsten wire which is electrochemically etched [104] to create a sharp tip at its end (see Fig. 3.3(b) in section 3.3). After tip attachement, the qPlus sensor is mounted into the microscope head and UHV and LT conditions are achieved (see section 3.1). Afterwards, field

[1] The resonances of the scan piezo tube are checked by measuring the double piezo electric response as proposed in Ref. [45]. A broad resonance between 26 kHz to 29 kHz is detected. However, a qPlus sensor with $f_0 \approx 30\,\mathrm{kHz}$ showed severe side resonances which compromise FM-AFM measurements. Therefore, the scan piezo tube is not responsible for the appearance of the side resonances and, hence, the coarse motor which consists of shear piezo stacks presumably exhibits additional resonances in the regime between 29 kHz to 31 kHz.

[2] Si-cantilever typically possess stiffnesses in the order of tens of N/m.

emission above the Cu(111) sample is performed to remove the oxide layers of the tip's apex which were created during the etching process: In field emission, a constant field emission current of about 10 μA to 100 μA at a bias voltage of 200 V is kept constant by using a z feedback loop. This leads to local heating of the tip apex which results in the removal of oxide layers and impurities. During field emission, the tip-sample distance increases since the tip is getting sharper microscopically until some parts of the tip apex are removed. The tip approaches the sample to keep the field emission current constant if parts from the tip are removed. Consequently, the tip should be retracted while the tip-sample distance is increasing to obtain a microscopically sharp tip [105].

The microscopical sharpness of a metal tip can be evaluated by studying the frequency shift Δf value at a certain conductance reference point [106]. In the following, a conductance reference of $\langle G \rangle = 100\,\mathrm{pA}/10\,\mathrm{mV} = 10\,\mathrm{nS}$ on the bare Cu(111) is used to discuss the tip's sharpness as, at the corresponding z position, the metal tip is mainly interacting via the attractive van-der-Waals interaction with the surface. Attractive tip-sample interactions lead to a decrease of the resonance frequency f in FM-AFM. Hence, the closer the frequency shift value Δf at the conductance reference point of $\langle G \rangle = 10\,\mathrm{nS}$ approaches zero, the sharper the metal tip is. The frequency shift value depends on the stiffness k, the eigenfrequency f_0, and the oscillation amplitude A of the used AFM sensor. Therefore, the remainder considers the averaged force gradient $\langle k_{\mathrm{ts}} \rangle = 2k\Delta f/f_0$ value to enable comparability between different types of AFM sensors [56]. A metal tip is defined as microscopically sharp if the averaged force gradient value $\langle k_{\mathrm{ts}} \rangle$ falls within a range of $-0.24\,\mathrm{N/m}$ to $-0.12\,\mathrm{N/m}$ when using an oscillation amplitude of $A = 50\,\mathrm{pm}$. Typically, less negative force gradient values than $-0.12\,\mathrm{N/m}$ are scarcely achieved. If $\langle k_{\mathrm{ts}} \rangle$ at the reference conductance point is smaller than $-0.24\,\mathrm{N/m}$, the tip should be repeatedly poked in a controlled fashion into the clean Cu(111) sample by several hundreds of picometers to few nanometers until $\langle k_{\mathrm{ts}} \rangle$ lies in the range of $-0.24\,\mathrm{N/m}$ to $-0.12\,\mathrm{N/m}$. However, a microscopically sharp tip can feature a force gradient value $\langle k_{\mathrm{ts}} \rangle$ significantly lower than $-0.24\,\mathrm{N/m}$ by exhibiting a secondary tip which is laterally displaced. The secondary tip might not be detected necessarily in the STM or AFM images as it might be quite blunt. Therefore, when obeying the above described range for the averaged force gradient, from time to time a microscopically sharp tip is poked into the Cu surface as it exhibits a secondary laterally displaced

tip.

In order to discriminate imaging artifacts due to an asymmetric tip (by e.g. multiple atoms at the tip's apex), it is suitable to terminate the tip's apex with a radially symmetric feature such as a single atom or molecule. This is further beneficial as the tunneling current decays by an order of magnitude when increasing the tip-sample distance z by 100 pm (see section 2.1) and the short-range forces also possess decay lengths of tens to few hundreds of picometers (see subsection 2.2.2). This means that the main interaction will occur between the single atom or molecule of the tip and the adsorbate or sample. To obtain a monoatomic metal tip, the microscopically sharp tip is again poked repeatedly hundreds of picometers to few nanometers into the clean Cu(111) sample. After each poke the tip is imaged by performing the carbon monoxide front atom identification (COFI) technique to determine the atomic structure of the tip's apex [33, 92]. In COFI, a single CO molecule adsorbed on the Cu(111) surface acts effectively as a probe. When scanning the CO molecule consecutively in constant-height mode while reducing the tip-sample distance z in-between each image, shortly before the CO molecule is manipulated laterally on the surface [107], the frequency shift image $\Delta f\,(x, y)$ resolves the atomic structure of the tip's apex. In case the COFI image resembles a radially symmetric attractive feature, the tip is terminated by a single metal atom (presumably Cu) [33, 92, 93].

The resolution capability in STM [31] and AFM [32] can be further enhanced by terminating the monoatomic metal tip with a single CO molecule. Using CO tips allowed resolving various sample systems such as organic molecules [32, 34–36], two-dimensional materials [37, 38], ionic surfaces [39], interfacial water [41] and small metal clusters [33] with unprecedented atomic resolution. In many cases, Pauli repulsion between the CO tip and the charge density of the investigated chemically inert samples (especially organic molecules) is the origin of the high-resolution [61]. In case of single Fe and Cu atoms, the origin of the appearance of non-trivial features (i.e. a torus-shaped appearance of single atoms) is the result of a hybridization of the tip's CO with the investigated single atom on the substrate. Hence, CO tips can transition from physisorption to chemisorption, i.e. form a chemical bond, when approaching the center of a single Fe or Cu adatom on Cu(111) [42]. Latter findings are briefly discussed in the first part of chapter 5 in case of the single Fe adatom. Moreover, the termination with a single CO molecule can lead to imaging artifacts

if large lateral forces act on the tip's CO molecule due to its lateral flexibility. The lateral stiffness of a CO molecule adsorbed on a monoatomic metal tip is $k_x = 0.24\,\mathrm{N/m}$ [60]. Hence, the tip's CO laterally deflects by 104 pm if a lateral force of 25 pN acts on it. The probe particle model (PPM) which considers van-der-Waals, electrostatic and repulsive (due to Pauli repulsion) interactions reproduces many experimental results on chemically inert sample systems – including imaging artifacts due to CO tip bending by using a flexible probe [63, 108].

Next, an improved CO pickup process from the sample to a monoatomic tip is introduced briefly as it differs from the original method established by Bartels *et al.* in Refs. [31, 95]. A modified method which was used in this work is described in Ref. [78]. The latter method is further adapted resulting in a significant enhancement of the pickup probability of a single CO molecule from the Cu(111) surface to a monoatomic metal tip. As described in Ref. [78], to functionalize a monoatomic metal tip with a CO molecule, a COFI image needs to be acquired to determine the most attractive lateral position at first (i.e. the position of the most negative frequency shift value $\Delta f\,(x, y, z = \text{const.})$). Afterwards, the monoatomic metal tip is positioned at the most attractive (x, y) position, while the z feedback loop is switched on using a tunneling current setpoint of $\langle I_{\mathrm{set}} \rangle = 2\,\mathrm{nA}$ and a bias voltage of $V_{\mathrm{tip}} = -10\,\mathrm{mV}$[1]. Subsequently, the bias voltage V_{tip} is lowered to $-2.4\,\mathrm{V}$. Reference [78] proposes to switch off the feedback loop and manually reduce the tip-sample distance until a drop or rise in the tunneling current channel $\langle I \rangle$ is detected. A rise is attributed to the removal of the CO molecule from the tip-sample junction, while a drop is interpreted as successful transfer of the CO to the tip. However, during this thesis it was found that the CO molecule is often transferred to the tip before switching off the feedback loop. Therefore, it is assumed that if in this case, the feedback loop is switched off and the tip is manually approached to the surface the CO desorbs from the monoatomic metal tip's apex and the tunneling current shows the characteristic rise. This circumstance can be avoided by checking the relative tip-sample distance z_{rel} when lowering the bias voltage to $-2.4\,\mathrm{V}$ while the feedback loop is still switched on (see Fig. 3.4). In the pickup experiment shown in Fig. 3.4, the bias voltage was lowered from $-10\,\mathrm{mV}$ to $-2.4\,\mathrm{V}$ within 9.7 s, while the monoatomic metal tip is positioned above the most attractive position of the COFI

[1] The oscillation amplitude is set to $A = 50\,\mathrm{pm}$.

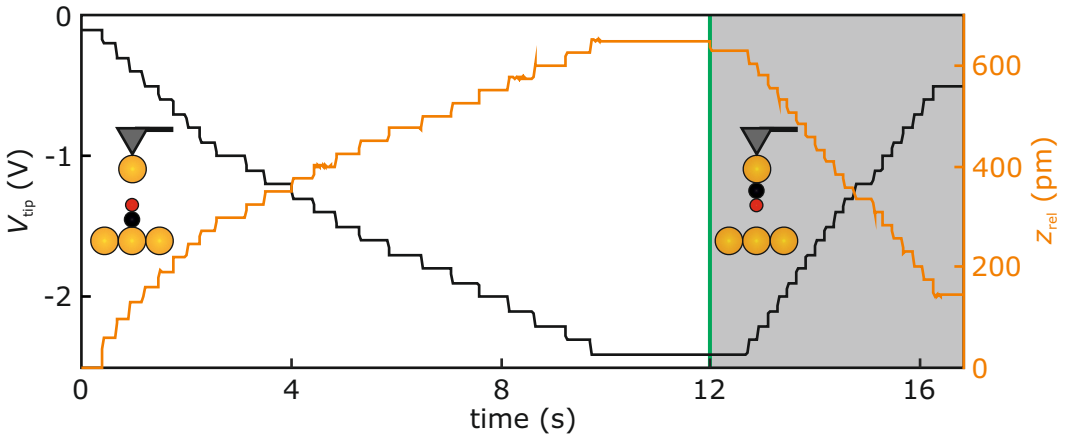

Figure 3.4. Time trace of the manually changed bias voltage which is applied to the tip V_{tip} and of the relative tip height z_{rel} during the transfer of a single CO molecule from the surface to the apex of a monoatomic metal tip. The feedback loop controlling the vertical position of the tip is switched on during the complete experiment ($\langle I_{\text{set}} \rangle = 2\,\text{nA}$). The bias voltage V_{tip} is subsequently lowered to $V_{\text{tip}} = -2.4\,\text{V}$ at $t = 9.7\,\text{s}$. 2.3 s later, while the bias voltage V_{tip} remains unchanged, the feedback loop suddenly reduces the vertical tip position z by 19 pm in order to keep the tunneling current $\langle I \rangle$ at $\langle I_{\text{set}} \rangle$. At that moment ($t = 12\,\text{s}$, vertical green line) the CO molecule is vertically transferred from the surface to the tip apex (see sketches in the insets) and, 0.7 s later, the bias voltage is reduced subsequently to $-0.5\,\text{V}$. The cantilever and its tip are not sketched to scale.

image ($\Delta f\,(x, y, z = \text{const.})$). Afterwards, the feedback loop remains closed and the relative tip-sample position z_{rel} is recorded. At $t = 12\,\text{s}$, a drop of 19 pm in the z_{rel} position can be observed (see vertical green line in Fig. 3.4) and, thereupon, the bias voltage V_{tip} is rapidly increased closer to zero. By performing a COFI image afterwards, a CO functionalization of the monoatomic metal tip (as sketched in the inset of Fig. 3.4) could be verified. Consequently, the CO is transferred to the tip at $t = 12\,\text{s}$. It is observed during the experiments of this thesis that the described characteristic drop in the z_{rel} position occurs in a bias range of $-2\,\text{V}$ to $-2.6\,\text{V}$[1] and the manual approach of the tip to the sample with a switched-off feedback loop is only needed if no drop in z is detected. Observing the z_{rel} position of the tip and recognizing small drops increases the CO molecule pickup probability[2] drastically to 80%. Before using this adapted CO pickup method, certain monoatomic metal

[1] In most of the cases it occurs in a bias range of $-2\,\text{V}$ to $-2.4,\text{V}$.
[2] The CO molecule pickup probability is defined by the number of successful CO pick up experiments divided by the total number of pickup attempts.

tips could not be functionalized with a CO molecule. Thus it can be suggested that in these cases the CO molecule was unperceived transferred to the tip for a short time but quickly desorbed from the tip's apex upon the manual approach of the tip towards the sample. However, prior to the above described finding, it was observed that a tip which was used for 1.5 years to investigate Fe clusters and adatoms on the Cu(111) sample could not be functionalized with a CO molecule anymore. The tip was probably covered with Fe as numerous Fe evaporation cycles took place during the 1.5 years. Within this work, no such indication is observed which is attributed to a design change of the microscope head resulting in an improved shadowing of the tip during Fe evaporation. This observation indicates that the adsorption of CO molecules on monoatomic Fe covered tips is not possible at all.

4. Lateral Manipulation of Single Fe Adatoms Using Characterized Tips

Most of the work presented in this chapter is published in Physical Review B [82]. Parts of the following text are identical to the publication. The author performed most[1] of the experimental measurements and carried out the complete analysis. Additionally, initial results of the lateral manipulation experiments[2] are presented in the master thesis of the author [109] and are analyzed in detail in sections 4.3 and 4.4 of this thesis.

This chapter describes, first, different modes in lateral manipulation (section 4.1) and, second, the basic principle of lateral manipulation experiments including the extraction of lateral forces (section 4.2). Afterwards, lateral manipulation experiments of single Fe adatoms on Cu(111) using monoatomic metal and CO-terminated monoatomic metal tips are presented and compared with respect to each other (section 4.3). Furthermore, an analytic model describing the experimental findings is introduced (see section 4.5). Finally, the assembly of small Fe clusters with atomic precision using CO tips is discussed (section 4.6).

[1] The first atom-by-atom assembly experiments of small Fe clusters, depicted in Fig. 4.12, were conducted together with Fabian Stilp during the measurements for his bachelor thesis within the group of Giessibl.

[2] i.e. the investigation of the lateral force threshold for lateral manipulation of single Fe adatoms and the tip tilt analysis of monoatomic metal and CO-terminated monoatomic metal tips

4.1. Various Modes in Lateral Manipulation

Individual atoms can be laterally manipulated in three different modes: pushing, pulling and sliding mode. These three modes were initially characterized by STM [8]. In the pushing mode, a repulsive interaction between tip and adatom initiates the lateral manipulation process. As the tip approaches the center of the adatom, it is pushed away from the tip, similar to a snow plow. Pulling describes the attractive lateral manipulation mode. In pulling mode, the adatom follows the tip's movement in discrete steps when the tip moves away from it. After the adatom is laterally manipulated, in the pushing and pulling mode, it remains temporally on an adsorption site until it is pushed or pulled another time. Hence, both modes are operating in a discontinuous manner. The sliding mode describes the continuous, collective movement of the adatom and tip without any interruption [8].

Next, two examples of the attractive pulling mode are presented. A single Fe adatom is manipulated laterally using a monoatomic metal and a CO-terminated monoatomic metal tip, respectively. Figure 4.1(a) shows the conductance trace $G(x)/G_0$ recorded while a monoatomic metal tip is scanned in constant-height across the center of a single Fe adatom adsorbed on Cu(111). Here, the conductance $G(x)$ is normalized with respect to the conductance at point contact of monoatomic metal tips $G_0 = (12906\,\Omega)^{-1}$ [13]. The tip's linear path is selected to cross equivalent fcc hollow sites (see sketch in Fig. 4.1(c)). At a tip-sample distance z greater than the manipulations threshold height, the conductance curve resembles a Gaussian shape centered around $x = 0$. Hence, the Fe adatom's initial position can be identified ($x = 0$). Upon approaching the tip laterally to the Fe adatom's center, the normalized conductance $G(x)/G_0$ rises slowly until a sudden increase at $x = -288\,\text{pm}$ occurs. Afterwards, the normalized conductance $G(x)/G_0$ increases for the next 33 pm and, thereafter, decreases with further increasing x. This means that the tip moves away from the Fe adatom's center. The adsorption position can be determined by fitting a Gaussian curve to each section of the normalized conductance trace $G(x)/G_0$. Single Fe adatoms adsorb in fcc positions on Cu(111) [97, 98] and the maxima of each section of the normalized conductance curve remain similar in absolute value. Hence, it can be concluded that the Fe adatom is manipulated to the nearest fcc hollow site along the $-x$ direction[1] as the tip is approaching its center. The change

[1] The nearest-neighbor distance on the Cu(111) surface is 255 pm [94].

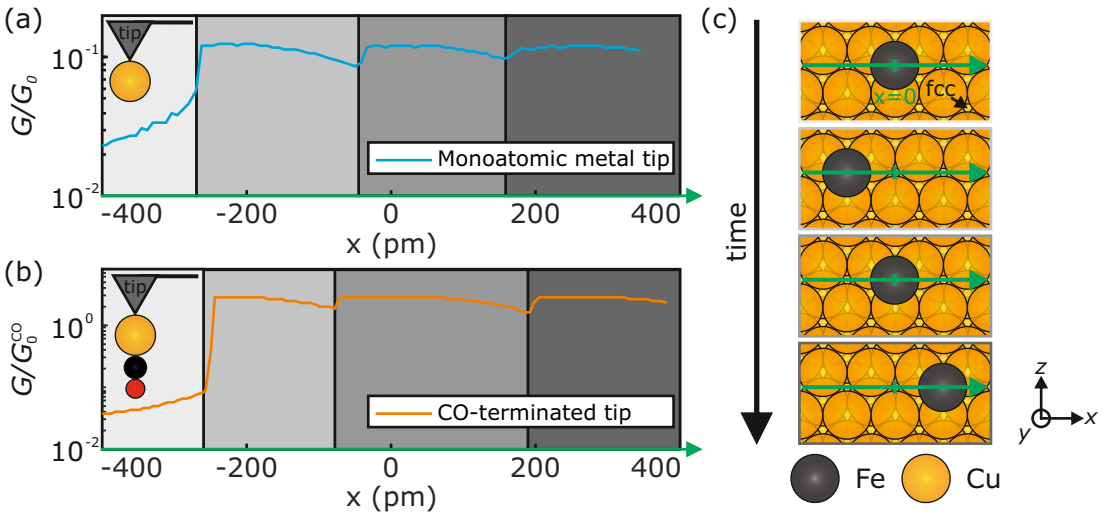

Figure 4.1. Conductance traces $G(x)$ normalized with respect to G_0 and G_0^{CO} while scanning across the center of a single Fe adatom on Cu(111) using (a) a monoatomic metal tip and (b) a CO-terminated monoatomic metal tip, respectively (see sketches in insets). (c) Top view of the Fe adatom adsorbed on the Cu(111) surface in different states of the lateral manipulation experiment. The color of each frame corresponds to the colored sections of the normalized conductance traces shown in panels (a) and (b). The cantilever and its tip are not sketched to scale in panels (a)-(b). The two conductance traces are also shown in Ref. [82].

in adsorption position with respect to the substrate is sketched in the upper two panels of Fig. 4.1(c). The colored frames of the individual panels of Fig. 4.1(c) correspond to the colored x sections in Fig. 4.1(a). The Fe adatom is now located at $x = -255\,\mathrm{pm}$. As the tip is moving away from the new adsorption position of the Fe adatom along the $+x$ direction, another sharp change in the normalized conductance occurs at $x = -50\,\mathrm{pm}$ and, thereafter, the normalized conductance $G(x)/G_0$ increases with increasing x position. Hence, the Fe adatom is manipulated laterally by one lattice site back to its initial adsorption position (as indicated at the third panel from the top in Fig. 4.1(c)). Afterwards, another attractive pulling process occurs at a tip position of $x = 156\,\mathrm{pm}$ and, therefore, the Fe adatom is manipulated laterally to the adsorption site at $x = 255\,\mathrm{pm}$. The lateral movement of the tip is stopped at $x = 345\,\mathrm{pm}$.

Using a CO-terminated monoatomic metal tip qualitatively results in a similar

normalized $G(x)/G_0^{\mathrm{CO}}$ curve[1] (see Fig. 4.1(b)) while the absolute values of the conductance differ due to the different tunneling rates of the tips. Moreover, the exact x positions of the individual lateral manipulation events are slightly different for both tips. In case of the CO tip, the Fe adatom is also manipulated at first by one position along the $-x$ direction as the tip approaches the center of the adatom. Afterwards, the adatom follows the tip's movement twice as the tip is moving away from the adatom (see Fig. 4.1(c) for the corresponding intermediate adsorption positions of the Fe adatom during the lateral manipulation experiment). In both cases, the Fe adatom initially jumps towards and below the tip along the $-x$ direction and, afterwards, is pulled two times along the $+x$ direction as the tip moves away from the Fe adatom. Note that the initial lateral manipulation in the $-x$ direction is attractive and, therefore, also called pulling of the Fe adatom. In conclusion, both presented tips manipulate the single Fe adatom in the attractive pulling mode.

Experimental examples of the pushing and sliding mode are not presented within this section as they are not relevant for this work. They can be found in Ref. [8].

4.2. Basic Principle of Lateral Manipulation Experiments and Determination of Lateral Forces

Within this section, the principle procedure to determine lateral force thresholds in a lateral manipulation experiment in combined STM/AFM is described briefly[2]. A single Fe adatom which adsorbs on a fcc hollow site on the Cu(111) surface is surrounded by six equivalent nearest fcc hollow sites (see Fig. 4.2(a)). All lateral manipulation experiments presented in section 4.3 are conducted along the high-symmetry directions $\vec{x}_{\mathrm{A}}$, $\vec{x}_{\mathrm{B}}$ and $\vec{x}_{\mathrm{C}}$. Here, the manipulation path is chosen such that it linearly connects the center of the adsorbed Fe adatom ($x = 0$) with the neighboring fcc hollow sites at $x = \pm 255\,\mathrm{pm}$. Afterwards, a two-dimensional

[1] Note that the normalization is performed with respect to the conductance at point contact for CO tips $G_0^{\mathrm{CO}} = (404497\,\Omega)^{-1}$ [81].

[2] The procedure follows the approach introduced by Ternes *et al.* [13] and realized by Emmrich *et al.* [107] within the group of Giessibl.

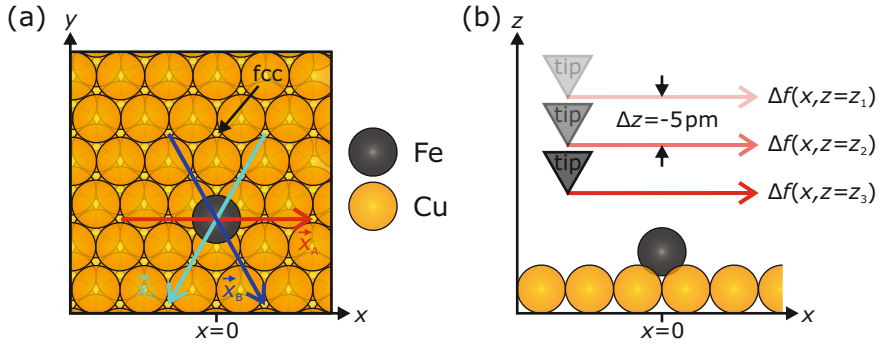

Figure 4.2. (a) Top view of a Fe adatom adsorbed on the Cu(111) surface. The three possible manipulation orientations (6 directions) which link equivalent fcc hollow sites are indicated as $\vec{x}_{\mathrm{A}}$, $\vec{x}_{\mathrm{B}}$ and $\vec{x}_{\mathrm{C}}$. (b) In order to analyze lateral force thresholds, a two-dimensional $\Delta f\,(x,z)$ data set needs to be acquired. For that, the tip scans directly across equivalent fcc hollow sites along a line which matches one of the three high-symmetry directions of the Cu(111) substrate. After each linescan, the tip-sample distance z is reduced by decrements of $\Delta z = -5\,\mathrm{pm}$. The tip's movement is stopped manually once the Fe adatom is manipulated laterally.

$\Delta f\,(x,z)$ and $\langle G\,(x,z)\rangle$ data set is simultaneously recorded. For that, the initial tip-sample distance $z = z_{\mathrm{start}}$ is set large enough such that the frequency shift $\Delta f\,(x, z_{\mathrm{start}})$ curve is flat. Using the LabVIEW [1] routine of Ref. [107], consecutive linescans are recorded while the z coordinate is reduced by 5 pm after each linescan has finished (see Fig. 4.2(b)). During backtracing the tip to the lateral starting position, the z coordinate is lifted by 50 pm to make sure the lateral manipulation process occurs in the forward scanning direction. When the Fe adatom is manipulated laterally at a tip-sample distance $z = z_{\mathrm{man}}$, the actual linescan is finished and the tip moves back to the lateral starting position at $z = z_{\mathrm{man}} + 50\,\mathrm{pm}$. The adsorption position after the lateral manipulation is deduced by investigating the corresponding conductance curve $\langle G\,(x, z_{\mathrm{man}} + 50\,\mathrm{pm})\rangle$ acquired during the final backtrace.

Afterwards, the recorded two-dimensional $\Delta f\,(x,z)$ data set is post-processed as described in subsection 2.3.4 (in the case of three-dimensional data sets). In that way, the two-dimensional short-range vertical force $F_{z,\mathrm{SR}}\,(x,z)$, the short-range potential $U_{\mathrm{SR}}\,(x,z)$ and the lateral force $F_x\,(x,z)$ between the Fe adatom and the tip are deconvoluted [74, 77] (following the procedure introduced in Ref. [13]).

As the data sets are recorded in constant-height mode, it is important to consider thermal drift between tip and sample as well as piezo creep. The piezo creep

[1] LabVIEW, National Instruments Corporation, Austin, TX 78759, USA

and remaining thermal drift which are still present, although all experiments are conducted in UHV conditions at $T_{\mathrm{mic}} \approx 5.7\,\mathrm{K}$ (see section 3.1), are compensated. This leads to an overall remaining lateral and vertical drift speed of less than 10 fm/s. The acquisition time of one two-dimensional $\Delta f\,(x,z)$ and $\langle G\,(x,z)\rangle$ data set is about 30 min. This can be converted to a remaining lateral and vertical drift of 18 pm which is significantly smaller than the nearest-neighbor distance on Cu(111) of 255 pm.

4.3. Directional Dependence of the Force Threshold in Lateral Manipulation of Single Fe Adatoms Using Monoatomic Metal and CO-Terminated Monoatomic Metal Tips

Figure 4.3(a) shows selected $\Delta f\,(x_{\mathrm{A}}, z_{i,\mathrm{Me}})$ curves at four different tip-sample distances $z_{i,\mathrm{Me}}$ ($i = 1,2,3,4$) recorded with a monoatomic metal tip in constant-height along the $\vec{x}_{\mathrm{A}}$ direction (see Fig. 4.2(b)).

The Fe adatom is initially located at $x_{\mathrm{A}} = 0$. At $z_{1,\mathrm{Me}} = 571\,\mathrm{pm}$, the frequency shift curve $\Delta f\,(x_{\mathrm{A}})$ is flat. Upon approaching the tip towards the sample, a shallow minimum centered at $x_{\mathrm{A}} = 0$ evolves (see $\Delta f\,(x, z_{2,\mathrm{Me}})$ and $\Delta f\,(x, z_{3,\mathrm{Me}})$ traces). At the tip-sample distance $z_{4,\mathrm{Me}} = 186\,\mathrm{pm}$, a sharp change in the $\Delta f\,(x_{\mathrm{A}})$ curve occurs at $x_{\mathrm{A}} = x_{\mathrm{man}}$ (see vertical light blue dotted line). Investigating the normalized conductance curve $G\,(x_{\mathrm{A}}, z_{4,\mathrm{Me}} + 50\,\mathrm{pm})\,/G_0$ of the last backward scan (see Fig. 4.3(b)) reveals that its maximum is laterally shifted by $+255\,\mathrm{pm}$ along the $+\vec{x}_{\mathrm{A}}$ direction with respect to the conductance curves recorded at larger tip-sample distances[1]. Hence, the Fe adatom changed its lateral adsorption position from $x_{\mathrm{A}} = 0$ to the nearest equivalent fcc hollow site at $x_{\mathrm{A}} = 255\,\mathrm{pm}$ along the $+\vec{x}_{\mathrm{A}}$ direction (as indicated in Fig. 4.3(c)).

Afterwards, the monoatomic metal tip is functionalized with a single CO molecule (CO tip A) and the experiment is repeated. At a tip-sample distance $z_{1,\mathrm{CO}} = 560\,\mathrm{pm}$, the $\Delta f\,(x, z_{1,\mathrm{CO}})$ curve no longer varies with x (see Fig. 4.3(d)). Approaching the CO tip by 120 pm results in the appearance of an attractive depression centered

[1] Therefore they exhibit smaller maxima ($G\,(x_{\mathrm{A}} = 0)\,/G_0$) at the center of the Fe adatom ($x_{\mathrm{A}} = 0$).

at $x_A = 0$. A further reduction of z to $z_{3,CO} = 220\,\text{pm}$ leads to the formation of two bumps at $x_A \approx \pm 220\,\text{pm}$. These bumps lead to the appearance of a single Fe adatom as a torus in the (x, y) plane (see Fig. 4.7(b)) [33] whose physical origin is described in Ref. [42] and is discussed briefly in chapter 5. At the tip-sample distance $z_{4,CO} = 205\,\text{pm}$, a sharp change in the $\Delta f\,(x, z_{4,CO})$ curve occurs at $x_A = x'_{man} < 0$ before the CO tip passes the center of the Fe adatom at $x_A = 0$. All normalized conductance traces $G\,(x_A, z)\,/G_0^{CO}$, except the one acquired at $z = z_{4,CO} + 50\,\text{pm}$, are centered at $x_A = 0$ (see Fig. 4.3(e)). The conductance curve acquired in the backward scan after the sharp change in the $\Delta f\,(x, z_{4,CO})$ curve occurred is centered at $x_A = -255\,\text{pm}$. Therefore, the Fe adatom is laterally manipulated from $x_A = 0$ to the nearest fcc hollow site located at $x_A = -255\,\text{pm}$ along the $-\vec{x}_A$ direction (as indicated in Fig. 4.3(f)).

In summary, the Fe adatom was manipulated by 255 pm to a neighboring fcc hollow site with both tips. However, the manipulation direction is reversed with respect to each other: In case of the monoatomic metal tip, the Fe adatom was manipulated along the $+\vec{x}_A$ direction while, after the CO termination of the tip, the Fe adatom was manipulated along the $-\vec{x}_A$ direction.

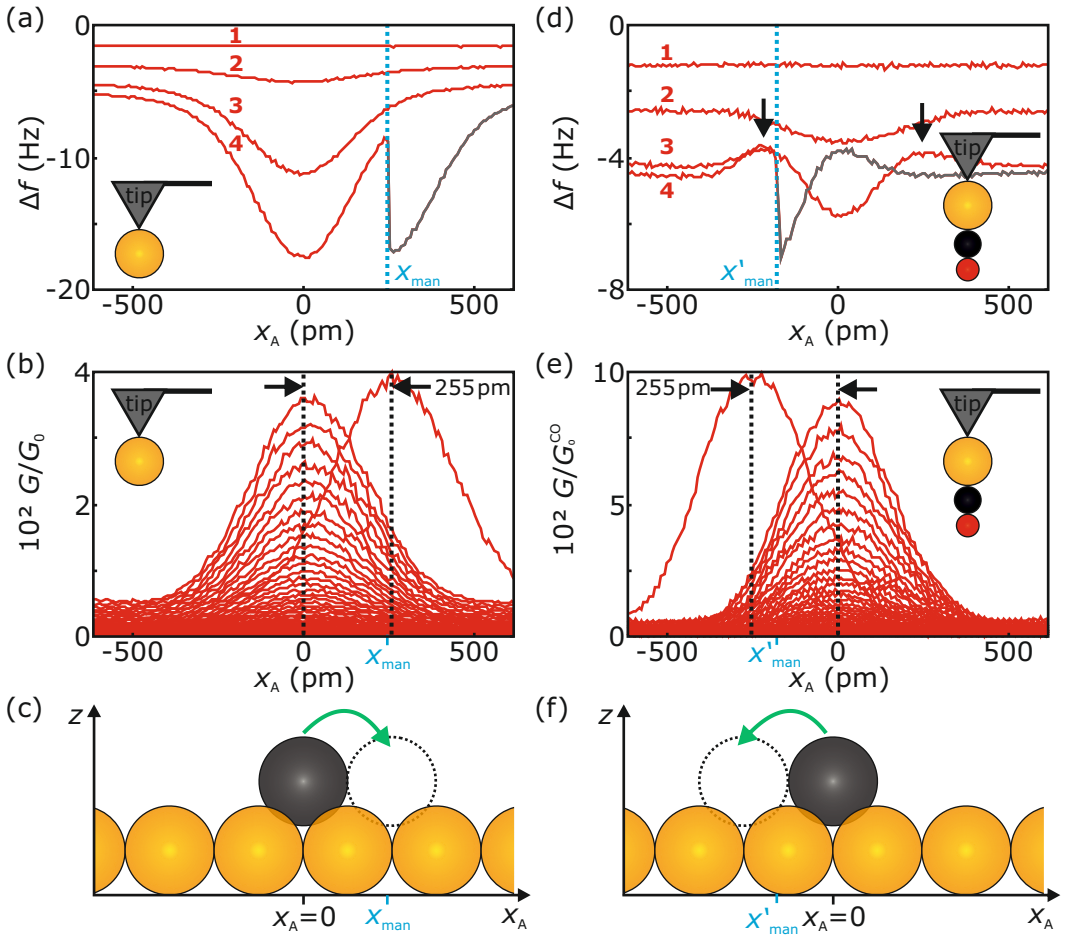

Figure 4.3. (a) Selected $\Delta f\,(x_\mathrm{A}, z_{i,\mathrm{Me}})$ curves $(i = 1, 2, 3, 4)$ acquired during scanning a monoatomic tip across the center of a single Fe adatom adsorbed on the Cu(111) surface at $x_\mathrm{A} = 0$ along the $\vec{x}_\mathrm{A}$ direction (see Fig. 4.2). The tip-sample distances $z_{i,\mathrm{Me}}$ indicate the distance to the conductance at point contact $G_0 = (12906\,\Omega)^{-1}$ [13] above the bare Cu(111) surface (see subsection 2.3.1): $z_{1,\mathrm{Me}} = 571\,\mathrm{pm}$, $z_{2,\mathrm{Me}} = 291\,\mathrm{pm}$, $z_{3,\mathrm{Me}} = 211\,\mathrm{pm}$ and $z_{4,\mathrm{Me}} = 186\,\mathrm{pm}$. The $\Delta f\,(x, z_4)$ curve shows a sharp change at $x_\mathrm{A} = x_\mathrm{man} > 0$ after the tip passes the Fe adatom's center. (b) The conductance curves $G\,(x_\mathrm{A}, z + 50\,\mathrm{pm})\,/G_0$ acquired during backtracing at $z + 50\,\mathrm{pm}$ reveal that the adatom is manipulated by one lattice site along the $+\vec{x}_\mathrm{A}$ direction to $x_\mathrm{A} = 255\,\mathrm{pm}$ (as indicated in the sketch shown in panel (c)). Panels (d) to (f) show the same results as presented in panels (a) to (c) after the monoatomic metal tip is terminated with a single CO molecule (CO tip A). Using CO tip A, the lateral manipulation occurs at $x'_\mathrm{man} < 0$ before passing the adatom's center and the adatom is manipulated to the nearest equivalent fcc hollow site along the $-\vec{x}_\mathrm{A}$ direction. Using the CO tip, the tip-sample distances are calculated with respect to the conductance at point contact of CO tips of $G_0^\mathrm{CO} = (404497\,\Omega)^{-1}$ [81]: $z_{1,\mathrm{CO}} = 560\,\mathrm{pm}$, $z_{2,\mathrm{CO}} = 340\,\mathrm{pm}$, $z_{3,\mathrm{CO}} = 220\,\mathrm{pm}$ and $z_{4,\mathrm{CO}} = 205\,\mathrm{pm}$. The corresponding full frequency shift $\Delta f\,(x_\mathrm{A}, z)$ datasets to panels (a) and (d) are shown in Fig. A.1 of the appendix. The cantilever and its tip are not sketched to scale in panels (a), (b), (d) and (e). The experimental data shown in this figure are also presented in Ref. [82].

To gain further insight into the manipulation process, the short-range potential $U_{\mathrm{SR}}(x_{\mathrm{A}}, z)$ and the lateral force $F_{\mathrm{x}}(x_{\mathrm{A}}, z)$ are deconvoluted (as described in subsection 2.2.3) and presented in Fig. 4.4. The short-range potential $U_{\mathrm{SR}}(x_{\mathrm{A}}, z)$ between the monoatomic metal tip and the single Fe adatom is entirely negative and, hence, attractive. Figure 4.4(b) depicts selected lateral force traces $F_x(x_{\mathrm{A}})$. Here, darker colored curves correspond to smaller tip-sample distances. The smaller the tip-sample distance gets, the higher the absolute values of the lateral force curves become. Throughout this work, a positive (negative) lateral force value indicates a lateral force acting on the Fe adatom pointing along the negative (positive) $\vec{x}$ direction. As for tip positions $x_{\mathrm{A}} < 0$ ($x_{\mathrm{A}} > 0$), the lateral force curves are entirely positive (negative) the Fe adatom is always attracted by the tip. Hence, while the tip is laterally approaching the Fe adatom at $x_{\mathrm{A}} = 0$ from the left side, the Fe adatom is attracted to the left side (towards the tip). After the tip passes the Fe adatom's center, Fe atom is attracted to the right side (towards the tip). The lateral manipulation event of the single adatom occurs at $x_{\mathrm{A}} = x_{\mathrm{man}}$ (see Fig. 4.3). The lateral force $F_x(x_{\mathrm{man}}, z_{4,\mathrm{Me}})$ value at $x_{\mathrm{A}} = x_{\mathrm{man}}$ is given by $-29\,\mathrm{pN}$. This lateral

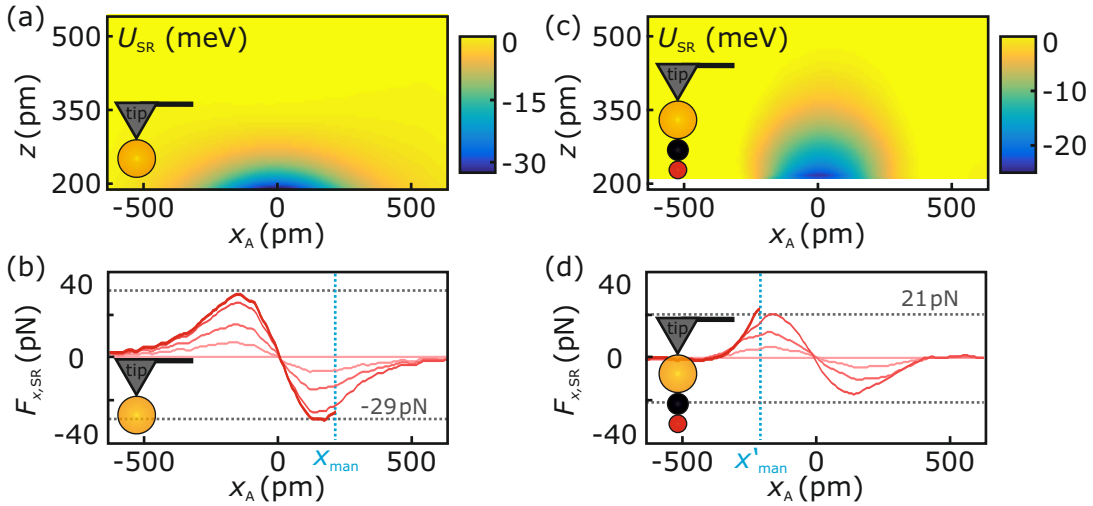

Figure 4.4. Short-range potentials $U_{\mathrm{SR}}(x_{\mathrm{A}}, z)$ between the Fe adatom and (a) the monoatomic metal tip and (b) the CO-terminated monoatomic metal tip (CO tip A) deconvoluted [74, 77] from the frequency shift $\Delta f(x, z)$ datasets presented in Fig. 4.3(a) and (d), respectively. (b) and (d) By taking the lateral derivative of the short-range potentials $U_{\mathrm{SR}}(x_{\mathrm{A}}, z)$ along the x_{A} axis the lateral force curves $F_x(x_{\mathrm{A}}, z)$ are derived (see subsection 2.2.3 for method description). The cantilever and its tip are not sketched to scale. Figure adapted from Ref. [82].

force value is called lateral force threshold [13, 67, 107] needed to be overcome to laterally manipulate the single Fe adatom on the Cu(111) surface. The lateral force trace $F_x(x_\mathrm{A}, z_{4,\mathrm{Me}})$ is slightly asymmetric with respect to $(x_\mathrm{A} = 0, F_x = 0)$: At $x_\mathrm{A} = -x_\mathrm{man}$, the lateral force value is given by 28 pN and, therefore, by 1 pN smaller than the absolute value of the lateral force threshold. Hence, the Fe adatom is not laterally manipulated at $x_\mathrm{A} = -x_\mathrm{man}$ as the lateral force acting on the Fe adatom is not sufficient to laterally manipulate it. However, after the Fe adatom is manipulated laterally to the right side by 255 pm the tip passes the adatom's center at $x_\mathrm{A} = 255\,\mathrm{pm}$ a second time. Due to the periodicity of the substrate, the lateral force value at $x_\mathrm{A} = x_\mathrm{man} + 255\,\mathrm{pm}$ after the first manipulation should be high enough such that the Fe adatom is manipulated further on to the right side. However, a second sharp change in the $\Delta f(x_\mathrm{A}, z_{4,\mathrm{Me}})$ curve is not detected experimentally. The absence of further lateral manipulation events to the right side can be explained by a small misalignment of the manipulation path with respect to the high-symmetry direction of the substrate or a local variation of the surface potential induced by e.g. a defect.

Figure 4.4(c) shows the short-range potential $U_\mathrm{SR}(x_\mathrm{A}, z)$ between CO tip A and the single Fe adatom. It is also completely attractive but laterally more confined than the short-range potential between the monoatomic metal tip and the Fe adatom shown in Fig. 4.4(a). The corresponding lateral force curves $F_x(x_\mathrm{A}, z)$ between the CO tip and the Fe adatom (see Fig. 4.4(d)) are qualitatively quite similar to the lateral force curves between the monoatomic metal tip and Fe adatom (see Fig. 4.4(b)): As the tip approaches the adatom from the left side the Fe adatom is attracted to the left side (towards the tip). After the tip passes the center of the Fe adatom an attractive lateral force acts on the adatom pointing to the right side (towards the tip). The lateral force curves $F_x\,(x_\mathrm{A}, z)$ are also asymmetric with respect to $(x_\mathrm{A} = 0, F_x = 0)$. However, the asymmetry is reversed compared to the monoatomic metal tip: The absolute values of the lateral force curves before the CO tip passes the center of the Fe adatom ($x_\mathrm{A} < 0$) are about 10% higher in absolute value compared to the absolute values after the CO tip passes the center of the Fe adatom ($x_\mathrm{A} > 0$). This is the reason why the Fe adatom is already manipulated laterally to the left side while the CO tip approaches its center from the left side. The force threshold to laterally manipulate the Fe adatom with CO tip A is 21 pN and, therefore, smaller compared to the experiment with the monoatomic metal tip.

After the Fe adatom is manipulated laterally to the left side by 255 pm the CO tip moves away from the center of the Fe adatom. As the lateral force values are 10% smaller on the right side of the Fe adatom, the adatom is not manipulated further to the right side after the tip passes the Fe adatom's center.

In summary, both tips induce an attractive lateral manipulation of the single Fe adatom (i.e. pulling). However, upon attachment of a CO molecule to the monoatomic metal tip, the asymmetry of the lateral force field reverses.

The above described lateral manipulation experiment of a single Fe adatom is repeated with another CO-terminated monoatomic metal tip (CO tip B). The corresponding $\Delta f(x_\mathrm{A}, z)$ curves are depicted for five selected tip-sample distances in Fig. 4.5(a). The comparison of these curves with the $\Delta f(x_\mathrm{A}, z)$ curves acquired with CO tip A (see Fig. 4.3(d)) reveals that the two bumps aside the center of the attractive dip at $x_\mathrm{A} = 0$ appear much more distinct in case of CO tip B. Using CO tip B, a sharp change of the $\Delta f(x_\mathrm{A}, z_\mathrm{man})$ curve occurs at $x_\mathrm{A} = x''_\mathrm{man}$ in a tip-sample distance $z_\mathrm{man} = 175\,\mathrm{pm}$ before the CO tip crosses the adatom's center ($x_\mathrm{A} < 0$). The normalized conductance curves $G\left(x_\mathrm{A}, z + 50\,\mathrm{pm}\right)/G_0$ during backtracing indicate that the Fe adatom was manipulated laterally along the $-\vec{x}_\mathrm{A}$ direction towards the fcc hollow site located at $x_\mathrm{A} = -255\,\mathrm{pm}$[1]. The short-range potential between CO tip B and the Fe adatom, depicted in Fig. 4.5(c), shows, similar to the short-range potential U_SR between CO tip A and the Fe adatom (see Fig. 4.4(c)), an attractive part located at $220\,\mathrm{pm} < z < 370\,\mathrm{pm}$ around $x_\mathrm{A} = 0$. However, the attraction between CO tip B and the Fe adatom is smaller in magnitude compared to CO tip A and the Fe adatom. Additionally, two repulsive (positive) features arise at close distances ($z < 200\,\mathrm{pm}$) at $x_\mathrm{A} = \pm 200\,\mathrm{pm}$. These vertical tip-sample distances are inaccessible with CO tip A as the Fe adatom is manipulated laterally at $z_\mathrm{4,CO} = 205\,\mathrm{pm}$. The lateral force curves $F_x(x_\mathrm{A}, z)$ between CO tip B and the Fe adatom display, as a result of the evolution of the two repulsive rims of the short-range potential U_SR, four extrema at close distances $z < 200\,\mathrm{pm}$ (see Fig. 4.5(d)). Consequently, repulsive lateral forces between CO tip B and the Fe adatom occur. However, the attractive lateral forces are higher in absolute value. Therefore, the Fe adatom is manipulated towards the tip to the left side at $x_\mathrm{A} = x''_\mathrm{man}$ while the tip approaches the center of the Fe adatom as attractive lateral forces are highest

[1] This was also observed with CO tip A.

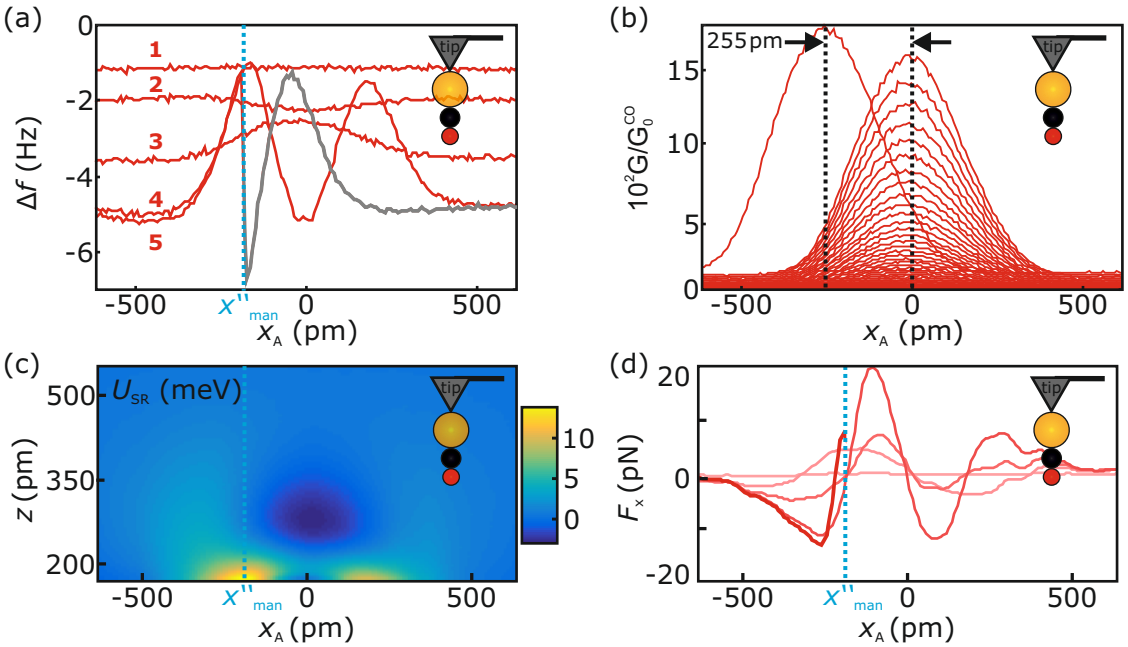

Figure 4.5. (a) Selected $\Delta f(x_\mathrm{A}, z)$ linescans during a lateral manipulation experiment of a single Fe adatom using another CO tip (CO tip B). (b) Normalized conductance curves $G\left(x_\mathrm{A}, z + 50\,\mathrm{pm}\right)/G_0$ during backtracing of the tip. The conductance trace $G\left(x_\mathrm{A}, z_\mathrm{man} + 50\,\mathrm{pm}\right)/G_0$ at a tip-sample distance of z_man, acquired after the lateral manipulation event occurred, is centered at $x_\mathrm{A} = -255\,\mathrm{pm}$. (c) The short-range potential $U_\mathrm{SR}(x_\mathrm{A}, z)$ shows, similar to U_SR between the CO tip A and the Fe adatom (shown in Fig. 4.4(c)), an attractive dip in a z distance regime between 220 pm to 370 pm. However, CO tip B can be approached to $z_\mathrm{man} = 175\,\mathrm{pm}$ before the Fe adatom is manipulated laterally and, hence, 30 pm closer than CO tip A (see Fig. 4.3 and 4.4). (d) The corresponding lateral force traces $F_x(x_\mathrm{A}, z)$ show, compared to the lateral force curves of CO tip A (see Fig. 4.4(d)), two more extrema at close distances. Here, darker lines indicate smaller tip-sample distances. The cantilever and its tip are not sketched to scale.

in absolute value for $x_\mathrm{A} < 0$. Note that the lateral manipulation position x''_man is 80 pm apart from the attractive lateral force maximum of 20 pN. A lateral force of 20 pN results in a lateral deflection of $\Delta x = 20\,\mathrm{pN}/k_x = 83\,\mathrm{pm}$. Here $k_x = 0.24\,\mathrm{N/m}$ is the torsional spring constant of a CO molecule adsorbed to a metal tip [60]. Hence, the deviation of the lateral manipulation position x''_man with respect to the maximum of the lateral force curve can be a result of the lateral deflection of the CO tip. Furthermore, the lateral force threshold of 20 pN is similar to the lateral force threshold determined with CO tip A (21 pN). In the following, CO bending is

neglected. The reason for the different appearances of the single Fe adatom using different CO tips is discussed in section 5.2.

Next, the lateral manipulation experiments are repeated along all three high-symmetry directions $\vec{x}_A$, $\vec{x}_B$ and $\vec{x}_C$ (see Fig. 4.2(a) and Fig. 4.6(b)) using two different monoatomic metal and three different CO-terminated monoatomic metal tips. In all experiments, the single Fe adatom is laterally manipulated due to an attractive interaction between each tip and the adatom (i.e. pulling as defined in Ref. [8]). Afterwards, the lateral force thresholds for lateral manipulation are determined (see Fig. 4.6(a)). Gray crosses correspond to the lateral manipulation experiments using monoatomic metal tips while black crosses correspond to CO-terminated monoatomic metal tips. Positive or negative lateral force thresholds $F_x\,(x = x_{\mathrm{man}})$ indicate whether the Fe adatom is manipulated before ($x_{\mathrm{man}} < 0$) or after ($x_{\mathrm{man}} > 0$) the tip has passed the center of the Fe adatom at $x = 0$, respectively. As all lateral

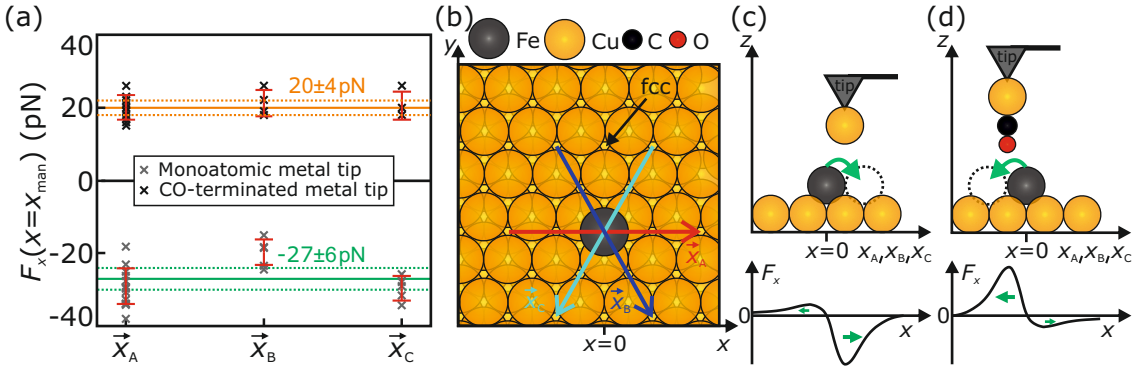

Figure 4.6. (a) Lateral force threshold values $F_x\,(x = x_{\mathrm{man}})$ at the location of lateral manipulation $x = x_{\mathrm{man}}$ using monoatomic metal tips (gray crosses) and CO-terminated monoatomic metal tips (black crosses) with respect to the manipulation direction $\vec{x}$. Each red colored error bar indicates the standard deviation of the mean value with respect to the manipulation direction and the tip termination. The solid (dashed) horizontal orange and green line indicate the mean value (standard deviation of the mean value) of the lateral force threshold with respect to the tip termination averaged over all manipulation directions. (b) The manipulation directions $\vec{x} \in \{\vec{x}_A, \vec{x}_B, \vec{x}_C\}$ match the high-symmetry directions of the Cu(111) substrate. (c) The single Fe adatom is always laterally manipulated along the positive $\vec{x}$ directions when using monoatomic metal tips (see top panel) as the lateral force field is asymmetric with respect to $x = 0$ as indicated in the bottom panel. (d) The manipulation behavior reverses after the tips are terminated with a CO molecule (see also Fig. 4.4). The cantilever and its tip are not sketched to scale in panels (c)-(d). Panel (a) is adapted from Ref. [82].

manipulation events occur in the attractive (pulling) mode a positive or negative lateral force threshold $F_x\,(x = x_{\mathrm{man}})$ indicate whether the Fe adatom is manipulated to the left (along the $-\vec{x}$ direction) or to the right side (along the $+\vec{x}$ direction), respectively.

For monoatomic metal tips, all lateral force thresholds are negative and, hence, the Fe adatom is always manipulated along positive $\vec{x}$ directions after the tips passes the adatom's center (see sketch in top panel of Fig. 4.6(c)). Therefore, the lateral force curves are higher in absolute value for tip positions $x > 0$ (see sketch in bottom panel of Fig. 4.6(c)). All CO tips show the opposite behavior: The lateral force thresholds $F_x\,(x = x_{\mathrm{man}})$ are entirely positive and, hence, the Fe adatom is always manipulated along the negative $\vec{x}$ directions as the tips approaches the adatom's center from the left side (see sketch in top panel including a sketch of the asymmetric F_x curve in the bottom panel of Fig. 4.6(d)). The average of the absolute values of the lateral force thresholds using monoatomic metal and CO-terminated monoatomic metal tips overlap: $27 \pm 6\,\mathrm{pN}$ and $20 \pm 4\,\mathrm{pN}$, respectively[1]. The diffusion barrier of a single Fe adatom on the Cu(111) surface is theoretically calculated (28.5 meV) and experimentally verified by diffusion experiments using STM ($22 \pm 7\,\mathrm{meV}$) [98]. Assuming a sinusoidal model potential, the diffusion barrier transforms into a lateral force threshold of 84.4 pN (theoretically) and $65 \pm 20\,\mathrm{pN}$ (experimentally) [109]. The lateral force thresholds using monoatomic metal tips and CO tips determined within this work are 50% to 70% smaller compared to the values experimentally reported in Ref. [98]. Emmrich *et al.* [107] discovered, by performing lateral manipulation experiments of a single CO molecule adsorbed on the Cu(111) surface using a monoatomic metal tip, that the lateral force threshold is 50% smaller than theoretically predicted. Reference [107] proposed a local lowering of the surface potential by the presence of the tip during the lateral manipulation experiment. This explanation can also be applied to the system of single Fe adatoms on Cu(111) and the above described observation that the lateral force threshold is 50% to 70% smaller compared to the results of diffusion experiments in STM [98]: As in the diffusion experiments the STM tip is positioned relatively far apart from the Fe adatom [98], the surface potential is not altered by the presence of the tip. In contrary, in the lateral manipulation experiments the tip is relatively close to

[1] This value is similar to the lateral force threshold of $17 \pm 3\,\mathrm{pN}$ to laterally manipulate a single Co adatom on the Cu(111) surface [13].

the surface as well as to the adatom and, hence, can induce a local lowering of the surface potential as proposed by Emmrich *et al.* for single CO molecules on Cu(111) [107].

4.4. Determination of the Tip's Tilt Direction

In the following, the reason for the asymmetric lateral force curves $F_x(x, z)$, presented in section 4.3, is discussed. In this thesis, the monoatomic metal tip[1] and the CO tip are selected as they exhibit a radial symmetry at their apexes (see section 3.4). However, the tips can possess an intrinsic tilt. For instance, the tilt can be a consequence of a small misalignment of the complete tip wire with respect to the normal vector of the surface. In order to study the tips' tilt, a constant-height $\Delta f(x, y)$ image of a single Fe adatom using a CO-terminated monoatomic metal tip and a COFI image of the monoatomic metal tip before functionalization is investigated (see section 3.4 for a description of the COFI technique).

Single Fe and Cu adatoms adsorbed on Cu(111) appear in the $\Delta f(x, y)$ image as bright tori with a dark center imaged in constant-height mode with CO tips at close tip-sample distances [33] (as shown for the single Fe adatom in Fig. 4.7(a) and (b)). Figure 4.7(c) depicts the side view of the experimental setup. If the torus is interpreted as an intrinsic property of the single adatom which is oriented parallel to the surface it is imaged completely in constant-height mode even if the CO tip is slightly tilted. The experimental setup for acquiring COFI images is reversed: A single CO molecule, adsorbed on a top site of the Cu(111) surface (see Fig. 4.7(d)), is scanned in constant-height mode using a metal tip. In the COFI setup, the single CO molecule effectively acts as the probe resolving the tip's apex on the atomic scale [92, 110]. In case of non-tilted monoatomic metal tips, the COFI image ($\Delta f(x, y, z = \text{const.})$) shows, at close tip-sample distances, a closed torus, similar to the reversed measurement shown in Fig. 4.7(b). The COFI image of the monoatomic metal tip, used for laterally manipulating a single Fe adatom on Cu(111), shows a bright sickle in the top part of the image which is centered around an attractive dip (see Fig. 4.7(e)). This clearly indicates that the tip is terminated

[1] In the following it is assumed that the presented monoatomic metal tips are terminated by a single Cu atom as the tips were repeatedly poked into the clean Cu(111) sample for tip preparation purposes.

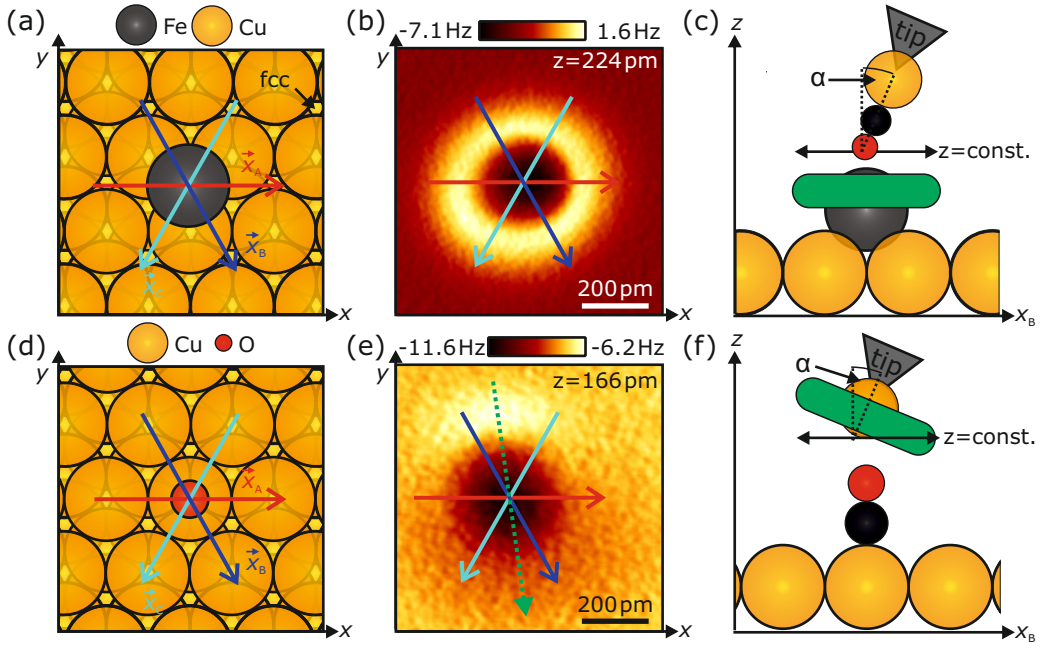

Figure 4.7. (a) Sketch of a Fe adatom adsorbed on the Cu(111) surface (top view). (b) Frequency shift image $\Delta f\,(x, y)$ of a single Fe adatom acquired with a CO tip in constant-height mode showing an almost radial symmetric torus [33, 42]. Single Cu adatoms also appear as tori when scanned in constant-height mode using CO tips [33]. (c) If the torus is interpreted as an intrinsic property of the adatom, it is completely imaged in constant-height at close distances z in the Δf image, even if the CO tip is slightly misaligned by an angle α with respect to the surface normal. (d) Sketch of a single CO molecule adsorbed on a top site of the Cu(111) surface (top view). (e) The COFI image ($\Delta f(x, y, z = \text{const.})$) of a monoatomic metal tip used to laterally manipulate a single Fe adatom shows a bright sickle in the top part of the image which is interpreted as a torus segment of the frontmost atom of the tip. The green dotted arrow points in the direction of highest asymmetry. (f) Sketch of the COFI setup using a tilted monoatomic metal tip (tilt angle α, side view). The reversed setup as shown in panel (c) also results in the appearance of a torus in the Δf image using monoatomic metal tips (Fe and Cu terminated) at small distances z [92]. However, if the torus is described as an intrinsic property of the tip's frontmost atom, the torus is not necessarily imaged completely in case that the tip's tilt angle α is getting too large. Figure adapted from Ref. [82].

by a single metal atom [33, 92, 110]. The bright sickle originates from the top of a tilted torus. If the torus is interpreted as an intrinsic property of the single frontmost atom of the tip, the presence of the sickle and absence of the closed torus can be understood in a pure geometric fashion (see sketch in Fig. 4.7(f)): If the tip is tilted by an angle α along an axis indicated by the green dotted arrow in Fig.

4.7(e), the torus of the frontmost atom is not oriented parallel to the surface plane. Therefore, only a segment of the torus is imaged during the COFI measurement. In theory, a further reduction of the tip-sample distance results in the appearance of the complete torus in the COFI image. However, experimentally the distance cannot be reduced further without laterally manipulating the single CO molecule on the Cu(111) surface (see also Ref. [107]).

Both COFI images of the two monoatomic metal tips that are used to laterally manipulate a single Fe adatom show a bright sickle and an asymmetry in the very same direction (indicated by the green dotted arrow in Fig. 4.7(e) for one tip). Hence, both tips are tilted along the same axis defined by the green dotted arrow. As the angles between the green dotted arrow and the high-symmetry directions $\vec{x}_{\mathrm{A}}$, $\vec{x}_{\mathrm{B}}$ and $\vec{x}_{\mathrm{C}}$ are smaller than 90° (see Fig. 4.7(e)), the monoatomic metal tips are tilted to the right side for all three high-symmetry directions (as sketched in Fig. 4.7(f) for the $\vec{x}_{\mathrm{B}}$ direction and sketched in Fig. 4.8 for all manipulation directions).

After conducting the lateral manipulation experiments, both monoatomic metal tips are terminated with a single CO molecule and the COFI measurements as well as the lateral manipulation experiments of single Fe adatoms are repeated. Both COFI images show an asymmetry along the very same direction as the monoatomic metal tips as indicated by the green dotted arrow in Fig. 4.7(e)[1]. Hence, it can be suggested that the CO molecule adsorbs to the monoatomic metal tip such that the symmetry of the tip is conserved. This assumption is supported by the observation that COFI images of many other monoatomic metal tips before and after CO termination typically exhibit asymmetries in the same direction. Furthermore, it is found during this thesis that the asymmetry axis does not change for various different tips if the same qPlus sensor is used, although relatively deep tip pokes took place in the meantime[2]. Therefore, it can be assumed that the tip tilt is a direct result of a macroscopic misalignment of the tip wire with respect to the surface normal of the Cu(111) surface along the very same axis as indicated by the green dotted arrow in Fig. 4.7(e). This could be a result of the sensor holder design which is tilted by 3° with respect to the Cu(111) plane [90].

[1] The COFI image of the second monoatomic metal prior and after CO-termination is not shown here.

[2] Typically the tip is poked hundreds of picometers to tens of nanometers into the Cu crystal to alter the tip apex (see section 3.4).

In summary, all monoatomic metal tips and CO-terminated monoatomic metal tips which were used for the lateral manipulation experiments are tilted along the direction indicated by the green dotted arrow so that the tilted part of the tip points to the positive $\vec{x}_{\mathrm{A}}$, $\vec{x}_{\mathrm{B}}$ and $\vec{x}_{\mathrm{C}}$ directions (see Fig. 4.8). Here, the tilt angle α along the $\vec{x}_{\mathrm{A}}$ direction is smaller than the tilt angle α' along the $\vec{x}_{\mathrm{B}}$ and $\vec{x}_{\mathrm{C}}$ direction because the angle between $\vec{x}_{\mathrm{A}}$ and the asymmetry axis (see green dotted arrow in Fig. 4.7(e)) is larger than the angle between $\vec{x}_{\mathrm{B}}$ and the asymmetry axis similar to the angle between $\vec{x}_{\mathrm{C}}$ and the asymmetry axis (see Fig. 4.8).

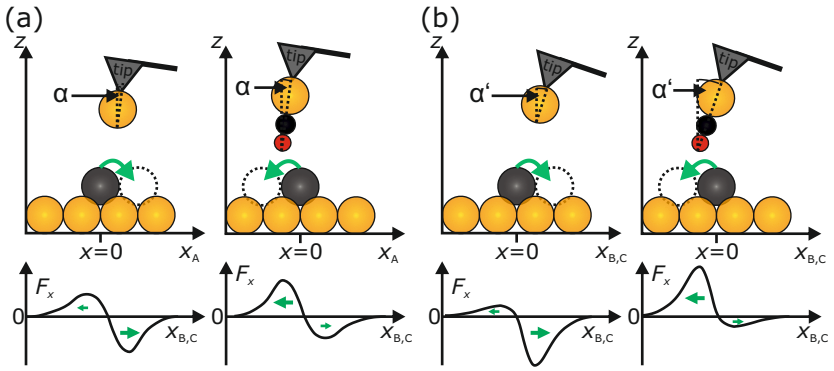

Figure 4.8. (a) Sketch of the tilt of the monoatomic metal tips and CO tips used to laterally manipulate single Fe adatoms projected in the zx_{A} plane (top panels). The tip tilt angle α induces a small asymmetry in the lateral force curves as sketched in the two bottom panels. The influence of the tip's tilt is reversed before and after terminating a monoatomic metal tip with a CO molecule. In case of the monoatomic metal tips, the lateral forces are higher in absolute value if the tilted part of the tip is pointing away from the adatom ($x_{\mathrm{A}} > 0$). After terminating the tip with a CO molecule, the asymmetry is reversed. (b) The tilt angle α' projected in the zx_{B} and zx_{C} plane is larger than the tilt angle α projected in the zx_{A} plane as the angle between $\vec{x}_{\mathrm{B}}$ or $\vec{x}_{\mathrm{C}}$ and the green dotted arrow is significantly smaller than between $\vec{x}_A$ and the green dotted arrow shown in Fig. 4.7(e) (top panels). The asymmetries in the lateral force curves are, therefore, larger along the $\vec{x}_{\mathrm{B}}$ and $\vec{x}_{\mathrm{C}}$ directions compared to the $\vec{x}_{\mathrm{A}}$ direction (bottom panels). The cantilever and its tip are not sketched to scale.

4.5. Analytic Model Using Van-der-Waals and Electrostatic Interactions

Next, an analytic model is used in order to gain insight to the physical origin of the reversed behavior of CO tips with respect to monoatomic metal tips when laterally manipulating single Fe adatoms. Within the model, the interaction between the tip and the Fe adatom is investigated in the xz plane. The model takes van-der-Waals and electrostatic interactions between a two-dimensional tip consisting of N atoms and a single Fe adatom into account. The interaction between the Cu substrate and the tip is neglected as it was subtracted in the experimental analysis as well.

Figure 4.9 depicts the side view of the model tip and the Fe adatom. The metal part of the monoatomic metal tip (see Fig. 4.9(a)) and CO-terminated monoatomic

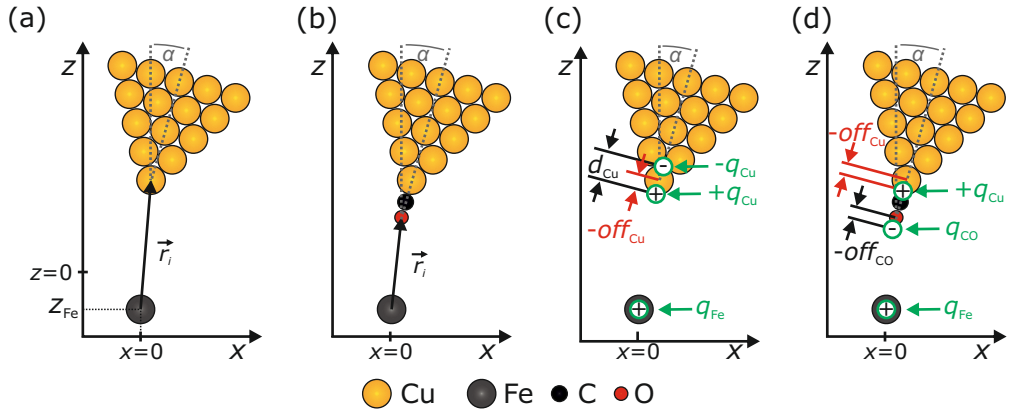

Figure 4.9. (a) Side view of the analytic setup in case of the monoatomic metal tip. The tip consists of 15 Cu atoms arranged in a pyramidal shape and can be tilted by an angle α. The Fe atom is located at $x = 0$ and $z_{\mathrm{Fe}} = -121\,\mathrm{pm}$ (see text). (b) In case of the CO-terminated monoatomic metal tip, an additional CO molecule is attached to the frontmost atom of the pyramidal metal tip. (c) Electrostatic interactions are enabled by placing point charges on specific locations: The Fe adatom is carrying a charge of $q_{\mathrm{Fe}} = 0.1\,e$. The metal tip's dipole [111] is modeled by two charges $\pm q_{\mathrm{Cu}} = \pm 0.13\,e$ with opposite sign separated by $d_{\mathrm{Cu}} = 135\,\mathrm{pm}$ [81]. Here, the positive charge is placed in the center of the metal tip's frontmost atom ($off_{\mathrm{Cu}} = 0$). (d) The CO molecule carries a negative charge of $q_{\mathrm{CO}} = -0.03\,e$ [81] which is offset by $off_{\mathrm{CO}} = -100\,\mathrm{pm}$ with respect to the O atom's center [39]. Figure adapted from Ref. [82].

metal tip (see Fig. 4.9(b)) consists of 15 Cu atoms[1] positioned in pyramidal order. The interatomic distance between the Cu atoms is set to the bulk lattice constant of Cu ($a_{\mathrm{Cu}} = 361\,\mathrm{pm}$). In case of the CO tip, an additional CO molecule is fixed with its C atom to the frontmost Cu atom of the metal tip (see Fig. 4.9(b)). The distance between the center of the C atom and the center of the frontmost Cu atom of the metal tip is set to $r_{\mathrm{C}} + r_{\mathrm{Cu}} = 70\,\mathrm{pm} + 135\,\mathrm{pm} = 205\,\mathrm{pm}$. The core of the O atom and the core of the metal tip's frontmost Cu atom are separated by $r_{\mathrm{O}} + 2r_{\mathrm{C}} + r_{\mathrm{Cu}} = 60\,\mathrm{pm} + 2 \cdot 70\,\mathrm{pm} + 135\,\mathrm{pm} = 335\,\mathrm{pm}$. Here, r_{C}, r_{Cu} and r_{O} are the atomic radii of C, Cu and O, respectively. Both tips can be tilted by an angle α.

The potential U_{vdW} between a single Fe adatom and a tip arising from van-der-Waals interaction can be written as [53, 112]:

$$U_{\mathrm{vdW}} = -\sum_{i=1}^{N} \frac{C_{6,spec(i),\mathrm{Fe}}}{r_{i,\mathrm{Fe}}^{6}} \tag{4.1}$$

Here, $r_{i,\mathrm{Fe}} = |\vec{r}_{i,\mathrm{Fe}}| = \sqrt{(x_{i,\mathrm{Fe}})^2 + (z_{i,\mathrm{Fe}})^2}$ describes the distance between the centers of the interacting atoms (see Fig. 4.9(a) and (b)) while $C_{6,spec(i),\mathrm{Fe}}$ is an elemental-specific parameter which can be calculated for various atomic pairings [54]. The relevant $C_{6,spec(i),\mathrm{Fe}}$ coefficients are shown in table 4.1 [54].

Interaction pair k	Cu,Fe	C,Fe	O,Fe	Cu,C	Cu,O
$C_{6,k}[10^{77}\,\mathrm{Jm}^6]$	3.64	1.42	0.73	0.99	0.50

Table 4.1. $C_{6,k}$ coefficients as a function of interaction partner k used to model the attractive van-der-Waals interaction between the single Fe adatom and the individual atoms of the model tip [54].

Both the monoatomic metal tip and the Fe adatom exhibit an electric dipole, due to the Smoluchowski effect [111]. The lateral manipulation experiments are performed at tip adatom distances of few hundreds picometers and, hence, the electrostatic interaction cannot be modeled via dipole-dipole interaction. Therefore, the electrostatic interaction is calculated using point charges. The dipole of the monoatomic metal tip is expressed by two point charges of $\pm q_{\mathrm{Cu}} = \pm 0.13\,e$ with opposite sign separated by $d_{\mathrm{Cu}} = 135\,\mathrm{pm}$ while the positive charge is placed at the

[1] In the experiment, the tip was repeatedly poked into the clean Cu surface for tip sharpening and shaping purposes. Hence, the tip's apex is likely to be covered with Cu atoms.

core of the tip's frontmost Cu atom [81] ($off_{\mathrm{Cu}} = 0$, see Fig. 4.9(c)). A charge of $q_{\mathrm{Fe}} = +0.10\,e$ is placed in the center of the Fe atom. The CO molecule of an CO-terminated tip carries a negative charge of $q_{\mathrm{CO}} = -0.03\,e$ [81]. Here, the charge is placed by $off_{\mathrm{CO}} = -100\,\mathrm{pm}$ off-center the O atom towards the Fe atom as it was found that the electric field of a CO tip is maximal 100 pm in front of the core of the CO tip's O atom [39]. In case of the CO tip, the influence of the negative charge $-q_{\mathrm{Cu}} = -0.13\,e$, arising from the metal tip background, onto the electrostatic interaction is neglected. The electrostatic potential U_{ES} between the model tips and the Fe adatom is given by the Coulomb interaction:

$$U_{\mathrm{ES}} = +\frac{1}{4\pi\epsilon_0}\sum_{i=1}^{N}\frac{q_{\mathrm{Fe}}q_{\mathrm{spec(i)}}}{r_{i,\mathrm{Fe}}} \tag{4.2}$$

The coordinate system is chosen such that it matches the experimental coordinate system. In the experiment, $z = 0$ corresponds to a conductance of G_0 (monoatomic metal tip) or G_0^{CO} (CO tip), respectively. At $z = 0$, the shell of the tip's frontmost atom (Cu or O) is still separated by $\Delta_{\mathrm{DFT}} = 172\,\mathrm{pm}$ from the shell of an Cu atom of the topmost Cu layer [80] (see subsection 2.3.1) and, therefore, the core of a Cu atom of the topmost layer of the substrate is located at $z = 0 - \Delta_{\mathrm{DFT}} - r_{\mathrm{Cu}} = -307\,\mathrm{pm}$. Using the adsorption height of the Fe adatom of $h = 186\,\mathrm{pm}$ [83] results in the z position of the core of the Fe atom $z_{\mathrm{Fe}} = -121\,\mathrm{pm}$ (see Fig. 4.9(a)). Hence, the Fe adatom is placed at $(x = 0, z = -121\,\mathrm{pm})$ in the analytic model. After calculating the van-der-Waals U_{vdW} and electrostatic U_{ES} potential between the model tips and the Fe adatom, the corresponding lateral force curves $F_{x,\mathrm{vdW}}(x,z)$ and $F_{x,\mathrm{ES}}(x,z)$ are obtained via $F_{x,i}(x,z) = -\partial U_i(x,z)/\partial x$.

Figure 4.10(a) and (b) show the calculated lateral force curves arising from van-der-Waals interaction ($F_{x,\mathrm{vdW}}(x,z)$) and electrostatic interaction ($F_{x,\mathrm{ES}}(x,z)$) and the sum of both curves ($F_{x,\mathrm{vdW}}(x,z) + F_{x,\mathrm{ES}}(x,z)$) for the closest approach in the experiments of the monoatomic metal tip ($z_{4,\mathrm{Me}} = 186\,\mathrm{pm}$) and the CO-terminated tip ($z_{4,\mathrm{CO}} = 205\,\mathrm{pm}$), respectively (see also Fig. 4.3). The tilt of both tips ($\alpha = 20°$) leads to the same asymmetry in the lateral force curve $F_{x,\mathrm{vdW}}(x)$ arising from van-der-Waals interaction (light blue dotted curves): The absolute values of $F_{x,\mathrm{vdW}}(x)$ are higher in absolute value when the tilted part of the tips are pointing away from the center of the Fe atom, i.e. if the tip is positioned at positive x values

($x > 0$, $|\max(F_{x,\mathrm{vdW}})| < |\min(F_{x,\mathrm{vdW}})|$). The resulting lateral force curves due to pure electrostatic interaction ($F_{x,\mathrm{ES}}(x)$) show a reversed behavior: The Coulomb interaction leads to a repulsive interaction between monoatomic metal tip and Fe atom while it results in additional attraction between the CO tip and the Fe atom (red dotted curves). This leads to a reversed asymmetry of the sum of the lateral force curves $F_{x,\mathrm{vdW}}(x) + F_{x,\mathrm{ES}}(x)$ in case of the CO tip compared to the monoatomic metal tip (solid black curves). In case of the monoatomic metal tip, the lateral forces $F_{x,\mathrm{vdW}}(x) + F_{x,\mathrm{ES}}(x)$ are higher in absolute value if the tilted part of the tip is pointing away from the Fe atom, i.e. for tip positions $x > 0$. This agrees with the asymmetry observed in the experiment (see Fig. 4.4(b)). In case of the CO tip, the lateral forces $F_{x,\mathrm{vdW}}(x) + F_{x,\mathrm{ES}}(x)$ are higher if the tilted part of the tip is pointing towards the Fe atom, i.e. tip positions $x < 0$. This also matches with the experimental finding shown in Fig. 4.4(d). In summary, the reversed dipole of the CO tip with respect to the monoatomic metal tip causes in the inversion of the asymmetry of the lateral force curves. The maxima of the absolute value of the lateral force curves $\max(|F_{x,\mathrm{vdW}}(x) + F_{x,\mathrm{ES}}(x)|)$ of the monoatomic metal and the CO tip are given by 13.6 pN and 11.4 pN, respectively, and, hence, are quite similar. However, the values are about 60% (monoatomic metal tip) and 50% (CO tip) smaller compared to the experimentally determined values of 27 ± 6 pN

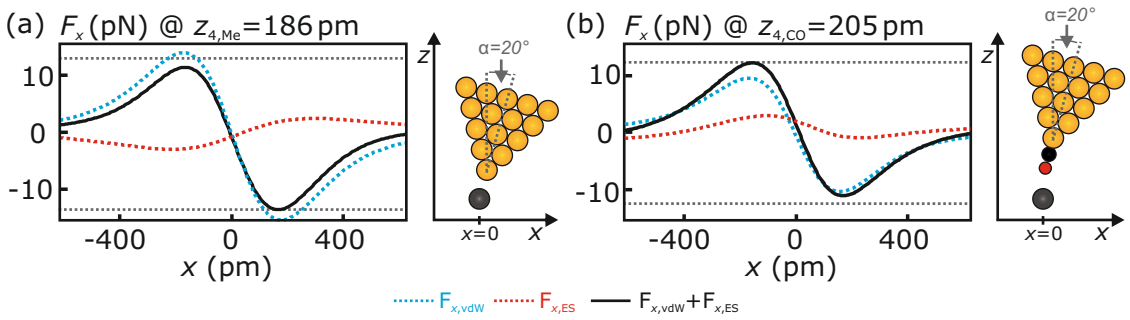

Figure 4.10. (a) Calculated lateral force curves for pure van-der-Waals interaction ($F_{x,\mathrm{vdW}}(x,z)$), pure electrostatic interaction ($F_{x,\mathrm{ES}}(x,z)$) and the sum of van-der-Waals and electrostatic interaction ($F_{x,\mathrm{vdW}}(x,z) + F_{x,\mathrm{ES}}(x,z)$) between the monoatomic metal tip and the Fe atom for the tip position $z_{4,\mathrm{Me}} = 186$ pm (left panel). The model tip's tilt is set to $\alpha = 20°$ (right panel). (b) Calculated lateral force curves $F_{x,\mathrm{vdW}}(x,z)$, $F_{x,\mathrm{ES}}(x,z)$ and $F_{x,\mathrm{vdW}}(x,z) + F_{x,\mathrm{ES}}(x,z)$ between a Fe atom and a tilted CO-terminated metal tip ($\alpha = 20°$, see right panel) for a tip-sample distance of $z_{4,\mathrm{CO}} = 205$ pm. Figure adapted from Ref. [82].

(monoatomic metal tip) and $20 \pm 4\,\mathrm{pN}$ (CO tip). These deviations originate from the usage of a two-dimensional tip in the analytic model compared to the three-dimensional tip in the experiment.

In order to evaluate the robustness of the above described analytic model with respect to the input parameters, the parameters are varied while the sum of the two extrema of the lateral force curve $\Delta F_x = \max(F_x) + \min(F_x)$ is observed. If ΔF_x is positive, the absolute value of the maximum lateral force is larger than the absolute value of the minimum lateral force. Positive lateral forces occur for tip positions $x < 0$ while negative lateral forces are present for $x > 0$ as the lateral forces between model tip and Fe atom are purely attractive (see Fig. 4.10). Hence, if ΔF_x is positive, the lateral force is larger in absolute value for tip positions $x < 0$ (as for the CO tip in Fig. 4.10(b)). In case ΔF_x is negative, the lateral force is larger in absolute value for tip positions $x > 0$ (as for the monoatomic metal tip in Fig. 4.10(a)).

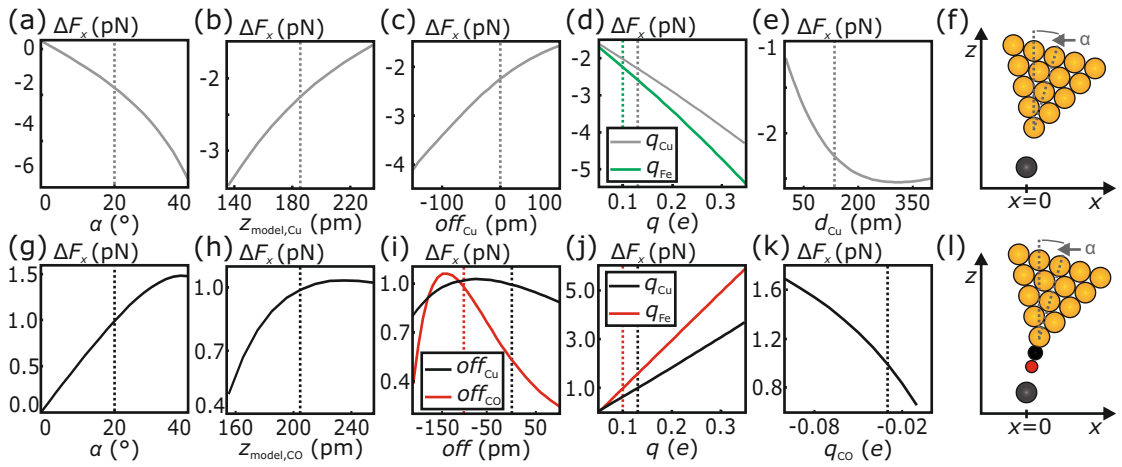

Figure 4.11. The robustness of the analytic model is studied by varying the input parameters and observing the sum of the two extrema of the calculated lateral force curve $\Delta F_x = \max(F_x) + \min(F_x)$. In case of the monoatomic metal tip (see panel (f)), the resulting $\Delta F_x = \max(F_x) + \min(F_x)$ curves are plotted against (a) α, (b) $z_{\mathrm{model,Cu}}$, (c) off_{Cu}, (d) q_{Cu} and q_{Fe} and (e) d_{Cu}. When modeling the CO tip, $\Delta F_x = \max(F_x) + \min(F_x)$ is investigated in dependence of variations of (g) α, (h) $z_{\mathrm{model,CO}}$, (i) off_{Cu} and off_{CO}, (d) q_{Cu} and q_{Fe} and (e) q_{CO}. The vertical dotted lines indicate the parameters used for the calculation in Fig. 4.10. Figure adapted from Ref. [82].

Figure 4.11(a) shows ΔF_x as a function of the tip's tilt angle α in case of the monoatomic metal tip. ΔF_x is negative (or zero for $\alpha = 0$) when changing α in a range from 0° to 40°. Hence, the lateral force is always larger in absolute value when the tilted part of the tip is facing away from the atom (i.e. for tip positions $x > 0$). The vertical gray dotted line indicates the tilt angle $\alpha = 20°$ used to calculate the lateral force profile presented in Fig. 4.10(a). Figure 4.11(b) depicts the resulting ΔF_x curve when changing the tip-sample distance $z_{\mathrm{model,Cu}}$ of the model in a range of $z_{\mathrm{model,Cu}} = [z_{4,\mathrm{Me}} - 50\,\mathrm{pm}, z_{4,\mathrm{Me}} + 50\,\mathrm{pm}]$. Within this range, ΔF_x is entirely negative. The same holds true when varying $\mathit{off}_{\mathrm{Cu}}$ within $\mathit{off}_{\mathrm{Cu}} = [-150\,\mathrm{pm}, 100\,\mathrm{pm}]$, q_{Cu} and q_{Fe} within $q_{\mathrm{Cu}}, q_{\mathrm{Fe}} = [0.05\,e, 0.35\,e]$ and d_{Cu} within $d_{\mathrm{Cu}} = [0\,\mathrm{pm}, 400\,\mathrm{pm}]$ (see Fig. 4.11(c)-(e)). The analytic model produces, therefore, a robust result regarding the asymmetry of the lateral force curves in case of the monoatomic tip (see Fig. 4.11(f)).

In case of the CO tip, the lateral force curve is larger in absolute value when the tilted part of the tip is facing towards the Fe adatom, i.e. for tip positions $x < 0$ (see Fig. 4.10(b)). When changing the tilt angle α of the tip between 0° and 40° the sum of the two extrema of the lateral force curve ΔF_x is positive or zero (for $\alpha = 0$) and, hence, the above described asymmetry of the lateral force curve persists (see Fig. 4.11(g)). ΔF_x is also entirely positive when varying the input parameters as follows (see Fig. 4.11(h)-(k)):

$$
\begin{aligned}
&z_{\mathrm{model,CO}} = [z_{4,\mathrm{CO}} - 50\,\mathrm{pm}, z_{4,\mathrm{CO}} + 50\,\mathrm{pm}] \\
&\mathit{off}_{\mathrm{Cu}}, \mathit{off}_{\mathrm{CO}} = [-200\,\mathrm{pm}, 100\,\mathrm{pm}] \\
&q_{\mathrm{Cu}}, q_{\mathrm{Fe}} = [0.05\,e, 0.35\,e] \\
&q_{\mathrm{CO}} = [-0.10\,e, -0.01\,e]
\end{aligned}
$$

The asymmetry of the lateral force curve using the CO model tip (see Fig. 4.11(l)) is, therefore, also robust with respect to variation of the input parameters.

In summary, the analytic model that describes the physical origin of the reversed lateral manipulation behavior between monoatomic metal and CO tip is robust with respect to variations of the input parameters. Hence, it can be concluded that the reversed electric dipoles of the two different tips are responsible for the reversed lateral manipulation behavior.

4.6. Creation of Small Fe Clusters Atom by Atom Using CO-Terminated Tips

As shown in section 4.3, reproducible lateral manipulation of single Fe adatoms using CO tips is possible. In this section, the knowledge about the lateral manipulation mechanism is applied in order to investigate whether small Fe clusters can be assembled atom by atom using CO tips. This would be beneficial as the Fe cluster could then be studied after each addition of a single atom on the atomic scale[1] using the very same tip and, hence, the next single atom can be added with atomic precision.

Figure 4.12(a) shows a topographic image[2] $z(x, y)$ of five individual Fe adatoms adsorbed on the Cu(111) surface acquired with a CO tip. For clarity, the single Fe adatoms are labeled with numbers from 1 to 5. Afterwards, the Fe atom number 5 is imaged in constant-height mode. The corresponding frequency shift image $\Delta f(x, y)$ (see Fig. 4.12(f)) shows a toroidal structure. The reason for the appearance of a single Fe adatom as a torus when imaged with a CO tip is described in Ref. [42] and is discussed in chapter 5. Thereafter, Fe adatoms 1 and 2 are pulled together using lateral manipulation with the same CO tip. Hereby, the CO tip is laterally moved in constant-height along an axis connecting the centers of the Fe atoms 1 and 2 (as indicated by the red arrow in Fig. 4.12(a)) and the tip-sample distance is set such that the lateral force threshold for lateral manipulation of a single Fe adatoms is overcome. In that way, the two individual Fe adatoms are approached to about 1 nm with respect to each other. However, a further approach of the two individual Fe atoms is not possible without further reducing the tip-sample distance as otherwise both atoms are laterally manipulated along the same lateral direction[3]. The need for further decreasing the tip-sample distance can be explained by the increased total energy barrier which needs to be overcome in order to form a two-atom Fe cluster (Fe dimer). This energy barrier is given by 59 meV and, therefore, it is by 20.5 meV larger than the potential barrier which needs to be overcome for laterally manipulating a single Fe adatom on the bare Cu(111) surface

[1] This is not possible with a metal tip as it does not provide atomic resolution on small Fe clusters [20].

[2] The filtering of the images was realized by using the software package WSxM 5.0 Develop 8.1, Nanotec Electronica S.L., Madrid, Spain [113].

[3] This observation is discussed in more detail in the bachelor thesis of Stilp [114].

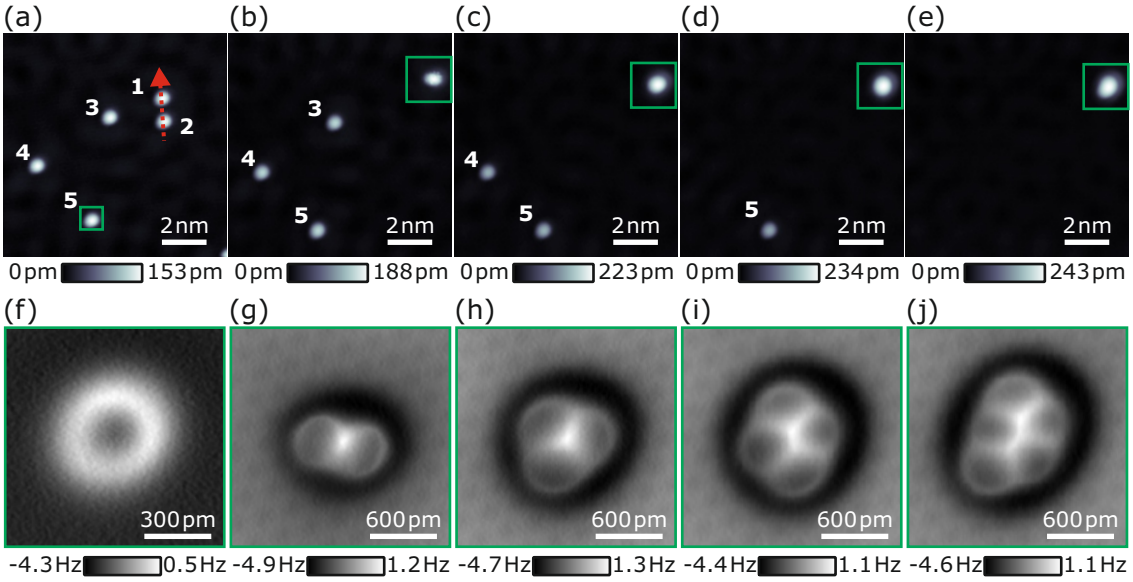

Figure 4.12. (a)-(e) Topographic images $z(x, y)$ of the same area showing five atoms in various configurations on the Cu(111) surface. In-between each image, a compact cluster is assembled atom by atom using the five individual Fe adatoms. (f)-(j) Atomically resolved frequency shift images $\Delta f(x, y)$ of the areas indicated by the green square in panels (a) through (e). The $\Delta f(x, y)$ images show a single Fe adatom (monomer, panel (f)), a two-atom Fe cluster (dimer, panel(g)), a three-atom Fe cluster (trimer, panel(h)), a four-atom Fe cluster (tetramer, panel(i)) and a five-atom Fe cluster (pentamer, panel(j)). The topographic images presented in panels (a) through (e) and the frequency shift images depicted in panels (f) to (j) are slightly smoothed using a Gaussian filter (filter width 2 px × 2 px and 4 px × 4 px applied to the 256 px × 256 px raw images, respectively). Imaging parameters: $V_{\text{tip}} = -10\,\text{mV}$ and $\langle I \rangle = 10\,\text{pA}$ (topographic images), $V_{\text{tip}} = -10\,\text{mV}$ and $\langle I \rangle = 300\,\text{pA}$ (frequency shift images). The single Fe atom shown in panel (f) is scanned in constant-height mode. Figure adapted from Ref. [82].

(28.5 meV) [98]. After further reducing the tip-sample distance, the two Fe atoms are successfully pulled together (see Fig. 4.12(b)) and, afterwards, imaged with atomic resolution in constant-current mode (see Fig. 4.12(g)). The constant-current mode allows simultaneously resolving small Fe clusters and the Cu(111) substrate on the atomic scale[1] [33]. The created Fe dimer appears instable in the topographic image (see Fig. 4.12(b)). A similar behavior (i.e. instability) was observed in case of a Cu dimer on Cu(111). The instability of the Cu dimer was attributed to a switching of the Cu dimer between two or more stable adsorption configurations [115]. The

[1]Note that the Cu(111) lattice is rotated by 16° anticlockwise with respect to the horizontal axis.

atomically resolved frequency shift image $\Delta f(x, y)$, shown in Fig. 4.12(g), does not show an instability. However, this image is acquired at a higher conductance setpoint ($\langle G \rangle = 300\,\mathrm{pA}/10\,\mathrm{mV}$) compared to the topographic image shown in Fig. 4.12(b) ($\langle G \rangle = 10\,\mathrm{pA}/10\,\mathrm{mV}$). The higher conductance setpoint approaches the CO tip closer to the Fe dimer[1] probably stabilizing the Fe dimer at one adsorption site due to the presence of the tip. The Fe dimer appears in the Δf image as a sum of two tori with positive frequency shift in-between the individual atoms. The individual Fe atoms adsorb in an asymmetric fashion close to bridge sites [33]. Figure 4.12(c) shows the same scan frame as Fig. 4.12(b) after Fe atom 3 was pulled inside the Fe dimer. The frequency shift image, recorded in constant-current mode, shows the assembled three-atom cluster (Fe trimer) with atomic resolution (see Fig. 4.12(h)). The Fe trimer is centered around a Cu surface atom while the individual atoms adsorb close to bridge sites. Experimentally, two more stable adsorption geometries of Fe trimer are found [33]: In both cases the individual Fe atoms adsorb in fcc hollow sites while they are centered either around a hcp hollow site or around a top position. DFT calculations revealed that the adsorption in fcc hollow sites centered around a hcp hollow site is energetically most favorable. The adsorption close to bridge sites (in fcc hollow sites) and centered around a top position is by 27 meV (69 meV) less energetically favorable than a fcc site adsorption geometry centered around a hcp site [33]. Figures 4.12(d) and (e) depict the topographic images of the same area as Figs. 4.12(a)-(c) after adding the Fe atoms 4 and 5 to the Fe cluster, respectively. The apparent height of the assembled Fe cluster increases with increasing cluster size from 153 pm to 243 pm. Figures 4.12(i) and (j) show the corresponding Δf images of the created four-atom and five-atom Fe cluster (tetramer and pentamer). The individual atoms of the Fe tetramer and the Fe pentamer adsorb on fcc hollow sites as fcc adsorption is energetically most favorable for Fe clusters consisting of more than two atoms [33].

In general, an atomically precise assembly of the Fe cluster is made possible by using a CO tip to attach each Fe atom to the existing Fe cluster. However, when adding the fourth Fe atom to the Fe trimer, the Fe cluster reconfigures. The reconfiguration is neccessary as the Fe atoms of Fe trimer adsorb close to bridge sites while the lowest energy adsorption geometry of Fe tetramers is fcc hollow

[1] An increase in conductance of a factor of 30 reduces the tip-sample distance by $\Delta z = -\ln(30)/2\kappa = -170\,\mathrm{pm}$ assuming a κ value of $\kappa = 1 \cdot 10^{10}\,\mathrm{m}^{-1}$ (see equation 2.16 in chapter 2).

site adsorption [33]. When adding more Fe atoms to the tetramer, the adsorption geometry of the cluster does not change anymore and, hence, an additional Fe atom can be added at a specific location of an existing Fe cluster.

So far, CO tips have been considered to be relatively sensitive and fragile as they deflect laterally quite easily due to their small lateral stiffness [60, 63, 108]. Hence, CO tips are treated in experiments with great care in order to prevent tip destruction. As briefly mentioned above, the same CO tip was used for the atom-by-atom assembly of the Fe clusters and to image them on the atomic scale in-between each enlargement step without a noticeable change of the behavior of the CO tip[1]. In order to prove that the CO tip does not change during the creation of the Fe pentamer, conductance $\langle G \rangle$ and frequency shift Δf versus distance z spectra are acquired above and besides a single CO molecule adsorbed on the Cu(111) surface before and after the assembly of the Fe pentamer shown in Fig. 4.12. Figure 4.13(a) and (b) depict the tunneling current images $\langle I(x,y) \rangle$ of a single CO molecule before and after the Fe pentamer creation, respectively. Both images show a Gaussian shaped protrusion surrounded by a characteristic halo [31, 116]. The two $\langle I(x,y) \rangle$ images are qualitatively and quantitatively[2] identical. The distance-dependent conductance traces $G(z)/G_0^{\mathrm{CO}}$ which are shown in Fig. 4.13(c), are recorded above the center of the CO molecule (light blue and green curve) and above the bare Cu(111) surface (red and black curve), respectively. The corresponding $G(z)/G_0^{\mathrm{CO}}$ curves recorded on the CO molecule and on the Cu(111) substrate before and after the pentamer assembly overlay, respectively. The residuals $G_{\mathrm{CO,before}} - G_{\mathrm{CO,after}}$ and $G_{\mathrm{Cu(111),before}} - G_{\mathrm{Cu(111),after}}$ normalized with respect to the conductance at point contact G_0^{CO} lie within the noise level of the tunneling current amplifier (see Fig. 4.13(d)). Therefore, no sign of a tip change is arising when investigating the conductance traces before and after assembling the Fe pentamer. Figure 4.13(e) and (f) show the frequency shift images $\Delta f(x,y)$ before and after the creation of the Fe pentamer which are recorded simultaneously with the tunneling current data presented in Fig. 4.13(a) and (b), respectively. Again, both $\Delta f(x,y)$ images are qualitatively and quantitatively identical. The $\Delta f(z)$ curves acquired above the center of the CO molecule (light blue and green

[1] A noticeable change could be a different Δf value at a certain conductance reference setpoint.
[2] The colorbars of both images are identical.

curve) and above the Cu(111) surface (red and black curve) overlay, respectively (see Fig. 4.13(g)). The residuals $\Delta f_{\mathrm{Cu(111),before}} - \Delta f_{\mathrm{Cu(111),after}}$ show no signature. The difference $\Delta f_{\mathrm{CO,before}} - \Delta f_{\mathrm{CO,after}}$ reveals a slight deviation of less than 0.12 Hz. However, this deviation can be attributed to a tiny difference in the (x, y) positions of the recorded spectra as the $\Delta f\,(z)$ curve on the CO molecule is highly sensitive to the exact lateral recording position. Hence, the deviation of 0.12 Hz is not significant. In summary, the above described spectra prove that the CO tip did not change

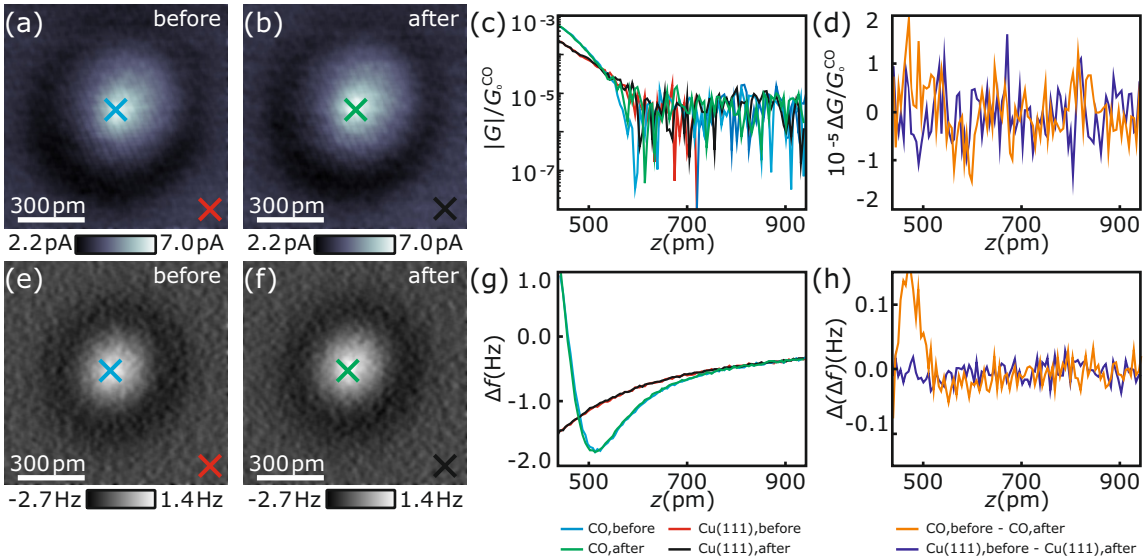

Figure 4.13. Tunneling current images $\langle I\,(x, y)\rangle$ of a single CO molecule adsorbed on the Cu(111) surface acquired in constant-height mode (a) before and (b) after the assembly of the Fe pentamer depicted in Fig. 4.12. (c) Normalized conductance spectra $G\,(z)\,/G_0^{\mathrm{CO}}$ recorded above the center of the CO molecule and above the bare Cu(111) surface as indicated by colored crosses in panels (a) and (b). (d) The normalized residuals $\Delta G/G_0^{\mathrm{CO}}$ above the center of the CO molecule $(G_{\mathrm{CO,before}} - G_{\mathrm{CO,after}})/G_0^{\mathrm{CO}}$ and above the bare Cu(111) surface $(G_{\mathrm{Cu(111),before}} - G_{\mathrm{Cu(111),after}})/G_0^{\mathrm{CO}}$ show no significant difference. (e)-(f) Corresponding simultaneously acquired frequency shift images $\Delta f\,(x, y)$ to the $\langle I\,(x, y)\rangle$ images shown in panels (a) and (b). (g) $\Delta f\,(z)$ curves acquired above the center of the CO molecule (light blue and green curve) and above the Cu(111) surface (red and black curve), respectively. The corresponding residuals $\Delta(\Delta f)$ above the bare Cu(111) surface $\Delta f_{\mathrm{Cu(111),before}} - \Delta f_{\mathrm{Cu(111),after}}$ and above the center of the CO molecule $\Delta f_{\mathrm{CO,before}} - \Delta f_{\mathrm{CO,after}}$ are depicted in panel (h). The $\langle I\,(x, y)\rangle$ and $\Delta f\,(x, y)$ images presented in panels (a), (b), (e) and (f) are slightly low pass filtered using a Gaussian filter (filter width 5 px × 5 px applied to the 256 px × 256 px raw images). The bias voltages are set to $V_{\mathrm{tip}} = -10$ mV. Figure adapted from Ref. [82].

during the assembly process of the Fe pentamer presented in Fig. 4.12. This result shows the robustness of the CO tip in case of the Fe cluster creation on Cu(111).

In the following, the five-atom Fe cluster is discussed in more detail. Khajetoorians *et al.* [20] studied the magnetic properties (e.g. switching rates and temperature dependence of the magnetic moment) of manually assembled Fe pentamers on Cu(111). Hereby, they used non-characterized metal tips. Metal tips do not reveal the internal structure of the created Fe pentamer. Accompanying DFT calculations proposed a flat (two-dimensional) or a pyramidal (three-dimensional) geometry of the Fe cluster [20].

In order to experimentally gain insight in the adsorption geometry of Fe pentamers on a quantitative basis, five different Fe pentamers are assembled atom by atom using three different CO tips. Figures 4.14(a) and (f) show the topographic $z\,(x,y)$ and the simultaneously acquired frequency shift $\Delta f\,(x,y)$ image of the Fe pentamer described in Fig. 4.12(j). The post-processed $\Delta f\,(x,y)$ image (Laplacian and Gaussian filter) shown in Fig. 4.14(k) allows precisely overlaying the hexagonal atomic lattice of the Cu(111) substrate. The fcc and hcp hollow sites[1] are indicated, respectively. As discussed above, the individual Fe atoms within a cluster appear as asymmetric tori in the $\Delta f\,(x,y)$ image. Therefore the assignment of their adsorption site is experimentally difficult. However, DFT calculations suggest a fcc hollow site adsorption for flat Fe clusters consisting of more than two Fe atoms [33]. The five green solid circles which are overlayed in Fig. 4.14(k) indicate the lateral positions of the five individual Fe atoms. The Fe pentamer is centered around a hcp hollow site. Afterwards, another Fe pentamer is created using lateral manipulation using the same CO tip. The topographic $z\,(x,y)$ and frequency shift images $\Delta f\,(x,y)$ are depicted in Figs. 4.14(b), (g) and (l). Apparently, the Fe pentamer also adsorbs in a flat geometry. In contrast to the first created Fe pentamer, the individual Fe atoms of the second five-atom cluster adsorb on hcp hollow sites centered around a top position of the Cu(111) substrate which is not the energetically most favorable adsorption according to DFT calculations [33]. However, the adsorption position of the Fe pentamer was stable on the timescale of a couple of hours and the hcp adsorption persisted even after adding five more Fe atoms in order to create a

[1]The identification of both hollow sites of the used Cu(111) sample is described in Ref. [114].

ten-atom Fe cluster (Fe decamer). A different CO tip is used to assemble a third Fe pentamer (see Figs. 4.14(c), (h) and (m)). The individual atoms of the cluster adsorb on fcc hollows sites centered around a top position (see Fig. 4.14(m)). Moreover, the individual Fe atoms of the two Fe pentamers assembled atom by atom using a third CO tip (see last two columns in Fig. 4.14) also adsorb on fcc hollow sites centered around a top and a hcp hollow site, respectively (see Fig. 4.14(n) and

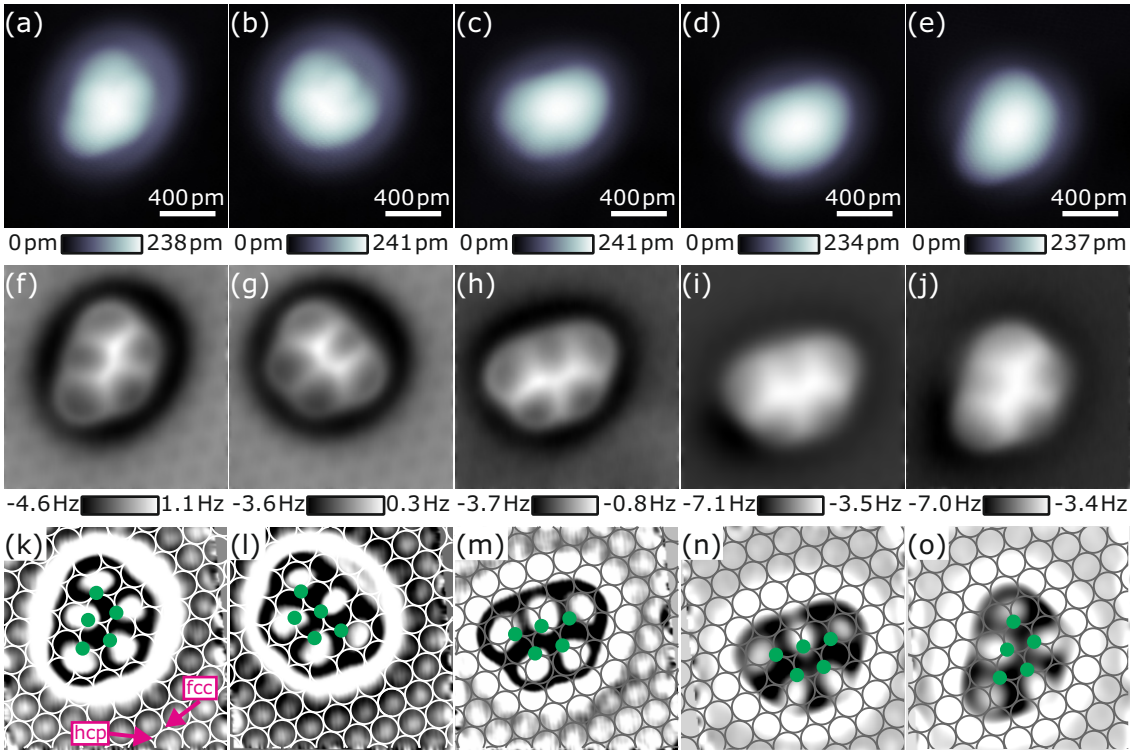

Figure 4.14. (a)-(e) Topographic images $z\,(x, y)$ of five atom-by-atom assembled Fe pentamers. (f)-(j) Corresponding simultaneously acquired frequency shift images $\Delta f\,(x, y)$ to the $z\,(x, y)$ images shown in panels (a) to (e), respectively. The $\Delta f\,(x, y)$ images are slightly low pass filtered using a Gaussian filter (filter width $8\,\text{px} \times 8\,\text{px}$). (k)-(o) Post-processed $\Delta f\,(x, y)$ images by subsequently applying a Gaussian filter (filter width $10\,\text{px} \times 10\,\text{px}$), a Laplacian filter and a Gaussian filter (filter width $10\,\text{px} \times 10\,\text{px}$) in order to enable the determination of the adsorption positions of the individual cluster atoms (see green circles). The bias voltage is set to $V_{\text{tip}} = -10\,\text{mV}$ and the individual images consist of $256\,\text{px} \times 256\,\text{px}$. The images are recorded in constant-current mode using a tunneling current setpoint of $\langle I \rangle = 300\,\text{pA}$ (panels (a), (b), (d) and (e)) and $\langle I \rangle = 400\,\text{pA}$ (panel (c)), respectively. The first two columns are acquired with the same CO tip, the central column with a second CO tip and the last two columns with a third CO tip. Figure adapted from Ref. [82].

(o)). In summary, the individual Fe atoms of four out of five presented Fe pentamers adsorb in the lowest energy fcc hollow sites, while the atoms of one five-atom Fe cluster adsorb in hcp hollow sites. Within this thesis, more small Fe clusters of various sizes were created via lateral manipulation (see also chapter 5). Out of approximately 40 Fe clusters consisting of more than 3 atoms, about 90% adsorb on fcc hollow sites, while approximately 10% adsorb on hcp hollow sites.

The apparent heights of the five assembled Fe pentamers (see Figs. 4.14(a)-(e)) are quite similar and the mean value is given by 238 ± 3 pm. The qualitative comparison of the $\Delta f\,(x, y)$ images, depicted in Figs. 4.14(f)-(j), show that the atomic contrast within the Cu(111) substrate and the Fe cluster strongly depends on the specific CO tip. In case of the first CO tip, the substrate and the Fe cluster are clearly resolved on the atomic scale in the $\Delta f\,(x, y)$ images while, in case of the second and third CO tip, extensive post-processing was required to determine the atomic structure of the substrate (see Figs. 4.14(f) and (g) versus Figs. 4.14 (h)-(j)).

As all five Fe pentamers adsorb in a flat geometry, a clear preference of the flat cluster over the three-dimensional cluster is indicated. This finding could be relevant for further investigations of the magnetic moment of small Fe clusters [20].

5. Investigation of Artificially Created Small Fe Clusters

Most of the work presented in this chapter is published in Physical Review Letters [106]. Parts of the following text are identical to the publication. The experimental measurements were performed by the author. He was supported by Fabian Stilp[1] regarding parts of the experimental data shown in section 5.5. The discussed results of accompanying DFT calculations were performed by Svitlana Polesya, Sergiy Mankovsky and Hubert Ebert from the LMU Munich within the framework of the research project No. SFB 1277, project A02.

In this chapter, atom-by-atom assembled Fe clusters are studied in more detail. At first, the terminology concerning the coordination number of individual Fe cluster atoms and the terms *physisorption* and *chemisorption* used within this chapter are introduced (section 5.1). Afterwards, the transition from physisorption to chemisorption when approaching various CO tips towards the center of a single Fe adatom are discussed by analyzing vertical short-range force versus distance curves (section 5.2). In section 5.3, small Fe clusters which are assembled atom by atom are resolved on the atomic scale and, afterwards, vertical short-range force spectra on the individual Fe atoms of the Fe cluster are investigated (subsection 5.3.1). Next, a potential influence of CO tip bending is considered (subsection 5.3.2) and short-range energy spectra on the individual Fe atoms of the Fe cluster are discussed (subsection 5.3.3). Hereafter, the origin of the atomic contrast of small Fe clusters is analyzed in detail (section 5.4) and, finally, a possible hydrogenation of small Fe clusters is studied in section 5.5.

[1]Fabian Stilp performed his bachelor thesis [114] in the group of Giessibl and was co-supervised by the author.

5.1. Terminology

5.1.1. Coordination Number and Number of Nearest Neighbors of Individual Cluster Atoms

Within this chapter, vertical short-range force curves acquired above the center of various Fe atoms are presented. These atoms are either single Fe adatoms or a part of small Fe clusters. In the following, each Fe atom is categorized by using a reduced coordination number c^*. As single Fe adatoms [98] as well as individual Fe atoms of small flat Fe clusters preferentially adsorb on fcc or hcp hollow sites[1] [33, 97, 117], c^* can be expressed by the coordination number c via:

$$c^* = c - 3 \tag{5.1}$$

Furthermore, c^* is identical to the number of neighboring Fe atoms within the xy plane of the specific Fe cluster. Table 5.1 notes all possible reduced coordination numbers c^* of the investigated Fe atoms as a function of cluster size and cluster name.

name	adatom	trimer	tetramer	pentamer	hexamer	decamer	tri-decamer	penta-decamer
size	1	3	4	5	6	10	13	15
c^*	0	2	2, 3	2, 3, 4	2, 4	2, 4, 6	2, 5, 6	2, 3, 4, 6

Table 5.1. Reduced coordination number c^* (i.e. number of nearest neighbors in plane) as a function of Fe cluster size (total number of Fe atoms within cluster).

Figures 5.1(a)-(e) depict the frequency shift images $\Delta f(x, y)$ of an atom-by-atom assembled Fe trimer, Fe tetramer, Fe pentamer, Fe decamer and Fe tridecamer, respectively, recorded in constant-current mode. The $\Delta f(x, y)$ images were recorded with a CO tip. The individual atoms of each Fe cluster and the Cu(111) substrate are resolved on the atomic scale. The Fe atoms are categorized by the reduced coordination number c^* (see colored circles in Figs. 5.1(f)-(j)).

In the following, all vertical short-range force $F_{z,\mathrm{SR}}$ and energy E_{SR} versus distance

[1] This holds true for all sizes of Fe clusters except for two-atom Fe clusters.

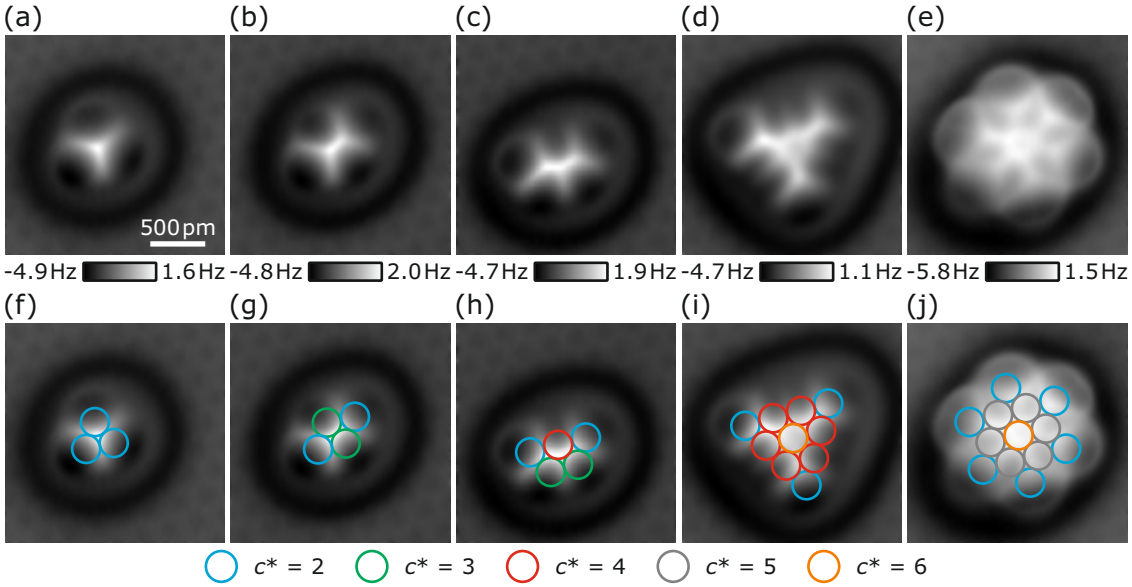

Figure 5.1. (a)-(e) Frequency shift images $\Delta f\,(x, y)$ of an atom-by-atom assembled three-, four-, five-, ten- and thirteen-atom Fe cluster acquired in constant-current mode using a CO tip. (f)-(j) Same images as depicted in panels (a)-(e) with overlayed colored circles (diameter 255 pm). The color of the circles indicates the atom's reduced coordination number c^*, i.e. number of nearest-neighbor Fe atoms. All $\Delta f\,(x, y)$ images were slightly smoothed using a Gaussian filter (filter width 6 px × 6 px applied to the 256 px × 256 px raw images). Imaging parameters: (a)-(e) $V_{\text{tip}} = -1$ mV, (a)-(d) $\langle I \rangle = 80$ pA and (e) $\langle I \rangle = 100$ pA, respectively. Figure adapted from Ref. [106].

z curves acquired above the center of individual Fe atoms[1] are expressed as a function of distance z and reduced coordination number c^* ($F_{z,\text{SR}}\,(z, c^*)$ and $E_{\text{SR}}\,(z, c^*)$).

5.1.2. Physisorption and Chemisorption

In surface physics and surface chemistry, physisorption describes the adsorption of an isolated atom or molecule on a surface due to attractive van-der-Waals interactions (see also subsection 2.2.2). Hereby, the electronic orbitals of the interaction partners do not change significantly [118, 119]. Chemisorption defines the adsorption of an isolated atom or molecule on an adsorbent as a result of the formation of a chemical bond between the adsorbate and the adsorbent involving a significant change of the electronic orbitals such as a hybridization of electronic orbitals [119, 120] (see also

[1] Each z spectroscopy curve is acquired either above single Fe adatoms or above Fe atoms incorporated in flat Fe clusters.

subsection 2.2.2).

Within this chapter, different CO tips are positioned, in experiment and DFT calculations, at various (x, y, z) positions above an adsorbent (e.g. a Fe adatom or a Fe cluster). As DFT only considers the single CO molecule as a tip (see Fig. 5.2(a)), there is a one-to-one correspondence to the physisorption or chemisorption of an isolated molecule, i.e. the CO molecule, on an adsorbent, i.e. a Fe atom. In the experiments, the CO molecule cannot be positioned freely at any (x, y, z) position without fixing it at one side. Therefore, the single CO molecule is transferred to the monoatomic metal tip of a qPlus sensor where it chemically binds to the frontmost tip atom with its C atom [31] (see Fig. 5.2(b)). Hence, the experimental signal resembles the total interaction between the complete tip and the adsorbent, i.e. the Fe adatom or Fe cluster. However, as short-range interactions are dominant at short-distances, the main contribution to the recorded forces originates from the interaction of the tip's CO molecule (i.e. the adsorbate) with the Fe adatom or Fe cluster (i.e. the adsorbent) at close distances. Therefore, the terms physisorption and chemisorption are used in the following for the experimental recorded data as well, although the CO molecule is already adsorbed on its C atom side to the metal tip's front atom.

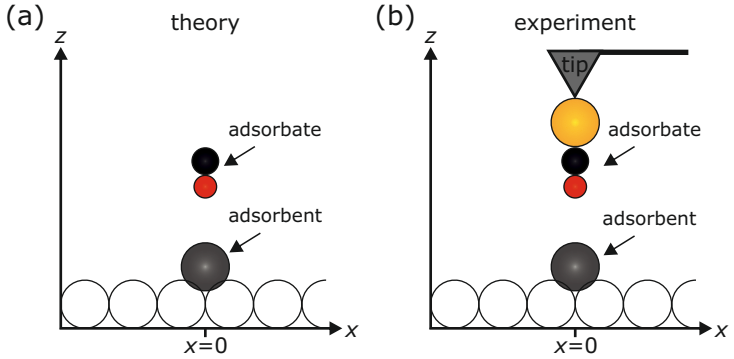

Figure 5.2. (a) Sketched theoretical setup in side view. In case of the DFT calculations, a single, rigid CO molecule (adsorbate) is used as a tip which can be positioned at various positions (x, y, z) above a single Fe adatom or a Fe atom inside a Fe cluster (adsorbent). (b) Sketch (side view) of the experimental setup showing a CO molecule attached to a monoatomic metal tip above a single Fe adatom adsorbed on the Cu(111) surface. The interaction between the tip and the substrate (unfilled circles) is subtracted in both theory and experiment (see also section 2.3.3). The cantilever and its tip are not sketched to scale.

5.2. Building Block of Fe Clusters: Single Fe Adatom

5.2.1. Origin of the Torus Appearance of Single Fe Adatoms

As mentioned in chapter 4, a single Fe adatom adsorbed on the Cu(111) surface appears as a torus in AFM imaged in constant-height mode with a CO tip. Additionally, the torus shows three local maxima (see Fig. 5.3(a)) which point to the neighboring hcp hollow sites [33]. In the following, the reason for the appearance of the single Fe adatom as a torus is discussed[1]. The orange colored short-range force versus distance curve $F_{z,\mathrm{SR}}(z)$ depicted in Fig. 5.3(b) is recorded at a (x, y) position of the torus appearance. The (x, y) location is marked with an orange cross in Fig. 5.3(a). The $F_{z,\mathrm{SR}}(z)$ curve shows a shallow minimum of $-3\,\mathrm{pN}$ at $z_{\mathrm{phys}} = 365\,\mathrm{pm}$. At closer tip-sample distances, the force is turning repulsive. The repulsion stems

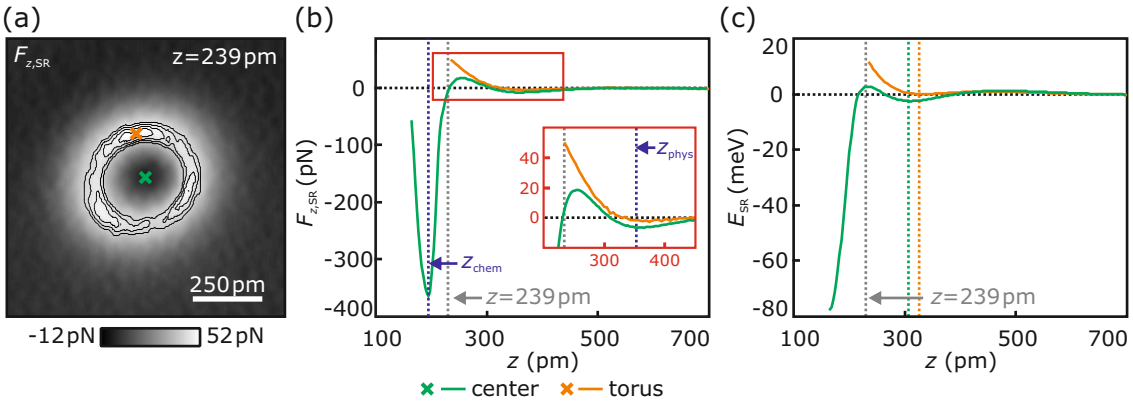

Figure 5.3. (a) $F_{z,\mathrm{SR}}(x, y, z = 239\,\mathrm{pm})$ image ($V_{\mathrm{tip}} = -0.1\,\mathrm{mV}$, $256\,\mathrm{px} \times 256\,\mathrm{px}$) of a single Fe adatom adsorbed on Cu(111) recorded in constant-height mode using a CO tip. The contour lines are spaced by 3 pN in a range from 40 pN to 52 pN. Note that the high-symmetry direction of the substrate is rotated by 15° anti-clockwise with respect to the horizontal axis. (b) The short-range force versus distance curve $F_{z,\mathrm{SR}}(z)$ acquired above the torus (orange curve) possesses a shallow dip at $z = z_{\mathrm{phys}}$. At smaller z distances it is turning repulsive. The $F_{z,\mathrm{SR}}(z, c^* = 0)$ curve recorded above the center of the Fe adatom (green curve) also shows a first shallow minimum at $z = z_{\mathrm{phys}}$ and, after exhibiting a repulsive barrier, a second deeper minimum at $z = z_{\mathrm{chem}}$. The corresponding short-range energy versus distance curves $E_{\mathrm{SR}}(z)$ are depicted in panel (c). The green colored $F_{z,\mathrm{SR}}(z)$ and $E_{\mathrm{SR}}(z)$ curves of panels (b) and (a) are also shown in Ref. [42].

[1]The original explanation of the torus appearance of the single Fe adatom including all relevant DFT calculations is presented in Ref. [42].

from Pauli repulsion on the CO tip due to an increased overlap of the electron charge densities of CO tip and Fe adatom. The corresponding short-range energy versus distance curve $E_{\mathrm{SR}}(z)$ is depicted in Fig. 5.3(c). It shows a local minimum of 0.2 meV at the z position indicated by the vertical orange dotted line. The presence of a positive minimum can be attributed to the long-range electrostatic repulsive interaction between the positively charged Fe adatom[1] and the in-total positively charged CO tip [38, 39]. The short-range force $F_{z,\mathrm{SR}}(z)$ and energy curves $E_{\mathrm{SR}}(z)$ resemble, due to the shallow minima, a typical physisorption-like force and energy curve.

The green colored $F_{z,\mathrm{SR}}(z, c^* = 0)$ curve with the corresponding $E_{\mathrm{SR}}(z, c^* = 0)$ curve (see Fig. 5.3(b) and (c)) are acquired above the center of the Fe adatom (as indicated by the green colored cross in Fig. 5.3(a)). At $z = z_{\mathrm{phys}}$, $F_{z,\mathrm{SR}}(z, 0)$ also shows a shallow minimum (−8 pN) which is slightly more attractive compared to the minimum of the orange curve. After passing a distance regime of repulsion, another more attractive force minimum of −364 pN appears at $z_{\mathrm{chem}} = 194$ pm. The corresponding $E_{\mathrm{SR}}(z, 0)$ curve exhibits a maximum of 2.9 meV between the shallow energy minimum of −2.3 meV at the z position indicated by the vertical green dotted line and the second minimum at closer z distances which is not resolved, yet. It was found that the first minimum of the $F_{z,\mathrm{SR}}(z, 0)$ curve at $z = z_{\mathrm{phys}}$, recorded in the center of the Fe adatom, corresponds to the physisorption force minimum [42]. Here, pure physical attraction between the tip's CO molecule and the Fe adatom occurs. Upon further approaching the CO tip towards the Fe adatom's center, the electronic orbitals of the CO molecule and the Fe adatom hybridize leading to a formation of a chemical bond. The chemical bond formation leads to additional attraction between the Fe adatom and the CO tip at closer z distances [42]. The vertical position of strongest attraction is indicated by z_{chem}. The CO tip, therefore, transitions from a physisorbed to a chemisorbed state when approaching the center of the Fe adatom. During the transition, the CO tip overcomes a potential barrier of 5.2 meV. The hybridization of the electronic orbitals is maximal if the CO tip is positioned above the center of the Fe adatom. A lateral shift of the CO tip with respect to the Fe adatom's center results in a decrease of the overlap of the electronic orbitals and, therefore, in a decrease of the hybridization [42].

[1] The positive charge of the Fe adatom is a result of the Smoluchowski effect [111] (see also chapter 4).

This leads, consequently, to a less attractive force at the same z position. If the CO tip is laterally offset by about 200 pm with respect to the Fe adatom's center, hybridization does not occur anymore and, hence, the vertical short-range force is dominated by Pauli repulsion (as shown by the orange colored spectrum in Fig. 5.3(b)). The $F_{z,\mathrm{SR}}(x, y)$ image depicted in Fig. 5.3(a) is acquired at a tip-sample distance of $z = 239$ pm. At this z distance, the tip's CO molecule transitions from physisorption to chemisorption when centered above the Fe adatom and, therefore, the CO tip is slightly attracted to the Fe adatom. However, 200 pm off center, repulsive forces resulting from Pauli repulsion dominate. Hence, the Fe adatom appears as a torus in the $F_{z,\mathrm{SR}}(x, y, z = 239\,\mathrm{pm})$ image shown in Fig. 5.3(a) [42].

5.2.2. Short-Range Force Spectroscopy above the Fe Adatom's Center Using Different CO Tips

Section 4.3 shows that two different CO tips lead to qualitatively different short-range potentials and lateral forces when interacting with a single Fe adatom. In the following, the influence of different CO tips is studied in detail by comparing short-range force versus distance curves $F_{z,\mathrm{SR}}(z, 0)$ acquired above the center of a single Fe adatom with five different CO tips (see Fig. 5.4(a) and Fig. 5.4(b) for the corresponding $E_{\mathrm{SR}}(z, 0)$ curves). The chemisorption energy minima (i.e. the energy minima at smaller z distances) are not resolved in the $E_{\mathrm{SR}}(z, 0)$ curves. In order to determine the chemisorption energy minimum, each CO tip needs to approach the center of the Fe adatom further. However, a noticeable change in the drive signal of the qPlus sensor is detected when further reducing the tip-sample distance. Therefore, dissipative forces between CO tip and Fe adatom occur which typically indicates that the tip structure will change if the tip-sample distance is further reduced. However, the chemisorption force minima (i.e. the force minima at smaller z distances) are fully resolved. As the value of the energy minimum directly correlates with the value of the force minimum, the chemisorption force minimum is discussed in the remainder to evaluate the strength of the chemical bond between CO tip and Fe adatom. Here, the green colored $F_{z,\mathrm{SR}}(z, 0)$ curve (CO tip 1, see Fig. 5.4(a)) is identical to the $F_{z,\mathrm{SR}}(z, 0)$ curve depicted in Fig. 5.3(b). While the physisorption force minima (i.e. the force minima at larger z positions) of CO tips 3, 4 and 5 are quite similar in absolute value, they are more attractive

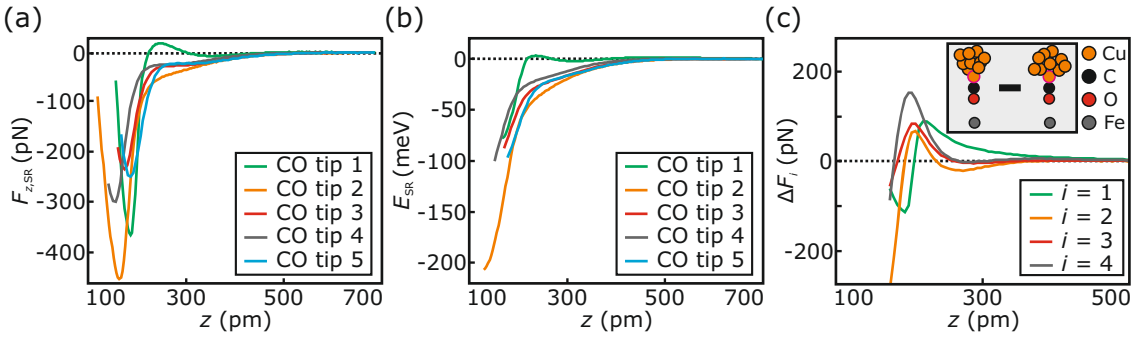

Figure 5.4. (a) Short-range vertical force versus distance curves $F_{z,\mathrm{SR}}(z,0)$ recorded above the center of a single Fe adatom using five different CO tips (CO tips 1 to 5). (b) Corresponding short-range energy versus distance curves $E_{\mathrm{SR}}(z,0)$. (c) Force difference curves $\Delta F_i = F_{z,\mathrm{SR}}(z,0)|_{\mathrm{COtip}\ i} - F_{z,\mathrm{SR}}(z,0)|_{\mathrm{COtip}\ 5}$ for $i = 1,2,3,4$ (as indicated by the sketch in the inset). All CO tips consist of a CO molecule adsorbed to a monoatomic metal tip. However, the metal backgrounds of the various tips differ. The experimental data shown in this figure is also presented in Ref. [106].

compared to the physisorption force minimum of CO tip 1. In case of CO tip 2, the physisorption force minimum is represented by a linear slope around $z \approx 300\,\mathrm{pm}$. The chemisorption force minimum (i.e. the minimum at smaller z distance) of CO tip 2 is more attractive compared to CO tip 1 while the chemisorption force minima of CO tips 3,4 and 5 are less attractive compared to CO tip 1. Overall, a proportional relation between physisorption force minimum value and chemisorption force minimum value is not observed.

All CO tips consist of a single CO molecule adsorbed to the apex of a monoatomic metal tip. Hence, the atomic species and the arrangement of the three foremost atoms (i.e. the O, C and Cu atom) of the tips are identical. However, the metal backgrounds behind these three atoms differ as the tips were poked repeatedly into the bare Cu(111) surface in order to generate a monoatomic tip prior to the CO functionalization (see also section 3.4). If the differences in the metal backgrounds of the different CO tips would lead to a plain additive contribution in the interaction between tip and Fe adatom, the force differences $\Delta F_i = F_{z,\mathrm{SR}}(z,0)|_{\mathrm{COtip}\ i} - F_{z,\mathrm{SR}}(z,0)|_{\mathrm{COtip}\ 5}$ with $i = 1,2,3,4$ should resemble a simple Lennard-Jones type behavior [112] (i.e. a single attractive dip at intermediate distances z and repulsion for short distances z). However, the differential force curves ΔF_i do not resemble

a Lennard-Jones type behavior[1] (see Fig. 5.4(c)). Hence, the contribution of the differences in the metal tip backgrounds of CO tip 1 to 5 cannot be treated in an additive manner. Therefore, the interaction (i.e. the chemical bond) between the individual CO molecules and the metal tips must be different. The differences of the chemical bond between CO molecules and metal tips lead to the quantitatively different $F_{z,\mathrm{SR}}(z,0)$ curves shown in Fig. 5.4(a). This observation agrees with the finding that the properties of CO tips strongly depend on the exact shape of the metal tip's structure behind the terminating CO molecule as discussed in Refs. [38, 39].

In summary, all $F_{z,\mathrm{SR}}(z,0)$ spectra acquired with five different CO tips show the transition from physisorption to chemisorption while the exact shape of the curves differ due to different chemical bonds between the various CO molecules and their metal tip backgrounds.

5.2.3. Potential Influence of CO Tip Bending on the Short-Range Force Spectra Acquired above Single Fe Adatoms

Repulsive interactions (e.g. Pauli repulsion) between the CO tip and an adsorbate or a surface can lead to a lateral deflection of the CO molecule on the tip. A lateral deflection of the tip's CO can introduce imaging artifacts such as bond elongation when imaging organic molecules [121] or the appearance of repulsive areas that can be misinterpreted as bonds [122]. Moreover, the lateral flexibility of CO tips can lead to the appearance of a second minimum in frequency shift $\Delta f(z)$ or vertical force $F_z(z)$ versus distance z curves if experiencing lateral repulsive interactions [123, 124].

In principle, CO bending could also be responsible for the appearance of the two minima in the $F_{z,\mathrm{SR}}(z,0)$ curves recorded above the center of a single Fe adatom (see Fig. 5.3(b)). However, the lateral force above the attractive center of the Fe adatom is zero and even a slight lateral offset with respect to the center would lead to a lateral deflection of the CO molecule towards the center of the Fe adatom [42].

[1] This observation does not change qualitatively when introducing a z offset in a range of $-20\,\mathrm{pm}$ to $20\,\mathrm{pm}$ to the z axes of the individual $F_{z,\mathrm{SR}}(z,0)$ spectra or subtracting a different $F_{z,\mathrm{SR}}(z,0)$ curve of CO tip 1, 2, 3 or 4.

Moreover, the double minima shape of the $F_{z,\mathrm{SR}}(z,0)$ spectra are reproduced by DFT calculations using a rigid CO molecule as a tip model [42]. Hence, the double minima of the $F_{z,\mathrm{SR}}(z,0)$ curves in case of the single Fe adatom are not caused by CO bending and the tip's CO molecule remains upright during the acquisition of the $F_{z,\mathrm{SR}}(z,0)$ spectra [42].

5.3. Fe Clusters Consisting of 3 to 15 Atoms

5.3.1. Force Spectroscopy on Individual Fe Cluster Atoms

Small Fe cluster are assembled atom-by-atom using three different CO tips (CO tips 2 to 4). Figure 5.5(a) depicts the $\Delta f(x,y)$ image of a ten-atom Fe cluster recorded in constant-current mode which is created and imaged using CO tip 2. The individual atoms of the Fe cluster adsorb on fcc hollow sites[1]. DFT calculations[2] confirm the fcc adsorption geometry while the corner (edge) atoms laterally deviate by 11 pm (6 pm) from the ideal fcc hollow position towards the central atom of the cluster [83, 106]. The atomic positions calculated by DFT[3] are overlayed as colored circles on the $\Delta f(x,y)$ image (see Fig. 5.5(b)). The color of the circles indicates the reduced coordination number c^* of each Fe atom. The c^* value of the cluster's central atom is $c^* = 6$. The six neighboring Fe atoms of the central atoms exhibit a value of $c^* = 4$ and the three corner atoms possess a value of $c^* = 2$ (see also subsection 5.1.1). Figure 5.5(c) shows three different experimental $F_{z,\mathrm{SR}}(z,c^*)$ spectra recorded above the three different types of Fe atoms within the cluster. The three different types differ by the reduced coordination number c^*. The force spectra $F_{z,\mathrm{SR}}(z,2)$ and $F_{z,\mathrm{SR}}(z,4)$ are acquired slightly off-center the specific Fe atom to ensure that the CO tip remains upright during the acquisition of the force curves (see subsection 5.3.2 for further details). The experimental $F_{z,\mathrm{SR}}(z,2)$ curve exhibits a shoulder-like dip at $z \approx 280\,\mathrm{pm}$ and a global force minimum of $F_{z,\mathrm{SR}}(z_{\mathrm{chem}},2) = -204\,\mathrm{pN}$ at $z_{\mathrm{chem}} = 168\,\mathrm{pm}$. The $F_{z,\mathrm{SR}}(z,4)$ curve recorded above an edge Fe atom displays a global physisorption force minimum (i.e. the minimum at larger z distance) of

[1] Not shown here.
[2] All DFT calculations include van-der-Waals interactions (DFT-D3). The computational details can be found in Ref. [106].
[3] The calculated adsorption positions are aligned with the experimental image via the central atom as it appears circularly symmetric in the $\Delta f(x,y)$ image.

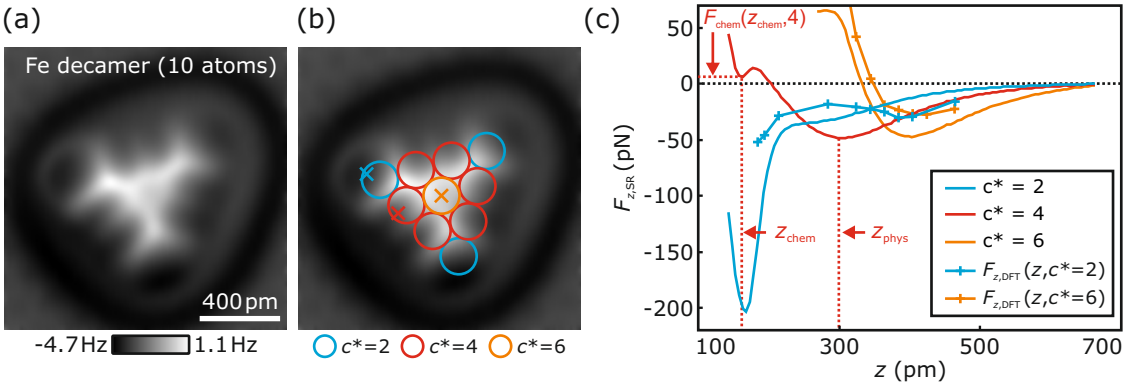

Figure 5.5. (a) Atomically resolved frequency shift image $\Delta f(x, y)$ of an atom-by-atom assembled ten-atom Fe cluster (Fe decamer) acquired in constant-current mode using CO tip 2. The high-symmetry direction of the substrate is rotated by 15° anti-clockwise with respect to the horizontal axis. (b) Same image as shown in panel (a) but overlayed with the atomic positions of the individual cluster's atoms (colored circles). The atomic positions are color-coded with respect to the reduced coordination number c^*. (c) Experimental $F_{z,\mathrm{SR}}(z, c^*)$ and theoretical $F_{z,\mathrm{DFT}}(z, c^*)$ vertical short-range force versus distance curves above the central, edge and corner atom of the Fe decamer whose (x, y) positions are indicated by colored crosses in panel (b). The corresponding experimental energy versus distance spectra $E_{\mathrm{SR}}(z, c^*)$ are shown in Fig. 5.6. Experimental parameters: (a) $V_{\mathrm{tip}} = -1\,\mathrm{mV}$, $\langle I \rangle = 80\,\mathrm{pA}$ and (c) $V_{\mathrm{tip}} = 0$. Figure adapted from Ref. [106].

$F_{z,\mathrm{SR}}(z_{\mathrm{phys}}, 4) = -48\,\mathrm{pN}$ at $z_{\mathrm{phys}} = 298\,\mathrm{pm}$ and a chemisorption force minimum (i.e. the minimum at smaller z distance) of $F_{z,\mathrm{SR}}(z_{\mathrm{chem}}, 4) = 6\,\mathrm{pN}$ at a smaller tip-sample distance $z_{\mathrm{chem}} = 163\,\mathrm{pm}$. The orange colored curve ($c^* = 6$) exhibits a global force minimum of $F_{z,\mathrm{SR}}(z_{\mathrm{phys}} = 403\,\mathrm{pm}, 6) = -47\,\mathrm{pN}$ and a chemisorption force plateau[1] of $F_{z,\mathrm{SR}}(z_{\mathrm{chem}} = 278\,\mathrm{pm}, 6) = 65\,\mathrm{pN}$.

In conclusion, all three experimental force curves deviate from a simple Lennard-Jones-type distance dependence. In case of the $F_{z,\mathrm{SR}}(z, 2)$ curve, a shoulder-like plateau and a global minimum is visible. For the $F_{z,\mathrm{SR}}(z, 4)$ and $F_{z,\mathrm{SR}}(z, 6)$ curves, two distinct minima are observed, respectively. In the following, the minima at larger (smaller) tip-sample distances z are interpreted as the physisorption (chemisorption) force minima, similar to the single Fe adatom. As the chemisorption force minima are present, the CO tip transitions from physisorption to chemisorption when

[1] It is unknown whether the $F_{z,\mathrm{SR}}(z, 6)$ curve displays a second force minimum at smaller tip-sample distances z, as z cannot be reduced further due to a significant change in the drive signal of the qPlus sensor.

approaching individual Fe atoms of the Fe decamer. In case of the edge and central atoms ($c^* = 4, 6$), the chemisorption force minimum is positive and, therefore, a stable chemical bond between the tip's CO molecule and the central Fe atom is not formed.

The $F_{z,\mathrm{DFT}}(z, 2)$ force curve, calculated by DFT, also shows a local minimum at larger z distance ($F_{z,\mathrm{DFT}}(384\,\mathrm{pm}, 2) = -29.9\,\mathrm{pN}$) and the beginning of a second global minimum at smaller z distance[1]. Therefore, it qualitatively agrees with the experimental $F_{z,\mathrm{SR}}(z, 2)$ curve. However, the physisorption force minimum in the calculated $F_{z,\mathrm{DFT}}(z, 2)$ curve occurs at a larger z distance compared to the shoulder-like section of the experimental $F_{z,\mathrm{SR}}(z, 2)$ curve (384 pm versus 280 pm). This discrepancy can be a result of the simplified tip model[2] used in the DFT calculations compared to the experimental tip. In case of the central atom ($c^* = 6$), the agreement of the position (424 pm versus 403 pm) and the magnitude (-27.1 pN versus -47 pN) of the physisorption force minimum between the calculated and experimental force curves is enhanced, respectively. Additionally, the calculated force curve ($c^* = 6$) reproduces the repulsion at smaller tip-sample distances z. The calculation of the force curve above a Fe atom of the cluster's edge ($c^* = 4$) is in progress at the time of this thesis's submission.

In summary, all experimental force curves show a deviation from a simple Lennard-Jones type behavior, i.e. a single minimum at intermediate distances and repulsion at small distances. This is interpreted as a transition of CO tip 2 from physi- to chemisorption when approaching the individual Fe atoms of the ten-atom Fe cluster, similar as for the single Fe adatom. Hereby, a strong dependence of the chemisorption force value $F_{z,\mathrm{SR}}(z_{\mathrm{chem}}, c^*)$ on the reduced coordination number c^* is indicated.

Figure 5.6 shows the $E_{\mathrm{SR}}(z, c^*)$ curves corresponding to the $F_{z,\mathrm{SR}}(z, c^*)$ spectra depicted in Fig. 5.5(c). The light blue colored curve acquired above a corner atom ($c^* = 2$) shows a linear slope in the z regime indicated by the light blue arrow.

[1] The calculation of further data points at closer z positions is in progress at the time of this thesis's submission. Note that the DFT calculations for magnetic systems are very time-consuming.

[2] As discussed above, in DFT, a single CO molecule without a metal tip background is used as a tip while, in the experiments, the tip consists of a CO molecule which terminates a monoatomic metal tip.

The linear slope is a result of the competition of van-der-Waals interaction and Pauli repulsion at intermediate distances and the entering of hybridization of the electronic orbitals of the CO tip and Fe corner atom. The linear slope leads to the shoulder-like feature in the corresponding $F_{z,\mathrm{SR}}(z, 2)$ curve (see Fig. 5.5(c)). The chemisorption energy minimum is not resolved, yet, similar as in the case of the single Fe adatom (see Fig. 5.4(b)). The $E_{\mathrm{SR}}(z, 4)$ spectrum acquired above the edge atom of the Fe decamer shows two distinct minima (indicated by the red arrows). The minimum at larger z distance is interpreted as the physisorption energy minimum while the second minimum at smaller z distance corresponds to the chemisorption energy minimum, i.e. the distance where the electronic orbitals of the CO tip and the Fe atom hybridized. In case of the central Fe atom ($c^* = 6$), the physisorption energy minimum indicated by the orange arrow at larger z distance is clearly resolved. The chemisorption energy minimum is not visible. However, the $E_{\mathrm{SR}}(z, 6)$ curve exhibits a linear slope at the z range indicated by the orange arrow at smaller z distances. This linear regime corresponds to the repulsive plateau in the $F_{z,\mathrm{SR}}(z, 6)$ curve depicted in Fig. 5.5(c). As the $F_{z,\mathrm{SR}}(z_{\mathrm{chem}}, 6)$ value is repulsive and the corresponding energy versus distance curve exhibits a linear relation in the

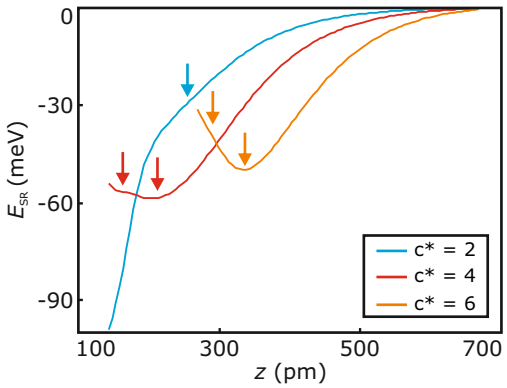

Figure 5.6. Corresponding short-range energy versus distance curves $E_{\mathrm{SR}}(z, c^*)$ to the $F_{z,\mathrm{SR}}(z, c^*)$ spectra depicted in Fig. 5.5(c). The colored arrows indicate either features, minima or linear slopes which correspond to the physisorption and chemisorption force minima of the $F_{z,\mathrm{SR}}(z, c^*)$ curves shown in Fig. 5.5(c). In case of $c^* = 2$, the energetic chemisorption minimum is not resolved in the experiment (see text). The experimental data shown in this figure is also presented in Ref. [106].

corresponding distance z regime, stable[1] chemical bonding between CO tip and the central Fe atom of the ten-atom Fe cluster does not occur. However, the presence of the linear slope is a distinct signature of an additional interaction between CO tip and the central Fe atom, presumably resulting from a weak hybridization between the electronic orbitals of CO tip and the central Fe atom.

In conclusion, all $E_{\mathrm{SR}}(z, c^*)$ curves are entirely attractive and show, next to the physisorption energy minimum, a second minimum or feature which indicates that a transition from physi- to chemisorption occurs. However, in case of the edge ($c^* = 4$) and central ($c^* = 6$) Fe atoms of the Fe decamer, the chemisorption energy minima are not energetically lower than the physisorption energy minima and do not lead to a stable chemical bond. In case of the corner atom ($c^* = 2$), the chemisorption energy minima could not be resolved yet, as a significant change in the qPlus sensor's drive signal is detected prohibiting the further reduction of the tip-sample distance z. However, the chemisorption energy minimum leads to a stable chemical bond as it is more attractive than the shoulder-like physisorption energy feature.

In the following, the chemisorption strength is investigated by studying the chemisorption force values $F_{z,\mathrm{SR}}(z_{\mathrm{chem}}, c^*)$ as a function of the reduced coordination number c^* because the chemisorption energy minima are not resolved in each of the energy versus distance curves[2] $E_{\mathrm{SR}}(z, c^*)$. Hereafter, various $F_{z,\mathrm{SR}}(z, c^*)$ spectra recorded with three different CO tips (CO tips 2, 3 and 4) on several atom-by-atom assembled Fe clusters are analyzed (see Fig. 5.7). The corresponding atomically-resolved $\Delta f(x, y)$ images of the Fe clusters are shown in Fig. A.2 of the appendix. First, a clustering of the chemisorption force minima $F_{z,\mathrm{SR}}(z_{\mathrm{chem}}, c^*)$ with respect to the reduced coordination number c^* is observed for all CO tips. While the chemisorption force minima for CO tip 2 are clearly resolved for all reduced coordination numbers $c^* = 0, 2, 3, 4, 6$ (Fig. 5.7(a)), they are only visible for CO tip 3 and 4 for $c^* = 0, 2, 3, 6$ (Fig. 5.7(b) and (c)). For $c^* = 4, 5$, the $F_{z,\mathrm{SR}}(z, c^*)$ curves exhibit a linear relation in a z range between 140 pm and 200 pm (Fig. 5.7(b) and (c)) leading to a plateau in the short-range force gradient curves[3]

[1] If the CO tip were not fixed at one end to the qPlus sensor, the distance between CO tip and Fe atom would increase until the short-range potential between tip and sample is minimized.
[2] This restriction is similar to the case of the single Fe adatom in section 5.2.
[3] The short-range force gradient curves are not shown here.

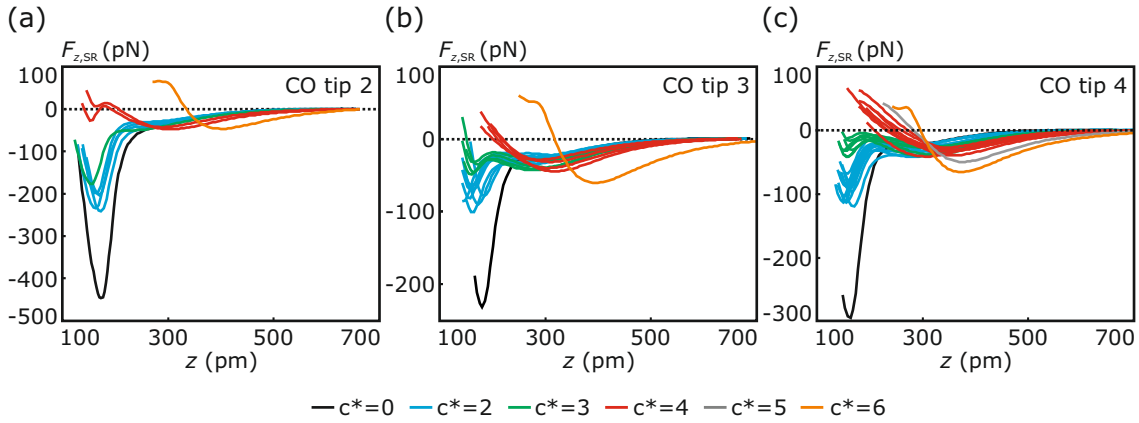

Figure 5.7. (a)-(c) Experimental vertical short-range force versus distance curves $F_{z,\mathrm{SR}}(z, c^*)$ above single Fe adatoms and individual Fe atoms of various atom-by-atom assembled Fe clusters using CO tips 2 to 4, respectively (see Fig. A.2 of the appendix for the corresponding atomically resolved $\Delta f(x, y)$ images of all atom-by-atom assembled Fe clusters). Figure adapted from Ref. [106].

$k_{z,\mathrm{SR}}(z, c^*) = -\partial F_{z,\mathrm{SR}}(z, c^*)/\partial z$. Hence, these linear relations in the $F_{z,\mathrm{SR}}(z, c^*)$ curves for $c^* = 4, 5$ indicate the onset of an additional interaction between the CO tip and the cluster's individual Fe atom presumably stemming from a weak hybridization of the electronic orbitals of CO tip and the investigated Fe atom[1]. As discussed in section 5.2, the chemisorption force minima between the single Fe adatom and CO tips 2, 3 and 4 differ significantly (-448 pN, -231 pN and -296 pN). This observation is attributed to a different chemical binding of the tip's single CO molecules on the various metal tip backgrounds (see subsection 5.2.2). The mean value of the chemisorption force minima between the corner Fe atoms ($c^* = 2$) and CO tip 2, 3 and 4 also differ (-215 ± 22 pN, -80 ± 13 pN and -98 ± 16 pN). The variation of the mean value of $F_{z,\mathrm{SR}}(z_{\mathrm{chem}}, 2)$ with respect to the CO tip number correlates with the chemisorption force minima of the different CO tips above the single Fe adatom: Using CO tip 2, the $F_{z,\mathrm{SR}}(z_{\mathrm{chem}}, 0)$ value is more negative compared to the $F_{z,\mathrm{SR}}(z_{\mathrm{chem}}, 0)$ values of CO tip 3 and 4. Also the $F_{z,\mathrm{SR}}(z_{\mathrm{chem}}, 2)$ value is more negative compared to the $F_{z,\mathrm{SR}}(z_{\mathrm{chem}}, 2)$ values of CO tip 3 and 4. The same holds true when comparing the chemisorption force minima in case of $c^* = 3$ (-178 pN, -41 ± 8 pN and -30 ± 11 pN) and $c^* = 6$ (28 pN, 50 pN

[1]Without the onset of chemical bond formation, the slope of the $F_{z,\mathrm{SR}}(z, c^*)$ curve would continuously increase with decreasing tip-sample distance after passing the physisorption force minimum.

and 34 pN) with the chemisorption force minima of the single Fe adatom of CO tip 2, 3 and 4. As discussed above, a comparison of the chemisorption force minima of the different CO tips in case of $c^* = 4$ is not possible as they are not clearly resolved with CO tip 3 and 4.

In summary, a correlation of the chemisorption force minimum $F_{z,\mathrm{SR}}(z_{\mathrm{chem}}, c^*)$ and the reduced coordination number c^* is deduced: The $F_{z,\mathrm{SR}}(z_{\mathrm{chem}}, c^*)$ values correlate with the chemisorption force minima $F_{z,\mathrm{SR}}(z_{\mathrm{chem}}, 0)$ of the single Fe adatom when using different CO tips. This trend becomes more clear when plotting the values of the chemisorption force minima $F_{z,\mathrm{SR}}(z_{\mathrm{chem}}, c^*)$ against the reduced coordination number c^* (see Fig. 5.8). Hereby, the error bars indicate the standard deviations of the mean values of the chemisorption force minima $F_{z,\mathrm{SR}}(z_{\mathrm{chem}}, c^*)$ for all three CO tips. The corresponding trend lines of all CO tips show the same behavior, namely a decrease of attraction with increasing reduced coordination number c^*. A correlation between the $F_{z,\mathrm{SR}}(z_{\mathrm{chem}}, c^*)$ value and the cluster size is not found. In the following, the dependence of $F_{z,\mathrm{SR}}(z_{\mathrm{chem}}, c^*)$ on the reduced coordination number c^* is interpreted as a direct measurement of the chemical reactivity, i.e. the *active sites* [30] of individual Fe atoms incorporated in small Fe clusters. However, the black curve (CO tip 2) is significantly more attractive compared to the golden (CO tip 3) and gray (CO tip 4) curves. As discussed above, this occurs due to the different

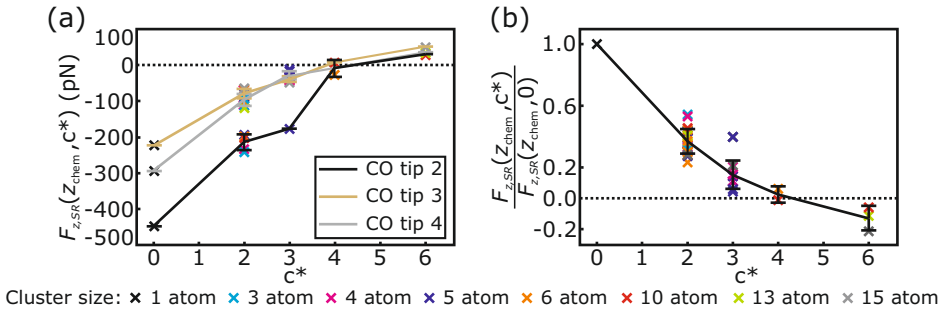

Figure 5.8. (a) Chemisorption force minima $F_{z,\mathrm{SR}}(z_{\mathrm{chem}}, c^*)$ versus reduced coordination number c^* extracted from the $F_{z,\mathrm{SR}}(z, c^*)$ curves depicted in Fig. 5.7. (b) Same plot as shown in panel (a) while the chemisorption force minima $F_{z,\mathrm{SR}}(z_{\mathrm{chem}}, c^*)$ are normalized with the corresponding chemisorption minima of the single Fe adatom $F_{z,\mathrm{SR}}(z_{\mathrm{chem}}, 0)$ curve. The error bars indicate the standard deviation of the mean value of the chemisorption force minima $F_{z,\mathrm{SR}}(z_{\mathrm{chem}}, c^*)$ of (a) CO tip 2,3 and 4 and (b) of all CO tips with respect to c^*, respectively. Panel (b) is adapted from Ref. [106].

binding of each CO molecule to the different monoatomic metal tip backgrounds (see also subsection 5.2.2). Hence, the chemical reactivity can only be measured relatively and not in an absolute manner. To eliminate the influence of different bonds between the various CO molecules and metal tip backgrounds, the chemisorption force minima $F_{z,\mathrm{SR}}(z_{\mathrm{chem}}, c^*)$ are normalized[1] with respect to the chemisorption force minima $F_{z,\mathrm{SR}}(z_{\mathrm{chem}}, 0)$ of the single Fe adatom (see Fig. 5.8(b)). The normalized $F_{z,\mathrm{SR}}(z_{\mathrm{chem}}, c^*)/F_{z,\mathrm{SR}}(z_{\mathrm{chem}}, 0)$ curve decreases with increasing reduced coordination number c^*. Hence, using a CO tip as a probe, it can be concluded that the single Fe adatom ($c^* = 0$) is most chemically reactive, followed by the corner Fe atoms ($c^* = 2$) and the edge atoms ($c^* = 3, 4$). Fe atoms with six nearest-neighbors within the xy plane ($c^* = 6$) are least chemical reactive.

5.3.2. Influence of CO Tip Bending and the Lateral Position on the Short-Range Force Spectra Acquired on Fe Clusters

Two minima in a vertical force versus distance curve can potentially be a result of the lateral deflection of the CO molecule on the tip (see also subsection 5.2.3). In case of the single Fe adatom, the CO remains upright during the acquisition of the $F_{z,\mathrm{SR}}(z, 0)$ curves as the lateral forces above the radially symmetric attractive center of the Fe adatom are zero (see subsection 5.2.3).

The $F_{z,\mathrm{SR}}(z, c^*)$ spectra presented above are recorded at the most attractive (x, y) positions of the atomically resolved $\Delta f(x, y)$ images of the Fe clusters. At these positions, the lateral forces are typically zero. Hence, by recording the $F_{z,\mathrm{SR}}(z, c^*)$ spectra on the most attractive (x, y) positions of the atomically resolved $\Delta f(x, y)$ images, the lateral forces acting on the CO tips are minimized and CO bending is suppressed. In the following, this statement is proven by investigating vertical and lateral force curves at small tip-sample distances across a ten-atom Fe cluster, calculated by DFT[2]. Figures 5.9(b) and (c) show the calculated vertical ($F_{z,\mathrm{DFT}}(x')$) and lateral ($F_{x,\mathrm{DFT}}(x')$) force curves between a Fe decamer and a CO

[1] This normalization method is inspired by Ref. [125]. In Ref. [125], the normalization method is used in order to distinguish between different atomic species of a monolayer consisting of Sn, Pb and Si atoms grown on Si(111).

[2] Experimentally, the lateral force traces cannot be recorded at these small tip-sample distances as their magnitude in-between the Fe atoms would result in significant bending of the CO molecule on the tip probably leading to a change of the tip's termination.

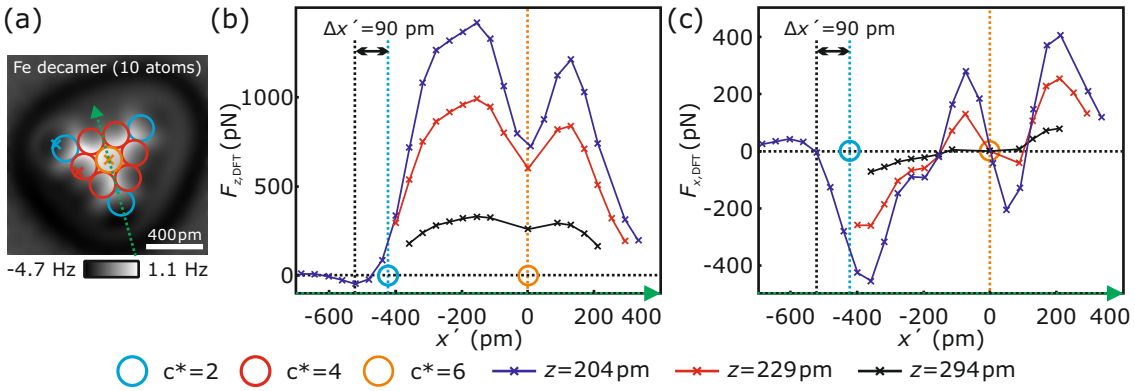

Figure 5.9. (a) Same atomically resolved $\Delta f(x, y)$ image of the ten-atom Fe cluster (Fe decamer) as shown in Fig. 5.5(b). The green dotted arrow indicates the x' axis in panels (b) and (c). (b) Vertical force $F_{z,\mathrm{DFT}}(x')$ and (c) lateral force $F_{x,\mathrm{DFT}}(x')$ curves derived by DFT calculations using a single rigid CO molecule as a tip for three different tip-sample distances $z = \{204\,\mathrm{pm}, 229\,\mathrm{pm}, 294\,\mathrm{pm}\}$ across the top corner atom ($c^* = 2$) and central atom ($c^* = 6$) of the Fe decamer (as indicated by the green dotted arrow in panel (a)). The absolute core-core distances between the tip's O atom and the central atom of the Fe cluster ($c^* = 6$) are transformed to the tip-sample distance z (see subsection 2.3.1). Here, the calculated adsorption height $h = 207\,\mathrm{pm}$ of the central atom ($c^* = 6$) is used. The blue and orange colored circles indicate the lateral positions of the cluster's corner ($c^* = 2$) and central atom ($c^* = 6$) along the x' axis. Figure adapted from Ref. [106].

molecule in dependence of the lateral position x' indicated by the green dotted arrow in Fig. 5.9(a). The center position of the central Fe atom ($c^* = 6$, $x' = 0$) matches the lateral position of the vertical local force minimum for all three calculated distances $z = \{204\,\mathrm{pm}, 229\,\mathrm{pm}, 294\,\mathrm{pm}\}$ (see vertical orange dotted line in Fig. 5.9(b)). Additionally, the lateral force $F_{x,\mathrm{DFT}}(x' = 0)$ is zero for $z = \{204\,\mathrm{pm}, 229\,\mathrm{pm}, 294\,\mathrm{pm}\}$ above the center of the central atom (see Fig. 5.9(c)). Hence, the CO molecule remains upright when approaching the tip towards the central Fe atom's center of the Fe decamer. In case of the Fe decamer's corner atom ($c^* = 2$), the lateral position of maximal vertical attraction is laterally offset by 90 pm with respect to the center of the corner atom (vertical black dotted line versus vertical light blue dotted line in Fig. 5.9(b)). The lateral force at the lateral position of maximal vertical attraction is zero (as indicated by the vertical black dotted line in Fig. 5.9(c)). Therefore, the CO molecule remains upright during the vertical approach to the lateral position of maximal vertical attraction and the double minima shape of the vertical short-range force curves $F_{z,\mathrm{SR}}(z, c^*)$ are not a

result of CO bending. This conclusion is further supported by the DFT calculations that qualitatively reproduce the experimental $F_{z,\mathrm{SR}}(z, c^*)$ curves using a rigid CO molecule as a tip (see Fig. 5.5(c)).

The experimental $F_{z,\mathrm{SR}}(z, c^*)$ curves were recorded about 90 pm off-center of the Fe atoms in case of $c^* = 2, 3, 4, 5$ (see colored crosses in Fig. A.2 of the appendix). In case of the single Fe adatom, it is shown (see subsection 5.2.1) that almost no hybridization of the electronic orbitals of CO tip and Fe adatoms occurs if the CO tip is laterally offset by 200 pm to the center of the Fe adatom. This leads to the appearance of the Fe adatom as a repulsive torus with radius 200 pm centered around an attractive hole in the $F_{z,\mathrm{SR}}(x, y, z = \text{const.})$ image [42] (see Fig. 5.3(a)). In the following, the influence of the lateral offset of 90 pm with respect to the center of the Fe atom on the hybridization of the electronic orbitals of CO tip and Fe atom, i.e. on the vertical short-range force curves $F_{z,\mathrm{SR}}(z, c^*)$ is exemplarily discussed for the single Fe adatom ($c^* = 0$). Figure 5.10 shows three $F_{z,\mathrm{SR}}(z, 0)$ curves acquired above the center of the Fe adatom ($\Delta x = 0$) and laterally offset with respect to the center of the Fe adatom ($\Delta x = 50$ pm and $\Delta x = 75$ pm, respectively). All three curves show a physisorption (local) force minimum at $z = z_{\mathrm{phys}}$ and a chemisorption (global) force minimum at $z = z_{\mathrm{chem}}$. Hereby, the chemisorption force minima $F_{z,\mathrm{SR}}(z_{\mathrm{chem}}, 0)$ do not deviate significantly in magnitude for the three different lateral positions (−231 pN, −222 pN and −230 pN). Consequently, a lateral

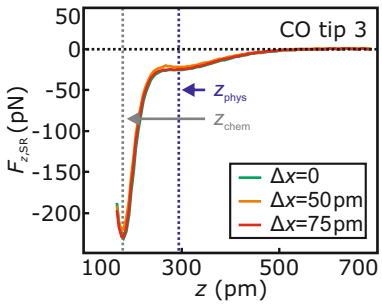

Figure 5.10. Three $F_{z,\mathrm{SR}}(z, 0)$ curves acquired above the center of a Fe adatom ($\Delta x = 0$) and laterally offset by $\Delta x = 50$ pm and $\Delta x = 75$ pm with respect to the center of the Fe adatom. All curves show a physisorption force minimum and a chemisorption force minimum as indicated by the vertical blue and gray dotted lines, respectively. The chemisorption force minima $F_{z,\mathrm{SR}}(z_{\mathrm{chem}}, 0)$ do not differ significantly. The $F_{z,\mathrm{SR}}(z_{\mathrm{chem}}, 0)$ curve at $\Delta x = 0$ is also presented in Ref. [106].

offset of $\Delta x = 75\,\mathrm{pm}$ does not lead to a significant decrease of hybridization of the electronic orbitals of the CO tip and the Fe adatom. Therefore, it can be concluded that the lateral offset of about 90 pm with respect to the Fe atoms' centers during the acquisition of the $F_{z,\mathrm{SR}}(z, c^*)$ spectra on various Fe atoms of small Fe clusters ($c^* = 2, 3, 4, 5$) does not substantially effect the hybridization of the electronic orbitals of the CO tip and investigated Fe atom. Hence, the chemisorption force minima of the $F_{z,\mathrm{SR}}(z, c^*)$ curves are an appropriate measure to investigate the chemical reactivity of the clusters' individual Fe atoms. However, if the $F_{z,\mathrm{SR}}(z, c^*)$ spectra are recorded on top of the individual cluster Fe atoms with $c^* = 2, 3, 4, 5$, the relatively large lateral forces (see Fig. 5.9(c)) will cause a considerable tilt of the CO probably leading to artifacts in the $F_{z,\mathrm{SR}}(z, c^*)$ curves (see also subsection 5.2.3). Hence, to prevent CO tip tilt, the $F_{z,\mathrm{SR}}(z, c^*)$ curves are recorded in the most attractive positions of the $\Delta f(x, y)$ images which are typically laterally offset by about $\Delta x = 90\,\mathrm{pm}$ to the center positions of the individual Fe atoms in case of $c^* = 2, 3, 4, 5$.

5.3.3. Energy Spectroscopy on Individual Fe Cluster Atoms

Next, the physisorption energy minima[1] extracted from the corresponding short-range energy versus distance curves $E_{\mathrm{SR}}(z, c^*)$, depicted in Fig. A.3 of the appendix, are investigated. Hereby, z_{phys} indicates the position of the physisorption energy minimum (i.e. the minimum at larger tip-sample distance z). The energy minima $E_{\mathrm{SR}}(z_{\mathrm{phys}}, c^*)$ become more negative (attractive) with increasing reduced coordination number c^* (see Fig. 5.11). It is found that $E_{\mathrm{SR}}(z_{\mathrm{phys}}, c^*)$ does not depend on the cluster size. The increase in attraction of $E_{\mathrm{SR}}(z_{\mathrm{phys}}, c^*)$ as a function of c^* can be explained by an increase of van-der-Waals interaction with rising c^*, i.e. the increasing number of neighboring Fe atoms. However, the situation is more complicated as the local electrostatic interaction may vary with the reduced coordination number c^* as well. Hereby, depending on the sign of the local charge of the investigated Fe atom, the electrostatic interaction can lead to additional attraction or repulsion on the in-total positively charged CO tip [38, 39]. The separation of van-der-Waals and electrostatic contribution is not possible in the

[1] The physisorption energy minima $E_{\mathrm{SR}}(z_{\mathrm{phys}}, c^*)$ are fully resolved in all $E_{\mathrm{SR}}(z, c^*)$ curves which is not the case for the chemisorption energy minima $E_{\mathrm{SR}}(z_{\mathrm{chem}}, c^*)$.

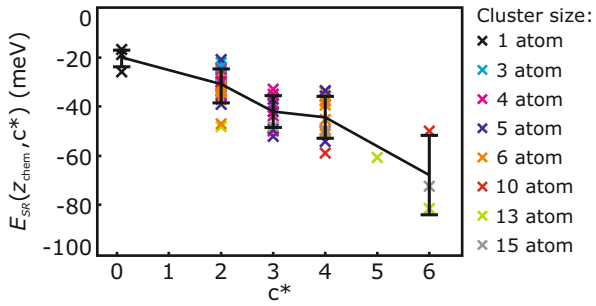

Figure 5.11. Physisorption energy minima $E_{\mathrm{SR}}\left(z_{\mathrm{phys}}, c^*\right)$ as a function of reduced coordination number c^*. The corresponding short-range energy versus distance curves $E_{\mathrm{SR}}\left(z, c^*\right)$ are depicted in Fig. A.3 of the appendix. The error bars indicate the standard deviation of the mean value of the physisorption energy minima $E_{\mathrm{SR}}\left(z_{\mathrm{phys}}, c^*\right)$ with respect to c^*. Figure adapted from Ref. [106].

presented experimental results. Recently, it was found that scanning dot microscopy is able to probe the electric potential of single atoms, molecules and metal-organic structures [126, 127] which could in principle be used to study the electric potential within small Fe clusters. This would help to discriminate between the electrostatic and van-der-Waals contribution.

5.4. Analysis of the Atomic Contrast of Small Fe Clusters

The introduction of CO tips in nc-AFM enabled unprecedented atomic resolution on various sample systems [33–36, 39, 40] including organic molecules [32]. It was shown that Pauli repulsion at small tip-sample distances is responsible for the atomic contrast in organic molecules [61–63]. In the following, the origin of the atomic contrast of small Fe clusters is investigated. Therefore, a 15-atom Fe cluster is assembled atom by atom which contains four Fe atoms with a reduced coordination number of $c^* = 6$ in its center. Using this specific Fe cluster, the atomic contrast between atoms with $c^* = 6$ and the atomic contrast on the cluster's corner and edge ($c^* = 2, 3, 4$) can be investigated at the same time.

The assembled 15-atom Fe cluster is atomically resolved in the $\Delta f\left(x, y\right)$ image depicted in Fig. 5.12(b). The $\Delta f\left(x, y\right)$ image is obtained in constant-current mode. This mode allows resolving the Fe cluster and the Cu(111) substrate with atomic

resolution at the same time [33, 88]. The corresponding topographic image $z(x, y)$ is presented in Fig. 5.12(c). The atomic positions of the individual Fe atoms of the cluster are indicated by the colored circles. The color of the circles relates to the reduced coordination number c^* of each atom. Here, fcc adsorption of the individual Fe atoms is assumed. This agrees with DFT calculations suggesting that fcc adsorption is energetically most favorable for Fe clusters containing more than two Fe atoms [33]. The cluster's edge atoms appear in the $\Delta f(x, y)$ image as bright tori [33]. One section of the torus of the top corner atom ($c^* = 2$) is indicated by the white arrow. The torus appears in a z distance regime of $z_{\text{torus appearance}} = [180\,\text{pm}, 230\,\text{pm}]$ (see $z(x, y)$ image in Fig. 5.12(c)). Figure 5.12(a) shows vertical short-range force versus distance curves $F_{z,\text{SR}}(z)$ which are recorded at the (x, y) positions marked by the colored crosses in Fig. 5.12(b) through (d). The light blue curve recorded above the Fe cluster's top corner atom ($c^* = 2$) shows two distinct minima, i.e. a physisorption force minimum at $z_{\text{phys}} = 292\,\text{pm}$ and a chemisorption force minimum at $z_{\text{chem}} = 162\,\text{pm}$. The z range of the torus appearance lies between the physisorption and chemisorption force minimum (see gray shaded area in Fig. 5.12(a)). The same holds true for the left corner atom (see $F_{z,\text{SR}}(z, 3)$ spectrum in Fig. 5.12(a)). The appearance of a single Fe adatom as a repulsive torus also occurs in a distance regime in which the CO tip transitions from physi- to chemisorption, i.e. the electronic orbitals of CO tip and Fe adatom start to hybridize [42] (see Fig. 5.3). Hence, the appearance of the corner and edge atoms as repulsive tori is a result of the hybridization of the electronic orbitals of the CO tip and corner or edge atom when the tip is positioned above the Fe atom and the vanishing hybridization if the CO tip is about 200 pm laterally offset to the Fe atom's center.

Figure 5.12(d) depicts a vertical short-range force image $F_{z,\text{SR}}(x, y, z = 335\,\text{pm})$, recorded in constant-height mode, of the same area as shown in Fig. 5.12(b). The z distance is chosen such that a noticeable atomic contrast is achieved. A further lowering of z is experimentally not feasible as significant lateral forces occur in-between the individual Fe atoms which would lead to a CO tip loss if the tip-sample distance z was reduced further. Here, the corner and edge atoms ($c^* = 2, 3, 4$) appear as depressions (dark, attractive features) with repulsion (bright) in-between the atoms. In the $F_{z,\text{SR}}(x, y, z = 335\,\text{pm})$ image, the torus-like structure of single Fe

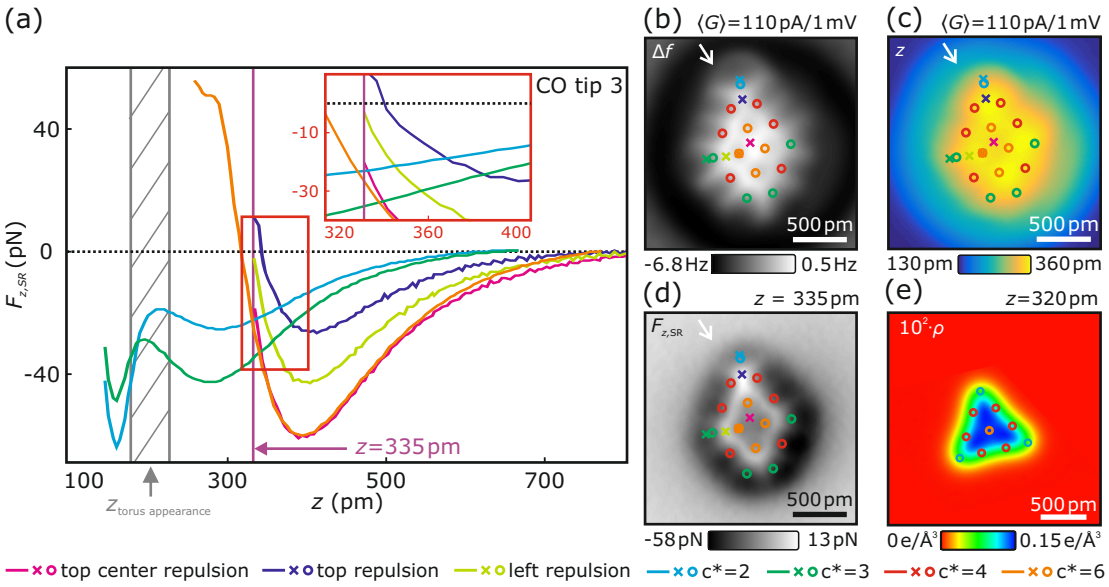

Figure 5.12. (a) Short-range vertical force versus distance curves $F_{z,\mathrm{SR}}(z)$ at various (x, y) positions above an atom-by-atom assembled 15-atom Fe cluster. The inset shows the enlarged region indicated by the red square. (b) Atomically resolved $\Delta f(x, y)$ image of the 15-atom Fe cluster acquired in constant-current mode ($\langle I \rangle = 110\,\mathrm{pA}$, $V_{\mathrm{tip}} = -1\,\mathrm{mV}$). (c) Corresponding topographic image $z(x, y)$ to panel (b). (d) Atomically resolved $F_{z,\mathrm{SR}}(x, y, z = 335\,\mathrm{pm})$ image of the 15-atom Fe cluster of the same cutout as shown in panel (b) and (c). The atomic positions (fcc adsorption) and the (x, y) locations of the $F_{z,\mathrm{SR}}(z)$ spectra are indicated as colored circles and crosses in panels (b) through (d). Hereby, the color of the circles indicates the reduced coordination number c^* of the specific Fe atom. The white arrow indicates the position of a section of the torus of the top corner Fe atom in panel (b). The non-overlayed images of panels (b) and (d) are depicted in Fig. 5.13. (e) Electron charge density $\rho(x, y)$ of a 10-atom Fe cluster at $z = 320\,\mathrm{pm}$ calculated by DFT. The high-symmetry direction of the substrate is rotated by 15° anti-clockwise with respect to the horizontal axis in panel (b) through (e). Figure adapted from Ref. [106].

adatoms is not observed for the corner and edge atoms[1]. The atomic contrast of the top corner atom ($c^* = 2$) occurs 43 pm before the physisorption force minimum is reached (see light blue versus dark blue curve in Fig. 5.12(a)). The same holds true for the left corner atom ($c^* = 3$, dark green curve versus light green curve). Hence, above the atoms the CO tip interacts purely physically with the corner and edge atoms, namely via the attractive van-der-Waals and the electrostatic interaction. The electrostatic interaction results presumably in additional attraction as the edge

[1]The white arrow indicates the (x, y) location of a torus's section in the $\Delta f(x, y)$ image depicted in Fig. 5.12(b).

and corner atoms probably exhibit a local positive charge due the Smoluchowski effect [111]. The dark blue and light green curve acquired in-between the atoms passed their force minima and exhibit a positive force gradient at $z = 335\,\text{pm}$. The dark blue curve is already repulsive. The positive force gradient arises from Pauli repulsion induced by the increased electron charge density in-between the cluster's Fe atoms on the CO tip. The electron charge density $\rho(x, y)$ of small Fe clusters is typically increased in-between the individual Fe atoms as shown exemplarily[1] for a Fe decamer in Fig. 5.12(e) for $z = 320\,\text{pm}$. Therefore, the atomic contrast on the cluster's edge and corner atoms is a result of the van-der-Waals and electrostatic interaction above the Fe atoms and Pauli repulsion in-between the atoms.

The atomic contrast of the Fe cluster's corner and edge atoms in constant-current and constant-height mode have a different origin. While the appearance of the edge and corner atoms in the constant-current mode as tori can be attributed to the chemical bond formation between the CO tip and the individual Fe atom, their appearance as attractive depressions in constant-height mode is a result of the interplay of attractive van-der-Waals interaction and electrostatic interaction above the Fe atoms and Pauli repulsion in-between the Fe atoms. In conclusion, the different tip-sample distances in the constant-current and constant height modes result in the different appearances of the edge and corner atoms.

Next, the origin of the atomic contrast in the Fe cluster's center is analyzed. In the constant-current mode, the atomic resolution in the center of the 15-atom Fe cluster (i.e. in-between the four central atoms with $c^* = 6$) occurs in a distance regime between 330 pm and 350 pm (see Fig. 5.12(b) and (c) and Fig. 5.13(a) for the non-overlayed $\Delta f(x, y)$ image). This regime matches with the z distance of the constant-height scan (see $F_{z,\text{SR}}\,(x, y, z = 335\,\text{pm})$ image in Fig. 5.12(d) and Fig. 5.13(b)). In the constant-current and constant-height scans, the four central atoms are imaged as depressions (dark) with slight repulsion (bright) in-between the Fe atoms. At $z = 335\,\text{pm}$, the value of the $F_{z,\text{SR}}\,(z, 6)$ curve recorded on the left Fe atom within the center of the 15-atom Fe cluster lies between the physisorption force minimum and the second local repulsive force minimum (see orange curve in Fig. 5.12(a)). The presence of the second repulsive force minimum of the $F_{z,\text{SR}}\,(z, 6)$

[1]The charge density $\rho(x, y)$ of the Fe decamer is calculated by DFT. The charge density of the 15-atom Fe cluster is not calculated, yet.

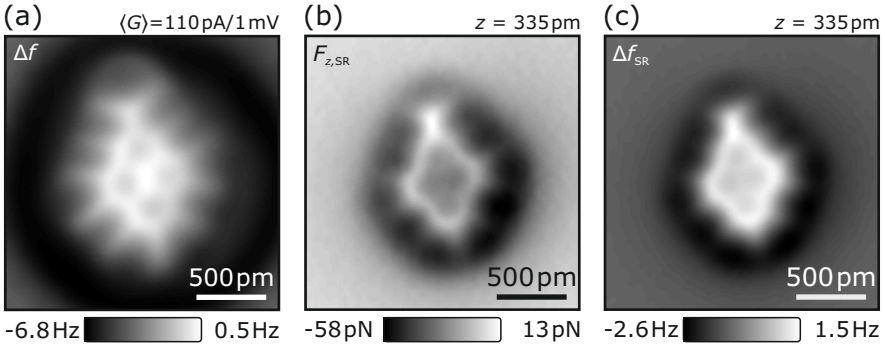

Figure 5.13. (a) Same $\Delta f\,(x, y)$ image as depicted in Fig. 5.12(b) without the colored circles and crosses. (b) Identical $F_{z,\mathrm{SR}}\,(x, y, z = 335\,\mathrm{pm})$ image of the 15-atom Fe cluster as shown in Fig. 5.12(d) but without overlayed atomic sites and spectra positions. (c) Corresponding short-range image $\Delta f\,(x, y, z = 335\,\mathrm{pm})$ prior to vertical short-range force deconvolution of the $F_{z,\mathrm{SR}}\,(x, y, z = 335\,\mathrm{pm})$ images depicted in panel (b). The high-symmetry direction of the substrate is rotated by 15° anti-clockwise with respect to the horizontal axis in all panels. Panels (b) and (c) are adapted from Ref. [106].

curve results in a decrease of the slope in the distance regime of 300 pm to 360 pm. The magenta curve acquired in the center of the upper triangle formed by three central atoms exhibits a steeper slope in the same z regime compared to the slope of the $F_{z,\mathrm{SR}}\,(z, 6)$ curve. This can be attributed to the absence of an additional attractive force in-between the Fe atoms. Hence, the atomic contrast within the center of the 15-atom Fe cluster is a result of the presence of the second local force minimum in the $F_{z,\mathrm{SR}}\,(z, 6)$ curve.

In summary, the atomic contrast in the constant-current mode is a result of the presence of the chemisorption force minima in the vertical short-range force curves $F_{z,\mathrm{SR}}\,(z, c^*)$ above the individual Fe atoms of the 15-atom Fe cluster. This leads to the tori-like appearance of the edge and corner atoms, similar to the single Fe adatoms. In constant-height mode, the atomic resolution within the Fe cluster's center is also a result of the presence of the chemisorption force minimum while the atomic contrast of the edge and corner atoms is a consequence of van-der-Waals and electrostatic interaction above the Fe atoms and of the Pauli repulsion in-between the Fe atoms.

5.5. Possible Hydrogenation of Small Fe Clusters

It was surprising to find that in long-term observations of small Fe clusters their appearance can change over time. The rate of the appearance change increases with the time t during which the microscope is at its base temperature $T_{\mathrm{mic}} = 5.7\,\mathrm{K}$. When the cryostat had been cooled down recently (i.e. $t = [0, 14\,\mathrm{d}]$) from liquid nitrogen temperatures to its base temperature, the assembled Fe clusters did not change their appearance in the STM and atomically resolved AFM images. However, after a couple of weeks, Fe clusters change their appearance over time. In the following, these changes in the appearance are discussed.

Figure 5.14(a) shows an atomically resolved $\Delta f(x, y)$ image of an atom-by-atom assembled 13-atom Fe cluster recorded in constant-current mode[1]. The $\Delta f(x, y)$ image is highly symmetric except for a sharp change indicated by the white arrow. After the acquisition of the $\Delta f(x, y)$ image depicted in Fig. 5.14(a), the Fe cluster is imaged again using the same scan parameters. The corresponding $\Delta f(x, y)$ image is similar to the $\Delta f(x, y)$ image shown in Fig. 5.14(a). However, it additionally exhibits a bright spot (as indicated by the red arrow in Fig. 5.14(b)). Therefore, the appearance of the 13-atom Fe cluster changed during the acquisition of the $\Delta f(x, y)$ image shown in Fig. 5.14(a). As the slow scanning direction is chosen from bottom to top, the change in the appearance, except for the sharp change, is not detected in the $\Delta f(x, y)$ image viewed in Fig. 5.14(a). After the acquisition of the $\Delta f(x, y)$ image depicted in Fig. 5.14(b), a three-dimensional set of constant-height images is recorded. Figure 5.15(a) shows the experimental $F_{z,\mathrm{SR}}(x, y)$ image[2] of the closest scan at $z = 353\,\mathrm{pm}$. The adsorption geometry is calculated using DFT [83].

The individual Fe atoms adsorb on or close to fcc hollow sites (see magenta colored circles): The six corner atoms are laterally offset from the ideal fcc adsorption by 26 pm towards the center of the Fe cluster. The six neighboring Fe atoms of the central atom are laterally offset by 9 pm towards the central Fe atom. Maximal repulsion occurs in-between the individual Fe atoms, similar to the 15-atom Fe cluster discussed in section 5.4. Figure 5.15(b) shows the calculated [83] electron charge density $\rho(x, y, z = 353\,\mathrm{pm})$ of a 13-atom Fe cluster with an additional H

[1] This cluster was created together with Stilp and the corresponding images are also depicted in his bachelor thesis (see Figs. 2.18(e) and (f) in Ref. [114]).

[2] The experimental results depicted in Figs. 5.15(a) and (d) are presented in a similar fashion in Figs. 2.20(a) and (b) of Ref. [114].

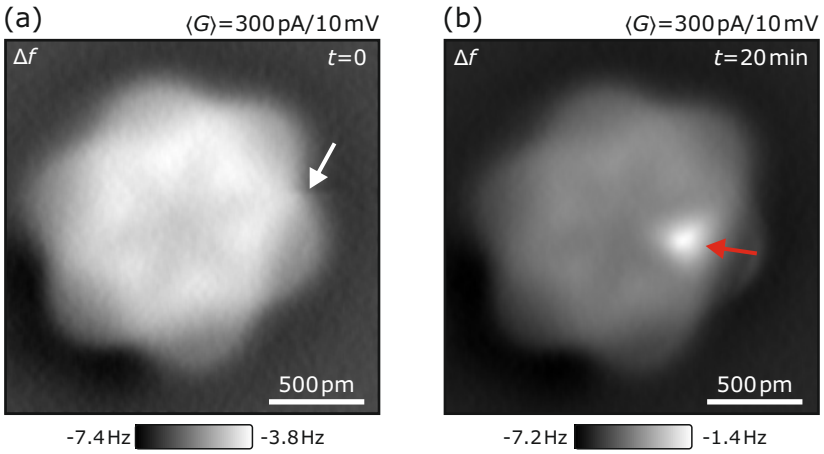

Figure 5.14. (a) and (b) Consecutively recorded $\Delta f(x, y)$ images showing atomic resolution of an atom-by-atom assembled 13-atom Fe cluster. The images are acquired in constant-current mode using $\langle I \rangle = 300\,\text{pA}$ and $V_{\text{tip}} = -10\,\text{mV}$. The white (red) arrow in panel (a) ((b)) indicates a sharp change (bright feature) in the $\Delta f(x, y)$ image. Note that the high-symmetry direction of the substrate is rotated by 15° anti-clockwise with respect to the horizontal axis. The experimental data shown in this figure is also presented in Ref. [114].

atom in the second layer. The green colored circle indicates the lateral position of the H atom. A perspective view of the geometrical structure is shown in Fig. 5.15(c). The charge density is increased in-between the Fe atoms. Therefore, the repulsion in-between the Fe atoms in the experimental $F_{z,\text{SR}}(x, y)$ image depicted in Fig. 5.15(a) can be explained by Pauli repulsion on the CO tip induced by the increased electron charge density in-between the Fe atoms. Moreover, the electron charge density $\rho(x, y, z = 353\,\text{pm})$ is locally further increased at the location of the H atom. The experimental $F_{z,\text{SR}}(x, y)$ image shows stronger repulsion on the position indicated by the green colored circle in Fig. 5.15(a). Hence, the increased repulsion of the experimental $F_{z,\text{SR}}(x, y)$ image at the lateral position indicated by the green colored circle in Fig. 5.15(a) might be explained by an adsorption of a H atom in the second layer of the 13-atom Fe cluster. This suggestion is further supported by comparing the experimental $F_{z,\text{SR}}$ curve along the orange colored ring depicted in Fig. 5.15(a) with the vertical forces calculated by DFT (see orange colored curves and black crosses in Fig. 5.15(d)). DFT calculations [83] lead to an increased repulsive force of 9.69 pN above the H atom compared to equivalent positions without a H atom (2.37 pN). In summary, the change in appearance of

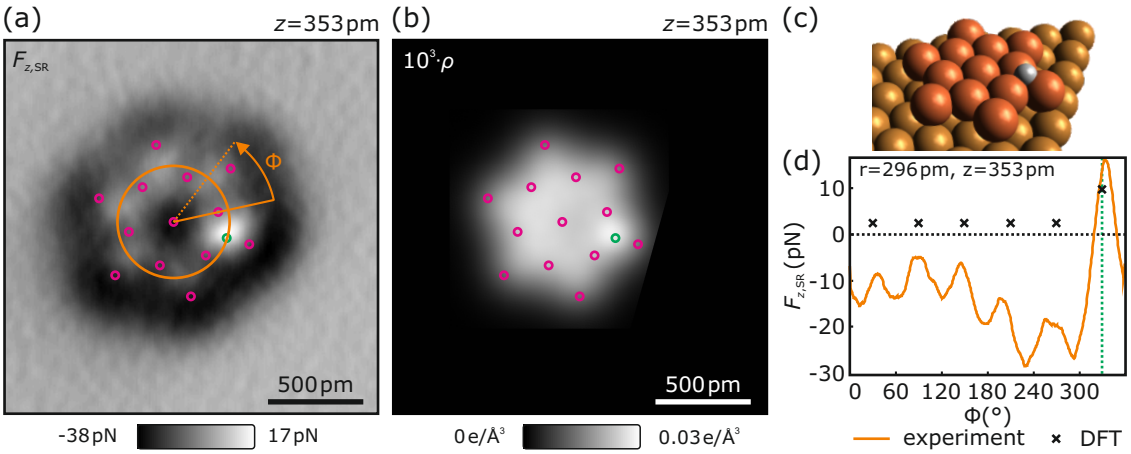

Figure 5.15. (a) $F_{z,\mathrm{SR}}(x, y)$ image of the 13-atom Fe cluster shown in Fig. 5.14(b) recorded at $z = 353\,\mathrm{pm}$. The magenta colored circles indicate the (x, y) positions of the individual Fe atoms as calculated by DFT [83]. (b) Electron charge density $\rho(x, y, z = 353\,\mathrm{pm})$ of a 13-atom Fe cluster (magenta colored circles) with a single H atom on top (green colored circle) derived by DFT calculations [83]. (c) Perspective view of the atomic arrangement of the 13-atom Fe cluster (orange colored atoms) with a H atom on top (gray colored atom) adsorbed on the Cu(111) surface (gold colored atoms) as calculated by DFT [83]. The adsorption height h of the central Fe atom is 205 pm. The H atom adsorbs in a hollow site with a vertical offset of 97 pm with respect to the central Fe atom. (d) Experimental $F_{z,\mathrm{SR}}$ curve along the orange colored circle, depicted in panel (a), with radius $r = 296\,\mathrm{pm}$ against radial angle Φ. The vertical forces at specific positions of the circle above the 13-atom Fe cluster including the H atom position are calculated by DFT [83] (black crosses). The vertical green dotted line indicates the position of the H atom in the DFT calculations [83]. The experimental data shown in panel (a) and (d) are also presented in Ref. [114].

the 13-atom Fe cluster, as shown in Fig. 5.14, might be a result of the adsorption of a H atom in the second layer of the Fe cluster. DFT calculations [83] investigated whether structural changes of the 13-atom Fe cluster without a H atom in the second layer can result in a change of the appearance of the cluster. However, a structural reconfiguration which could induce a change in the appearance of the Fe cluster can be excluded as a second stable adsorption geometry is not found [83].

Consequently, a single H atom might have adsorbed on the 13-atom Fe cluster during the image acquisition of the $\Delta f(x, y)$ image depicted in Fig. 5.14(a). However, atomic hydrogen was not dosed into the UHV chamber. As the experiments are conducted at liquid helium temperatures, all residual gases except for hydrogen

and helium[1] are immobilized (see section 3.1). Additionally, it is experimentally observed that the amount of molecular hydrogen (H_2) increases over time within the cold He shields [128]. Molecular hydrogen can dissociate to atomic hydrogen[2] in the vicinity of a catalyst such as single Ti atoms on hBN at 50 K or single Fe adatoms on Pt(111) [29, 131–133]. While dissociation does not occur on the bare Cu(111) surface [134], the catalytic properties of single Fe adatoms could in principle foster a dissociation [133, 135, 136]. Furthermore, hydrogen is quite mobile on various chemically-nonreactive surfaces such as Cu(111), and it can be accidentally or intentionally trapped between tip and sample which can lead to image artifacts or enable intramolecular resolution in scanning tunneling microscopy [137–139].

The molecular hydrogen originating from the residual gas within the UHV chamber can cause the appearance of the repulsive feature in the $\Delta f(x, y)$ image depicted in Fig. 5.14(b) in three possible scenarios: Either, molecular hydrogen is dissociated at a nearby located single Fe adatom, and afterwards, a single H atom diffuses to the Fe cluster and adsorbs on its second layer[3]. Another possibility is that H_2 diffuses to the Fe cluster, dissociates at the cluster and one out of two H atoms adsorbs on the Fe cluster while the other one diffuses away or adsorbs somewhere at the side of the tip[4]. A third possible explanation is the non-dissociative adsorption of a single H_2 molecule on the Fe cluster, assuming that the adsorption of a single H_2 molecule leads to the appearance of a single repulsive feature. The last two scenarios have not yet been checked by DFT calculations.

The adsorption mechanisms for H and H_2 on an adsorbent differ. While a single H atom probably binds strongly to the Fe cluster by forming a chemical bond (chemisorption), H_2 presumably adsorbs via the weaker van-der-Waals interaction[5] (physisorption). As the adsorption of H_2 does not involve the formation of a chemical bond, it could be more easily manipulated on the Fe cluster compared to a single H atom. Emmrich *et al.* [33] present an atomically resolved $\Delta f(x, y)$ image of

[1] A rest gas analysis within the UHV chamber shows that the amount of H_2 is bigger by three orders of magnitude than the amount of He. Therefore, the influence of He is neglected in the remainder.
[2] The dissociation energy of a H_2 molecule in the gas phase is 4.5 eV [129] and, hence, 41% of the dissociation energy of a CO molecule in the gas phase (11.1 eV) [130].
[3] The resulting charge density and vertical forces calculated by DFT for a 13-atom Fe cluster with a H atom adsorbed on the second layer show similarities with the experimental observations of the 13-atom Fe cluster with a bright feature on top of it.
[4] Otherwise two repulsive features would evolve.
[5] Unless it is not dissocitated to two hydrogen atoms due to the catalytic properties of Fe clusters.

a 15-atom Fe cluster which exhibits a bright feature on top of the cluster. The bright feature is interpreted as an atom in the second layer of the Fe cluster [33]. Furthermore, it was accidentally manipulated laterally to another position while scanning the Fe cluster in constant-current mode. This observation supports the scenario that the adsorption of a H_2 molecule is responsible for the appearance of the repulsive features on top of small Fe clusters as they can be laterally manipulated more easily compared to atomic hydrogen. However, the binding energies of molecular and atomic hydrogen on small Fe clusters adsorbed on Cu(111) are currently unknown.

In order to get further insight on the evolution of additional repulsive features, another 13-atom Fe cluster is assembled atom by atom and repeatedly imaged in constant-current mode. Figure 5.16(a) shows a $\Delta f(x, y)$ image of that second 13-atom Fe cluster recorded in constant-height mode at $z = 404\,\text{pm}$ prior to consecutive scanning in constant-current mode. For clarity, the atomic positions of the individual Fe atoms resulting from DFT calculations are overlayed as magenta colored circles. The green colored circles indicate the experimentally determined positions of two repulsive features. Figure 5.16(b) shows a $\Delta f(x, y)$ image of the same 13-atom Fe cluster recorded 909 min after the acquisition of the first $\Delta f(x, y)$ image depicted in Fig. 5.16(a). Thereby, the number of repulsive features increased from 2 to 6 (as indicated by the green colored circles). Between the acquisition of both $\Delta f(x, y)$ images, the Fe cluster is scanned[1] in constant-current mode every 20 min. Selected topographic images $z(x, y)$ are shown in Figs. 5.16(c)-(g). At $t = 16\,\text{min}$, the 13-atom Fe cluster appears symmetric except for a diffuse shadow-like area in the top right part of the image[2] (see Fig. 5.16(c)). The Fe cluster's apparent height is 223 pm. The appearance of the Fe cluster does not change in the consecutive topographic scans until $t = 182\,\text{min}$. At $t = 182\,\text{min}$, an additional feature indicated by the red arrow in Fig. 5.16(d) is present in the lower part of the Fe cluster and the apparent height increased by 2 pm compared to the $z(x, y)$ image at $t = 16\,\text{min}$.

[1] Technically, a three-dimensional constant-height set with active drift compensation is recorded using an adapted LabVIEW routine based on the routine introduced in Ref. [75]. To determine changes in the drift speeds, topographic images are acquired in constant-current mode every 20 min.

[2] The shadow-like feature is probably a result of a small macroscopic tip tilt of the CO tip with respect to the normal vector of the Cu(111) surface.

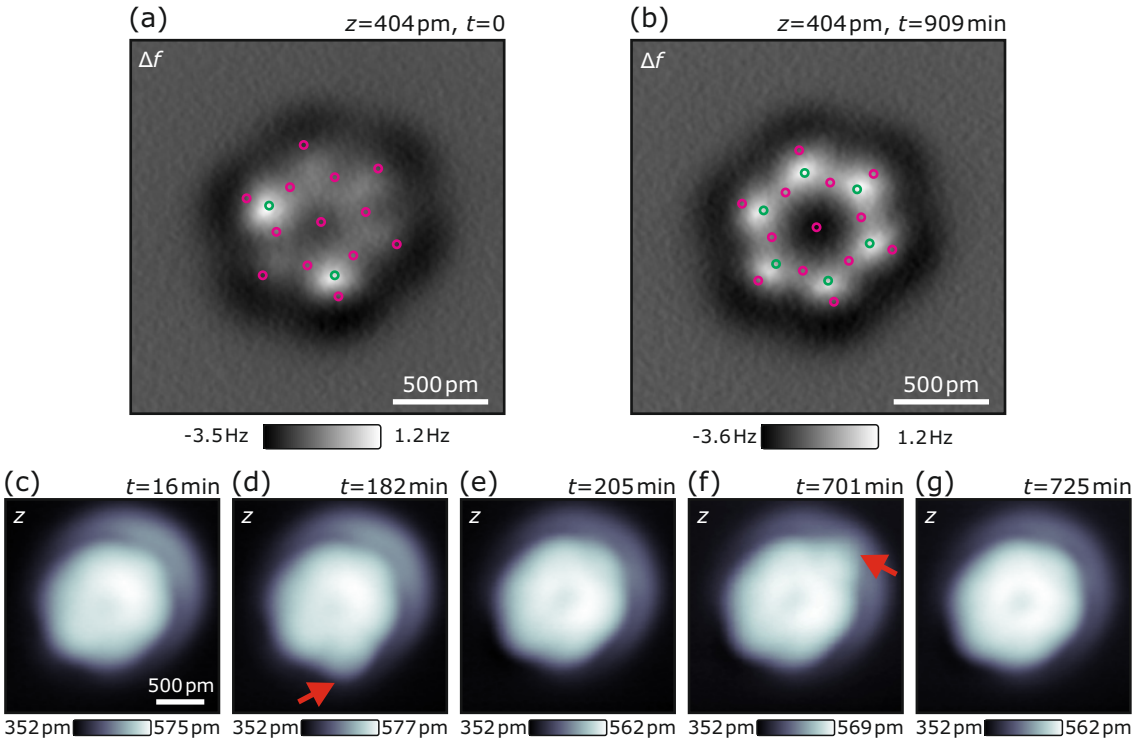

Figure 5.16. $\Delta f(x, y, z = 404\,\text{pm})$ images of a second atom-by-atom assembled 13-atom Fe cluster at (a) $t = 0$ and (b) $t = 909\,\text{min}$, respectively. The magenta colored circles indicate the calculated [83] positions of the Fe atoms while the green colored circles mark the locations of repulsive features. (c) through (g) Consecutively acquired $z(x, y)$ images ($\langle I \rangle = 10\,\text{pA}$, $V_{\text{tip}} = -10\,\text{mV}$) of the 13-atom Fe cluster at $t = 16\,\text{min}$, $t = 182\,\text{min}$, $t = 205\,\text{min}$, $t = 701\,\text{min}$ and $t = 725\,\text{min}$. The red arrows in panels (e) and (f) indicate temporal lateral enlargements of the Fe cluster.

23 min later, the additional feature disappears and the apparent height decreases by 15 pm to 210 pm. The appearance in the subsequently recorded topographic images does not change until $t = 701\,\text{min}$. At $t = 701\,\text{min}$, the topographic image exhibits a lateral enlargement at another position of the Fe cluster and the apparent height increases by 7 pm (see Fig. 5.16(f)). 24 min later, the enlargement vanishes and the apparent height decreases to 210 pm. In summary, two temporal enlargement events occur during the acquisition of the topographic images. This observation can be explained by a diffusion of either two H atoms, two H_2 molecules or a H atom and a H_2 molecule to the Fe cluster. The $\Delta f(x, y)$ images recorded before and after the consecutive topographic scans reveal that four additional repulsive features evolve between $t = 0$ and $t = 909\,\text{min}$. This evolution could be explained

by the diffusion of two H_2 molecules to the Fe cluster, the dissociation of these two H_2 molecules to four H atoms in the vicinity of the Fe cluster and the adsorption of the four H atoms on the Fe cluster at the positions indicated by green colored circles in Fig. 5.16(b). However, it might be that not all diffusion events are captured in the topographic scans. Hence, the four additional features in the $\Delta f(x, y)$ image can also be explained by two more H_2 molecules which diffused unnoticed to the Fe cluster and physisorbed on top of it. Alternatively, the appearance of four additional features could be a result of the adsorption of four H atoms on the cluster which diffused to the cluster beforehand while only the diffusion of two H atoms is captured in the constant-current images.

In the following, the findings of this section are briefly summed up: At first, a single repulsive feature evolved during the scan of the first 13-atom Fe cluster (see Fig. 5.14) which can be explained by either the chemisorption of a single H atom or by the physisorption of a single H_2 molecule. In Ref. [33], a similar single repulsive feature is accidentally manipulated laterally on a 15-atom Fe cluster during imaging in constant-current mode suggesting that the bond between the adsorbate and the Fe cluster is relatively weak. The latter observation fosters the adsorption of a H_2 molecule on the Fe cluster but it can also be explained by the adsorption of a H atom[1]. The last discussed experimental results of the second 13-atom Fe cluster shown in Fig. 5.16 can be explained by the diffusion of two H_2 molecules to the Fe cluster which dissociated to 4 single H atoms which then adsorbed on top of the Fe cluster causing the additional four repulsive features. However, not all diffusion events might be captured in the constant-current scans and two more H_2 might be diffused unnoticed towards the Fe cluster and adsorbed on top of it causing four additional repulsive features in the $\Delta f(x, y)$ image in Fig. 5.16(b).

Overall, a clear conclusion whether the adsorption of atomic or molecular hydrogen is responsible for the appearance of additional repulsive features cannot be drawn at the present stage of the study. In all cases, either atomic hydrogen or molecular hydrogen is likely to be responsible for the appearance of the repulsive features. Hence, further theoretical work on the specific system (i.e. small Fe cluster on Cu(111)) is needed as, so far, both chemisorption upon dissociation and physisorption

[1]The adsorption energy of a single H atom and H_2 molecule on a Fe cluster is unknown, so far.

of H_2 molecules on Fe clusters is reported for Fe clusters in the gas phase [135, 136, 140].

Moreover, the lateral positions of the repulsive features do not agree with the *active sites* on the Fe clusters as determined with the CO tips: In section 5.3 it was found that the tip's CO is mostly attracted to the centers of the Fe cluster's individual atoms[1]. In this section, it was shown that the additional repulsive features evolve in-between the cluster's Fe atoms. This observation indicates that the location of the *active sites* of Fe clusters depend on the atomic species of the adsorbate. In case of hydrogen[2], the *active sites* seem to lie in-between the Fe cluster's individual atoms.

[1] A slight lateral offset of 90 pm is reported for Fe atoms with $c^* = 2, 3, 4, 5$.

[2] Whether the adsorption of atomic or molecular hydrogen results in the appearance of additional repulsive features is still unclear.

6. Summary

The first part of this work demonstrates that CO tips can be used to assemble small Fe clusters with atomic precision via the lateral manipulation of single Fe adatoms (chapter 4). The second part studies the chemical reactivity of small Fe clusters on the atomic scale using the same tips (chapter 5).

In chapter 4, the lateral manipulation of single Fe adatoms using monoatomic metal tips and CO-terminated monoatomic metal tips was compared. It was found that both tips reliably laterally manipulate single Fe adatoms on the Cu(111) surface in the attractive pulling mode. The determined force thresholds needed to be overcome to laterally manipulate a single Fe adatom were identical for the monoatomic metal and CO tip. However, the detected force thresholds were significantly lower than theoretically expected. This was attributed to a lowering of the diffusion barrier due to the presence of the tip. Furthermore, it was found that the lateral force profiles between the tips and the Fe adatoms are slightly asymmetric with respect to the center of the Fe adatom. This asymmetry was attributed to the tilt of the tips. The asymmetry of the lateral force curves acquired with a monoatomic metal and a CO tip were reversed with respect to each other although both tips exhibit a tip tilt in the same direction. Furthermore, it was shown that the tilt direction of the tip did not change prior and after functionalization with a CO molecule.

The experimental observations were confirmed by applying a two-dimensional, analytic model using van-der-Waals and electrostatic interactions. It was concluded that the reversed dipoles of the CO tip and the monoatomic metal tip are responsible for the reversed asymmetry of the lateral force curves of both tips. The robustness of the analytic model was verified by varying its input parameters.

In addition, it was shown that CO tips can be used to assemble small Fe clusters atom by atom. Using CO tips instead of metal tips to build up Fe clusters allowed studying the created clusters on the atomic scale without changing the tip

termination. This had been not possible beforehand as metal tips do not allow resolving the clusters on the atomic scale. Using CO tips, various Fe cluster including five different 5-atom Fe clusters were built up atom by atom. It was shown that all five 5-atom Fe clusters adsorbed in a flat geometry on the Cu(111) substrate which might be valuable for theoretical calculations of their magnetic moment in the future. Furthermore, it was proven that CO tips are relatively robust as they do not change during the assembly of small Fe clusters.

In chapter 5, the atom-by-atom assembled Fe clusters were investigated in detail. In the beginning, the terminology concerning reduced coordination number and the concept of physi- and chemisorption were introduced. Afterwards, the building block of small Fe clusters – the single Fe adatom – was revisited: A vertical short-range force versus distance curve with two minima recorded above the center of a single Fe adatom with a CO tip was presented. Following the findings of Ref. [42], the presence of the second minimum at smaller tip-sample distance was attributed to the hybridization of the electronic orbitals of the CO tip and the single Fe adatom. This hybdridization results in the formation of a chemical bond between CO tip and the single Fe adatom at close distances [42]. Hence, the CO tip transitions from physisorption to chemisorption when approaching the center of a single Fe adatom [42]. 200 pm off-center, chemisorption between the CO tip and the Fe adatom does not occur resulting in the appearance of single Fe adatoms as repulsive tori in the constant-height vertical force image at a specific tip-sample distance [42]. Furthermore it was shown, that the exact shape of the vertical short-range force versus distance curves above the center of the single Fe adatom changes if a different CO-terminated metal tip was used. This observation was attributed to a different chemical bond between the CO molecule and the metal tip's apex.

Next, vertical short-range force spectroscopy was performed on individual Fe atoms of various atom-by-atom assembled Fe clusters using different CO tips. The vertical short-range force curves exhibited two minima. Accompanying DFT calculations confirmed that the CO tip remained upright during the acquisition of the vertical short-range force curves proving that the appearance of a second minimum is not the result of CO bending. Hence, the force minima at smaller tip-sample distances were interpreted as a result of chemical bond formation between the CO tips and the individual Fe atoms of the Fe clusters, similar to the single Fe adatom.

Moreover, it was shown that the chemisorption force minimum values $F_{z,\mathrm{SR}}(z_{\mathrm{chem}}, c^*)$ (i.e. the values of the $F_{z,\mathrm{SR}}(z, c^*)$ curve's minimum at smaller tip-sample distance z_{chem}) depend, first, on the reduced coordination number of the specific atom c^* and, second, on the specific CO tip. The influence of different CO tips was disentangled by normalizing the $F_{z,\mathrm{SR}}(z_{\mathrm{chem}}, c^*)$ values with the chemisorption force minimum value of the single Fe adatom ($F_{z,\mathrm{SR}}(z_{\mathrm{chem}}, 0)$). The resulting normalized $F_{z,\mathrm{SR}}(z_{\mathrm{chem}}, c^*)/F_{z,\mathrm{SR}}(z_{\mathrm{chem}}, 0)$ value was interpreted as a local measurement of the relative chemical reactivity, i.e. the *active sites*, within a Fe cluster. Here, it was found that the chemical reactivity of a cluster's Fe atom reduces with increasing coordination number c^*. Therefore, it was concluded that the Fe cluster's corner atoms ($c^* = 2$) are most chemical reactive followed by the edge atoms ($c^* = 3, 4$) interacting with a CO tip. Additionally, it was deduced that stable chemical bonds between CO tip and the Fe atoms with $c^* = 6$ are not formed.

Furthermore, the physisorption energy minima (i.e. the energy minima at larger tip-sample distances) of the corresponding short-range energy versus distance curves showed a dependency on the reduced coordination number c^* of the individual Fe atom. This was explained by an increase of van-der-Waals interaction with increasing coordination number c^* neglecting an influence of the electrostatic interaction.

Afterwards, the physical origin of the atomic contrast of small Fe clusters in the nc-AFM images was investigated. In constant-current mode, the corner and edge atoms of small Fe clusters appear as bright tori in the $\Delta f(x, y)$ image, similar to the single Fe adatom in the constant-height mode. It was demonstrated that the atomic contrast of the corner, edge and central atoms ($c^* = 2, 3, 4, 5, 6$) occurs in a distance regime in which the CO tip transitions from physisorption to chemisorption if positioned above the individual Fe atoms of the cluster. This was done by linking the vertical short-range force curves acquired above various lateral positions of an atom-by-atom assembled 15-atom Fe cluster with the atomically resolved $\Delta f(x, y)$ image. Hence, the atomic contrast in constant-current mode is a direct result of the chemical bond formation of the CO tip with the individual Fe atoms of the Fe cluster. If the feedback loop controlling the tip-sample distance was switched off above the Fe cluster and the latter was imaged in constant-height mode, the corner and edge atoms did not appear as tori but as attractive depressions with repulsion in-between the individual atoms. This different appearance of the corner and edge atoms of the Fe cluster in the constant-current and constant-height mode

is a result of the different tip-sample distance at the edge and corner of the Fe cluster. In constant-current mode, the CO tip approached the sample in order to maintain a specific tunneling conductance while in constant-height mode the tip-sample distance remained constant. At constant tip-sample distance, the CO tip does not transition from physisorption to chemisorption when positioned above the corner and edge atoms of the Fe cluster. Moreover, the atomic contrast at the corner and edge atoms in constant-height mode is a result of van-der-Waals and electrostatic interaction above the Fe atoms and Pauli repulsion in-between the Fe atoms. DFT calculations suggested that the Pauli repulsion in-between the Fe atom at the corner and edge of the Fe clusters is a result of an increased electron charge density in-between the Fe cluster's atoms. However, the atomic contrast within the center of the Fe cluster ($c^* = 6$) is again a result of the CO tip's transition from physi- to chemisorption when approaching the individual Fe atoms of the Fe cluster's center.

Finally, the time dependence of the appearance of small Fe clusters in atomically resolved $\Delta f(x, y)$ images was studied. Over time, repulsive features evolve on small Fe clusters if the microscope head was exposed to low temperatures for a couple of weeks. As the amount of molecular hydrogen (H_2) increases with the time the microscope is subjected to low temperatures, the appearance of repulsive features was attributed to the adsorption of hydrogen on the investigated Fe clusters. However, the experiments did not reveal whether molecular (H_2) or atomic (H) hydrogen adsorbed on the Fe cluster. The latter could be a result of the dissociation of H_2 to atomic hydrogen due to the catalytic properties of small Fe clusters. Future research, mainly in the form of theoretical calculations, is required to clarify this open issue.

A. Appendix

A.1. Full Frequency Shift Dataset During the Lateral Manipulation of a Single Fe Adatom Using a Mononoatomic Metal and a CO-Terminated Tip

Figures 4.3 (a) and (d) in chapter 4 show selected $\Delta f(x_{\mathrm{A}}, z)$ curves recorded above a single Fe adatom using a monoatomic metal and a CO tip, respectively. The corresponding full $\Delta f\,(x_{\mathrm{A}}, z)$ datasets are shown in Fig. A.1 (a) and (b), respectively.

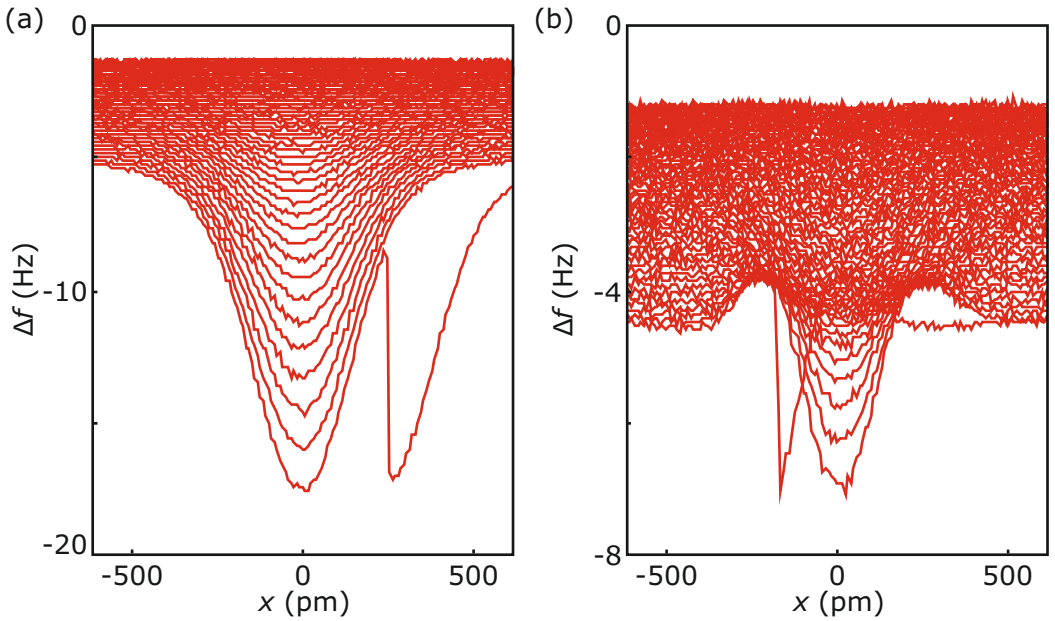

Figure A.1. Full $\Delta f\,(x_{\mathrm{A}}, z)$ dataset above a single Fe adatom using (a) a monoatomic metal tip and (b) a CO-terminated monoatomic metal tip corresponding to Fig. 4.3(a) and (d) in chapter 4, respectively. Figure adapted from [82].

A.2. Atomically Resolved Frequency Shift Images of Various Atom-by-Atom Assembled Fe Clusters

Figure 5.7 in chapter 5 shows various $F_{z,\mathrm{SR}}(z, c^*)$ curves which are recorded above the individual Fe atoms of different atom-by-atom assembled Fe clusters. The corresponding Fe clusters are atomically resolved in constant current-mode using CO tips 2 to 4. The corresponding $\Delta f(x, y)$ images are depicted in Fig. A.2.

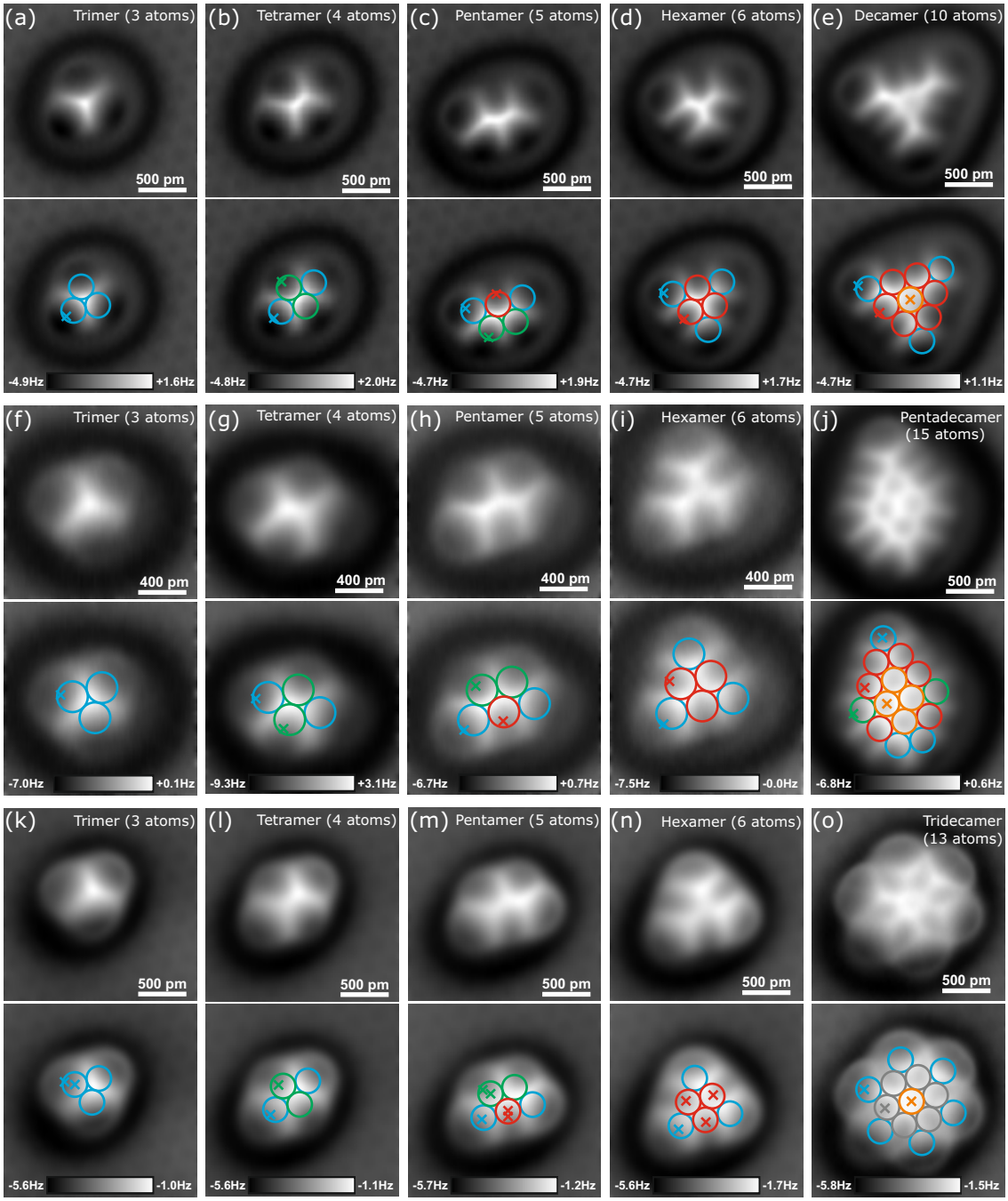

Figure A.2. Corresponding atomically resolved $\Delta f(x, y)$ images of various Fe clusters (top panels) including the atomic positions (colored circles) and the (x, y) locations (colored crosses, bottom panels) of the $F_{z,\mathrm{SR}}(z, c^*)$ curves which are depicted in Fig. 5.7 of chapter 5. Panels (a)-(e), (f)-(j) and (k)-(o) correspond to CO tip 2, 3 and 4, respectively. Imaging parameters: [CO tip 2] (a)-(e) $V_{\mathrm{tip}} = -1\,\mathrm{mV}$, $\langle I \rangle = 80\,\mathrm{pA}$, $A = 50\,\mathrm{pm}$; [CO tip 3] (f)-(j) $V_{\mathrm{tip}} = -1\,\mathrm{mV}$, $\langle I \rangle = 110\,\mathrm{pA}$, $A = 10\,\mathrm{pm}$ except $\langle I \rangle = 100\,\mathrm{pA}$ for panel (f) and $A = 10\,\mathrm{pm}$ for panel (j); [CO tip 4] (k)-(o) $V_{\mathrm{tip}} = -1\,\mathrm{mV}$, $\langle I \rangle = 100\,\mathrm{pA}$, $A = 50\,\mathrm{pm}$. Note that the high-symmetry direction of the substrate is rotated by 15° anti-clockwise with respect to the horizontal axis. Figure adapted from [106].

A.3. Energy versus Distance Spectroscopy on Individual Fe Atoms of Small Fe Clusters

Figure 5.7 in chapter 5 shows various $F_{z,\mathrm{SR}}(z, c^*)$ curves which are recorded above the individual Fe atoms of different Fe clusters. The corresponding $E_{\mathrm{SR}}(z, c^*)$ spectra recorded with CO tips 2 to 4 are depicted in Fig. A.3.

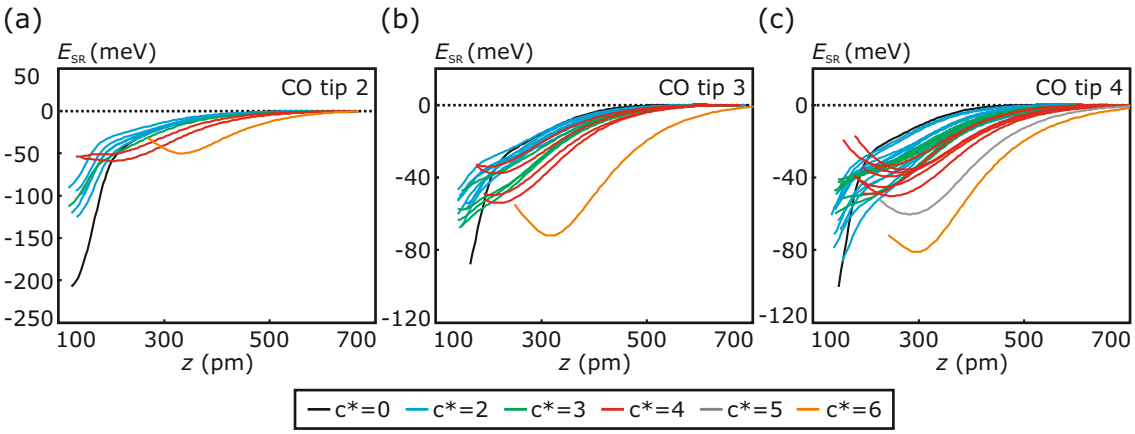

Figure A.3. Corresponding short-range energy versus distance curves $E_{\mathrm{SR}}(z, c^*)$ above individual Fe atoms of different Fe clusters to the $F_{z,\mathrm{SR}}(z, c^*)$ spectra depicted in Fig. 5.7 of chapter 5. The color of the individual curves indicates the reduced coordination number c^* of the investigated cluster's Fe atom. Figure adapted from [106].

List of Publications

All publications to which the author was contributing as first or co-author are presented in the following list.

- F. Pielmeier, G. Landolt, B. Slomski, S. Muff, J. Berwanger, A. Eich, A. A. Khajetoorians, J. Wiebe, Z. S. Aliev, M. B. Babanly, R. Wiesendanger, J. Osterwalder, E. V. Chulkov, F. J. Giessibl, and J. H. Dil: *Response of the topological surface state to surface disorder in $TlBiSe_2$*, New Journal of Physics **17**, 23067 (2015)

- J. Berwanger, F. Huber, F. Stilp, and F. J. Giessibl: *Lateral manipulation of single iron adatoms by means of combined atomic force and scanning tunneling microscopy using CO-terminated tips*, Physical Review B **98**, 195409 (2018)

- F. Huber, J. Berwanger, S. Polesya, S. Mankovsky, H. Ebert, and F. J. Giessibl: *Chemical bond formation showing a transition from physisorption to chemisorption*, Science **366**, 235 (2019)

- J. Berwanger, S. Polesya, S. Mankovsky, H. Ebert, and F. J. Giessibl: *Atomically Resolved Chemical Reactivity of Small Fe Clusters*, Physical Review Letters **124**, 096001 (2020)

Bibliography

[1] G. Binnig, H. Rohrer, C. Gerber and E. Weibel: *Tunneling through a controllable vacuum gap*, Appl. Phys. Lett. **40**, 178 (1982)

[2] G. Binnig and H. Rohrer: *Scanning tunneling microscopy*, Surf. Sci. **126**, 236 (1983)

[3] G. Binnig, C. F. Quate and C. Gerber: *Atomic Force Microscope*, Phys. Rev. Lett. **56**, 930 (1986)

[4] T. R. Albrecht, P. Grütter, D. Horne and D. Rugar: *Frequency modulation detection using high-Q cantilevers for enhanced force microscope sensitivity*, J. Appl. Phys. **69**, 668 (1991)

[5] F. J. Giessibl: *High-speed force sensor for force microscopy and profilometry utilizing a quartz tuning fork*, Appl. Phys. Lett. **73**, 3956 (1998)

[6] D. M. Eigler and E. K. Schweizer: *Positioning single atoms with a scanning tunneling microscope*, Nature **344**, 524 (1990)

[7] J. A. Stroscio and D. M. Eigler: *Atomic and Molecular Manipulation with the Scanning Tunneling Microscope*, Science **254**, 1319 (1991)

[8] L. Bartels, G. Meyer and K.-H. Rieder: *Basic Steps of Lateral Manipulation of Single Atoms and Diatomic Clusters with a Scanning Tunneling Microscope Tip*, Phys. Rev. Lett. **79**, 697 (1997)

[9] J. A. Stroscio and R. J. Celotta: *Controlling the Dynamics of a Single Atom in Lateral Atom Manipulation*, Science **306**, 242 (2004)

[10] B. Wolter, Y. Yoshida, A. Kubetzka, S.-W. Hla, K. von Bergmann and R. Wiesendanger: *Spin Friction Observed on the Atomic Scale*, Phys. Rev. Lett. **109**, 116102 (2012)

[11] R. J. Celotta, S. B. Balakirsky, A. P. Fein, F. M. Hess, G. M. Rutter and J. A. Stroscio: *Invited article: Autonomous assembly of atomically perfect nanostructures using a scanning tunneling microscope*, Rev. Sci. Instrum. **85**, 121301 (2014)

[12] R. P. Feynman: *There's Plenty or Room at the Bottom*, Eng. Sci. **23**, 22 (1960)

[13] M. Ternes, C. P. Lutz, C. F. Hirjibehedin, F. J. Giessibl and A. J. Heinrich: *The Force Needed to Move an Atom on a Surface*, Science **319**, 1066 (2008)

[14] M. F. Crommie, C. P. Lutz and D. M. Eigler: *Confinement of Electrons to Quantum Corrals on a Metal Surface*, Science **262**, 218 (1993)

[15] M. F. Crommie, C. P. Lutz, D. M. Eigler and E. J. Heller: *Quantum corrals*, Phys. D Nonlinear Phenom. **83**, 98 (1995)

[16] M. Crommie, C. Lutz, D. Eigler and E. Heller: *Quantum interference in 2D atomic-scale structures*, Surf. Sci. **361-362**, 864 (1996)

[17] A. A. Khajetoorians, J. Wiebe, B. Chilian and R. Wiesendanger: *Realizing All-Spin-Based Logic Operations Atom by Atom*, Science **332**, 1062 (2011)

[18] A. A. Khajetoorians, J. Wiebe, B. Chilian, S. Lounis, S. Blügel and R. Wiesendanger: *Atom-by-atom engineering and magnetometry of tailored nanomagnets*, Nat. Phys. **8**, 497 (2012)

[19] G. E. Pacchioni, L. Gragnaniello, F. Donati, M. Pivetta, G. Autès, O. V. Yazyev, S. Rusponi and H. Brune: *Multiplet features and magnetic properties of Fe on Cu(111): From single atoms to small clusters*, Phys. Rev. B **91**, 235426 (2015)

[20] A. A. Khajetoorians, B. Baxevanis, C. Hübner, T. Schlenk, S. Krause, T. O. Wehling, S. Lounis, A. Lichtenstein, D. Pfannkuche, J. Wiebe and R. Wiesendanger: *Current-Driven*

Spin Dynamics of Artificially Constructed Quantum Magnets, Science **339**, 55 (2013)

[21] S. H. Phark, J. A. Fischer, M. Corbetta, D. Sander, K. Nakamura and J. Kirschner: *Reduced-dimensionality-induced helimagnetism in iron nanoislands*, Nat. Commun. **5**, 5183 (2014)

[22] A. A. Khajetoorians, D. Wegner, A. F. Otte and I. Swart: *Creating designer quantum states of matter atom-by-atom*, Nat. Rev. Phys. (2019)

[23] A. Fürstner: *Iron Catalysis in Organic Synthesis: A Critical Assessment of What It Takes To Make This Base Metal a Multitasking Champion*, ACS Cent. Sci. **2**, 778 (2016)

[24] C. Bolm, J. Legros, J. Le Paih and L. Zani: *Iron-Catalyzed Reactions in Organic Synthesis*, Chem. Rev. **104**, 6217 (2004)

[25] K. S. Egorova and V. P. Ananikov: *Which Metals are Green for Catalysis? Comparison of the Toxicities of Ni, Cu, Fe, Pd, Pt, Rh, and Au Salts*, Angew. Chemie Int. Ed. **55**, 12150 (2016)

[26] D. M. Cox, K. C. Reichmann, D. J. Trevor and A. Kaldor: *CO chemisorption on free gas phase metal clusters*, J. Chem. Phys. **88**, 111 (1988)

[27] L.-S. Wang, X. Li and H.-F. Zhang: *Probing the electronic structure of iron clusters using photoelectron spectroscopy*, Chem. Phys. **262**, 53 (2000)

[28] C. P. McNary and P. B. Armentrout: *Iron cluster–CO bond energies from the kinetic energy dependence of the* Fe_n^+ *($n = 4 - 17$) + CO association reactions*, Phys. Chem. Chem. Phys. **16**, 26467 (2014)

[29] M. D. Morse, M. E. Geusic, J. R. Heath and R. E. Smalley: *Surface reactions of metal clusters. II. Reactivity surveys with D_2, N_2, and CO*, J. Chem. Phys. **83**, 2293 (1985)

[30] H. S. Taylor: *A Theory of the Catalytic Surface*, Proc. R. Soc. A Math. Phys. Eng. Sci. **108**, 105 (1925)

[31] L. Bartels, G. Meyer and K.-H. Rieder: *Controlled vertical manipulation of single CO molecules with the scanning tunneling microscope: A route to chemical contrast*, Appl. Phys. Lett. **71**, 213 (1997)

[32] L. Gross, F. Mohn, N. Moll, P. Liljeroth and G. Meyer: *The Chemical Structure of a Molecule Resolved by Atomic Force Microscopy*, Science **325**, 1110 (2009)

[33] M. Emmrich, F. Huber, F. Pielmeier, J. Welker, T. Hofmann, M. Schneiderbauer, D. Meuer, S. Polesya, S. Mankovsky, D. Ködderitzsch, H. Ebert and F. J. Giessibl: *Subatomic resolution force microscopy reveals internal structure and adsorption sites of small iron clusters*, Science **348**, 308 (2015)

[34] N. Pavliček and L. Gross: *Generation, manipulation and characterization of molecules by atomic force microscopy*, Nat. Rev. Chem. **1**, 0005 (2017)

[35] P. Jelínek: *High resolution SPM imaging of organic molecules with functionalized tips*, J. Phys. Condens. Matter **29**, 343002 (2017)

[36] A. Extance: *How atomic imaging is being pushed to its limit*, Nature **555**, 545 (2018)

[37] M. P. Boneschanscher, S. K. Hämäläinen, P. Liljeroth and I. Swart: *Sample Corrugation Affects the Apparent Bond Lengths in Atomic Force Microscopy*, ACS Nano **8**, 3006 (2014)

[38] F. Schulz, J. Ritala, O. Krejčí, A. P. Seitsonen, A. S. Foster and P. Liljeroth: *Elemental Identification by Combining Atomic Force Microscopy and Kelvin Probe Force Microscopy*, ACS Nano **12**, 5274 (2018)

[39] M. Ellner, N. Pavliček, P. Pou, B. Schuler, N. Moll, G. Meyer, L. Gross and R. Peréz: *The Electric Field of CO Tips and Its Relevance for Atomic Force Microscopy*, Nano Lett. **16**, 1974 (2016)

[40] J. Peng, D. Cao, Z. He, J. Guo, P. Hapala, R. Ma, B. Cheng, J. Chen, W. J. Xie, X.-Z. Li, P. Jelínek, L.-M. Xu, Y. Q. Gao, E.-G.

Wang and Y. Jiang: *The effect of hydration number on the interfacial transport of sodium ions*, Nature **557**, 701 (2018)

[41] J. Peng, J. Guo, P. Hapala, D. Cao, R. Ma, B. Cheng, L. Xu, M. Ondráček, P. Jelínek, E. Wang and Y. Jiang: *Weakly perturbative imaging of interfacial water with submolecular resolution by atomic force microscopy*, Nat. Commun. **9**, 122 (2018)

[42] F. Huber, J. Berwanger, S. Polesya, S. Mankovsky, H. Ebert and F. J. Giessibl: *Chemical bond formation showing a transition from physisorption to chemisorption*, Science **366**, 235 (2019)

[43] G. Binnig, H. Rohrer, C. Gerber and E. Weibel: *Surface Studies by Scanning Tunneling Microscopy*, Phys. Rev. Lett. **49**, 57 (1982)

[44] E. C. Teague: *Room Temperature Gold-Vacuum-Gold Tunneling Experiments*, J. Res. Natl. Bur. Stand. (1934). **91**, 171 (1986)

[45] C. J. Chen: *Introduction to scanning tunneling microscopy*, Oxford University Press, New York (1993)

[46] H. B. Michaelson: *The work function of the elements and its periodicity*, J. Appl. Phys. **48**, 4729 (1977)

[47] J. Bardeen: *Tunnelling from a Many-Particle Point of View*, Phys. Rev. Lett. **6**, 57 (1961)

[48] J. Tersoff and D. R. Hamann: *Theory and Application for the Scanning Tunneling Microscope*, Phys. Rev. Lett. **50**, 1998 (1983)

[49] J. Tersoff and D. R. Hamann: *Theory of the scanning tunneling microscope*, Phys. Rev. B **31**, 805 (1985)

[50] L. Gross, N. Moll, F. Mohn, A. Curioni, G. Meyer, F. Hanke and M. Persson: *High-Resolution Molecular Orbital Imaging Using a p-Wave STM Tip*, Phys. Rev. Lett. **107**, 086101 (2011)

[51] C. J. Chen: *Theory of scanning tunneling spectroscopy*, J. Vac. Sci. Technol. A Vacuum, Surfaces Film. **6**, 319 (1988)

[52] C. J. Chen: *Tunneling matrix elements in three-dimensional space: The derivative rule and the sum rule*, Phys. Rev. B **42**, 8841 (1990)

[53] F. London: *Zur Theorie und Systematik der Molekularkräfte*, Zeitschrift für Phys. **63**, 245 (1930)

[54] T. Gould and T. Bučko: *C_6 Coefficients and Dipole Polarizabilities for All Atoms and Many Ions in Rows 1–6 of the Periodic Table*, J. Chem. Theory Comput. **12**, 3603 (2016)

[55] H. Hamaker: *The London-van der Waals attraction between spherical particles*, Physica **4**, 1058 (1937)

[56] F. J. Giessibl: *Forces and frequency shifts in atomic-resolution dynamic-force microscopy*, Phys. Rev. B **56**, 16010 (1997)

[57] B. M. Law and F. Rieutord: *Electrostatic forces in atomic force microscopy*, Phys. Rev. B **66**, 035402 (2002)

[58] W. Pauli: *Über den Zusammenhang des Abschlusses der Elektronengruppen im Atom mit der Komplexstruktur der Spektren*, Zeitschrift für Phys. **31**, 765 (1925)

[59] J. E. Jones: *On the Determination of Molecular Fields. II. From the Equation of State of a Gas*, Proc. R. Soc. A Math. Phys. Eng. Sci. **106**, 441 (1924)

[60] A. J. Weymouth, T. Hofmann and F. J. Giessibl: *Quantifying Molecular Stiffness and Interaction with Lateral Force Microscopy*, Science **343**, 1120 (2014)

[61] N. Moll, L. Gross, F. Mohn, A. Curioni and G. Meyer: *The mechanisms underlying the enhanced resolution of atomic force microscopy with functionalized tips*, New J. Phys. **12**, 125020 (2010)

[62] N. Moll, L. Gross, F. Mohn, A. Curioni and G. Meyer: *A simple model of molecular imaging with noncontact atomic force microscopy*, New J. Phys. **14**, 083023 (2012)

[63] P. Hapala, R. Temirov, F. S. Tautz and P. Jelínek: *Origin of High-Resolution IETS-STM Images of Organic Molecules with Functionalized Tips*, Phys. Rev. Lett. **113**, 226101 (2014)

[64] P. M. Morse: *Diatomic Molecules According to the Wave Mechanics. II. Vibrational Levels*, Phys. Rev. **34**, 57 (1929)

[65] F. H. Stillinger and T. A. Weber: *Computer simulation of local order in condensed phases of silicon*, Phys. Rev. B **31**, 5262 (1985)

[66] F. J. Giessibl: *Advances in atomic force microscopy*, Rev. Mod. Phys. **75**, 949 (2003)

[67] S. Morita, F. J. Giessibl and R. Wiesendanger: *Noncontact Atomic Force Microscopy*, second edition, Springer-Verlag, Berlin, Heidelberg (2009)

[68] D. S. Wastl, A. J. Weymouth and F. J. Giessibl: *Optimizing atomic resolution of force microscopy in ambient conditions*, Phys. Rev. B **87**, 245415 (2013)

[69] F. J. Giessibl: *The qPlus sensor, a powerful core for the atomic force microscope*, Rev. Sci. Instrum. **90**, 011101 (2019)

[70] F. J. Giessibl: *A direct method to calculate tip-sample forces from frequency shifts in frequency-modulation atomic force microscopy*, Appl. Phys. Lett. **78**, 123 (2001)

[71] H. Hölscher, U. D. Schwarz and R. Wiesendanger: *Calculation of the frequency shift in dynamic force microscopy*, Appl. Surf. Sci. **140**, 344 (1999)

[72] U. Dürig: *Extracting interaction forces and complementary observables in dynamic probe microscopy*, Appl. Phys. Lett. **76**, 1203 (2000)

[73] T. Seeholzer, O. Gretz, F. J. Giessibl and A. J. Weymouth: *A Fourier method for estimating potential energy and lateral forces from frequency-modulation lateral force microscopy data*, New J. Phys. **21**, 083007 (2019)

[74] J. E. Sader and S. P. Jarvis: *Accurate formulas for interaction force and energy in frequency modulation force spectroscopy*, Appl. Phys. Lett. **84**, 1801 (2004)

[75] J. Welker: *Höchstauflösende Kraftmikroskopie mit subatomar definierten Bindungszuständen*, PhD thesis, University of Regensburg (2012)

[76] J. E. Sader, B. D. Hughes, F. Huber and F. J. Giessibl: *Interatomic force laws that corrupt their own measurement,* `arXiv:1709.07571[cond-mat.mes-hall]`

[77] J. E. Sader, B. D. Hughes, F. Huber and F. J. Giessibl: *Interatomic force laws that evade dynamic measurement*, Nat. Nanotechnol. **13**, 1088 (2018)

[78] F. Huber: *Tieftemperatur- Rasterkraftmikroskopie mit funktionalisierten Spitzen an einzelnen Adatomen*, PhD thesis, University of Regensburg (2018)

[79] F. J. Giessibl, H. Bielefeldt, S. Hembacher and J. Mannhart: *Calculation of the optimal imaging parameters for frequency modulation atomic force microscopy*, Appl. Surf. Sci. **140**, 352 (1999)

[80] A. Gustafsson, N. Okabayashi, A. Peronio, F. J. Giessibl and M. Paulsson: *Analysis of STM images with pure and CO-functionalized tips: A first-principles and experimental study*, Phys. Rev. B **96**, 085415 (2017)

[81] M. Schneiderbauer, M. Emmrich, A. J. Weymouth and F. J. Giessibl: *CO Tip Functionalization Inverts Atomic Force Microscopy Contrast via Short-Range Electrostatic Forces*, Phys. Rev. Lett. **112**, 166102 (2014)

[82] J. Berwanger, F. Huber, F. Stilp and F. J. Giessibl: *Lateral manipulation of single iron adatoms by means of combined atomic force and scanning tunneling microscopy using CO-terminated tips*, Phys. Rev. B **98**, 195409 (2018)

[83] S. Polesya, S. Mankovsky and H. Ebert: *Unpublished DFT calculations (private communication), LMU Munich*, (2018-2019)

[84] M. Gajdoš and J. Hafner: *CO adsorption on Cu(111) and Cu(001) surfaces: Improving site preference in DFT calculations*, Surf. Sci. **590**, 117 (2005)

[85] Z. Majzik, M. Setvín, A. Bettac, A. Feltz, V. Cháb and P. Jelínek: *Simultaneous current, force and dissipation measurements on the Si(111) 7×7 surface with an optimized qPlus AFM/STM technique*, Beilstein J. Nanotechnol. **3**, 249 (2012)

[86] L. Nony, F. Bocquet, F. Para and C. Loppacher: *Frequency shift, damping, and tunneling current coupling with quartz tuning forks in noncontact atomic force microscopy*, Phys. Rev. B **94**, 115421 (2016)

[87] M. Ternes, C. González, C. P. Lutz, P. Hapala, F. J. Giessibl, P. Jelínek and A. J. Heinrich: *Interplay of conductance, force, and structural change in metallic point contacts*, Phys. Rev. Lett. **106**, 016802 (2011)

[88] D. Martin-Jimenez, S. Ahles, D. Mollenhauer, H. A. Wegner, A. Schirmeisen and D. Ebeling: *Bond-Level Imaging of the 3D Conformation of Adsorbed Organic Molecules Using Atomic Force Microscopy with Simultaneous Tunneling Feedback*, Phys. Rev. Lett. **122**, 196101 (2019)

[89] M. Schneiderbauer: *Aufbau eines Tieftemperatur-Ultrahochvakuum-Rasterkraftmikroskops und Messung elektrischer Multipolkräfte im Piconewton-Bereich*, PhD thesis, University of Regensburg (2014)

[90] M. Emmrich: *Subatomare Auflösung auf Adatomen und kraftfeldabhängige laterale Manipulation mit einem eigenentwickelten Tieftemperatur-Rasterkraftmikroskop*, PhD thesis, University of Regensburg (2015)

[91] F. Huber and F. J. Giessibl: *Low noise current preamplifier for qPlus sensor deflection signal detection in atomic force microscopy at room and low temperatures*, Rev. Sci. Instrum. **88**, 073702 (2017)

[92] J. Welker and F. J. Giessibl: *Revealing the Angular Symmetry of Chemical Bonds by Atomic Force Microscopy*, Science **336**, 444 (2012)

[93] T. Hofmann, F. Pielmeier and F. J. Giessibl: *Chemical and Crystallographic Characterization of the Tip Apex in Scanning Probe Microscopy*, Phys. Rev. Lett. **112**, 066101 (2014)

[94] W. L. Bragg: *XLII. The crystalline structure of copper*, London, Edinburgh, Dublin Philos. Mag. J. Sci. **28**, 355 (1914)

[95] L. Bartels, G. Meyer, K.-H. Rieder, D. Velic, E. Knoesel, A. Hotzel, M. Wolf and G. Ertl: *Dynamics of Electron-Induced Manipulation of Individual CO Molecules on Cu(111)*, Phys. Rev. Lett. **80**, 2004 (1998)

[96] H. J. Lee and W. Ho: *Single-Bond Formation and Characterization with a Scanning Tunneling Microscope*, Science **286**, 1719 (1999)

[97] A. Biedermann, W. Rupp, M. Schmid and P. Varga: *Coexistence of fcc- and bcc-like crystal structures in ultrathin Fe films grown on Cu(111)*, Phys. Rev. B **73**, 165418 (2006)

[98] N. N. Negulyaev, V. S. Stepanyuk, L. Niebergall, P. Bruno, W. Auwärter, Y. Pennec, G. Jahnz and J. V. Barth: *Effect of strain relaxations on heteroepitaxial metal-on-metal island nucleation and superlattice formation: Fe on Cu(111)*, Phys. Rev. B **79**, 195411 (2009)

[99] M. F. Crommie, C. P. Lutz and D. M. Eigler: *Imaging standing waves in a two-dimensional electron gas*, Nature **363**, 524 (1993)

[100] D. S. Wastl, M. Judmann, A. J. Weymouth and F. J. Giessibl: *Atomic Resolution of Calcium and Oxygen Sublattices of Calcite in Ambient Conditions by Atomic Force Microscopy Using qPlus Sensors with Sapphire Tips*, ACS Nano **9**, 3858 (2015)

[101] F. Pielmeier and F. J. Giessibl: *Spin Resolution and Evidence for Superexchange on NiO(001) Observed by Force Microscopy*, Phys. Rev. Lett. **110**, 266101 (2013)

[102] F. Elsner: *Untersuchung der Rauschgrenzen bei der Messung kleinster mechanischer Auslenkungen*, Diploma thesis, University of Regensburg (2010)

[103] F. Huber: *Charakterisierung und Optimierung des Auslenkungsrauschens von Vorverstärkern für piezoelektrische Kraftsensoren*, Bachelor thesis, University of Regensburg (2011)

[104] T. Hofmann: *Hochauflösende Rasterkraftmikroskopie auf Graphen und Kohlenmonoxid*, PhD thesis, University of Regensburg (2014)

[105] T. Hofmann, J. Welker and F. J. Giessibl: *Preparation of light-atom tips for scanning probe microscopy by explosive delamination*, J. Vac. Sci. Technol. B, Nanotechnol. Microelectron. Mater. Process. Meas. Phenom. **28**, C4E28 (2010)

[106] J. Berwanger, S. Polesya, S. Mankovsky, H. Ebert and F. J. Giessibl: *Atomically Resolved Chemical Reactivity of Small Fe Clusters*, Phys. Rev. Lett. **124**, 096001 (2020)

[107] M. Emmrich, M. Schneiderbauer, F. Huber, A. J. Weymouth, N. Okabayashi and F. J. Giessibl: *Force Field Analysis Suggests a Lowering of Diffusion Barriers in Atomic Manipulation Due to Presence of STM Tip*, Phys. Rev. Lett. **114**, 146101 (2015)

[108] P. Hapala, G. Kichin, C. Wagner, F. S. Tautz, R. Temirov and P. Jelínek: *Mechanism of high-resolution STM/AFM imaging with functionalized tips*, Phys. Rev. B **90**, 085421 (2014)

[109] J. Berwanger: *Manipulation und Inspektion von Eisen-Adatomen mittels Rastersondenmikroskopie im Ultrahochvakuum bei tiefen Temperaturen*, Master thesis, University of Regensburg (2015)

[110] J. Welker, A. J. Weymouth and F. J. Giessibl: *The Influence of Chemical Bonding Configuration on Atomic Identification by Force Spectroscopy*, ACS Nano **7**, 7377 (2013)

[111] R. Smoluchowski: *Anisotropy of the Electronic Work Function of Metals*, Phys. Rev. **60**, 661 (1941)

[112] J. E. Lennard-Jones: *Cohesion*, Proc. Phys. Soc. **43**, 461 (1931)

[113] I. Horcas, R. Fernández, J. Gómez-Rodríguez, J. Colchero, J. Gómez-Herrero and M. Baro: *WSXM: a software for scanning probe microscopy and a tool for nanotechnology.*, Rev. Sci. Instrum. **78**, 013705 (2007)

[114] F. Stilp: *Aufbau von Clustern aus einzelnen Eisenatomen und deren Charakterisierung mit einem Tieftemperatur-Rastersondenmikroskop mit CO-terminierter Spitze*, Bachelor thesis, University of Regensburg (2018)

[115] J. Repp, G. Meyer, K.-H. Rieder and P. Hyldgaard: *Site Determination and Thermally Assisted Tunneling in Homogenous Nucleation*, Phys. Rev. Lett. **91**, 206102 (2003)

[116] Z. Sun, M. P. Boneschanscher, I. Swart, D. Vanmaekelbergh and P. Liljeroth: *Quantitative Atomic Force Microscopy with Carbon Monoxide Terminated Tips*, Phys. Rev. Lett. **106**, 046104 (2011)

[117] M. T. Kief and W. F. Egelhoff: *Growth and structure of Fe and Co thin films on Cu(111), Cu(100), and Cu(110): A comprehensive study of metastable film growth*, Phys. Rev. B **47**, 10785 (1993)

[118] D. H. Everett: *Manual of Symbols and Terminology for Physicochemical Quantities and Units, Appendix II: Definitions, Terminology and Symbols in Colloid and Surface Chemistry*, Pure Appl. Chem. **31**, 577 (1972)

[119] M. Nič, J. Jirát, B. Košata, A. Jenkins and A. McNaught (Editors): *IUPAC Compendium of Chemical Terminology*, IUPAC, Research Triagle Park, NC, USA (2009)

[120] J. G. Calvert: *Glossary of atmospheric chemistry terms (Recommendations 1990)*, Pure Appl. Chem. **62**, 2167 (1990)

[121] F. Mohn, B. Schuler, L. Gross and G. Meyer: *Different tips for high-resolution atomic force microscopy and scanning tunneling microscopy of single molecules*, Appl. Phys. Lett. **102**, 073109 (2013)

[122] S. K. Hämäläinen, N. van der Heijden, J. van der Lit, S. den Hartog, P. Liljeroth and I. Swart: *Intermolecular Contrast in Atomic*

Force Microscopy Images without Intermolecular Bonds, Phys. Rev. Lett. **113**, 186102 (2014)

[123] M. Neu, N. Moll, L. Gross, G. Meyer, F. J. Giessibl and J. Repp: *Image correction for atomic force microscopy images with functionalized tips*, Phys. Rev. B **89**, 205407 (2014)

[124] M. Corso, M. Ondráček, C. Lotze, P. Hapala, K. J. Franke, P. Jelínek and J. I. Pascual: *Charge Redistribution and Transport in Molecular Contacts*, Phys. Rev. Lett. **115**, 136101 (2015)

[125] Y. Sugimoto, P. Pou, M. Abe, P. Jelinek, R. Pérez, S. Morita and Ó. Custance: *Chemical identification of individual surface atoms by atomic force microscopy*, Nature **446**, 64 (2007)

[126] C. Wagner, M. F. B. Green, P. Leinen, T. Deilmann, P. Krüger, M. Rohlfing, R. Temirov and F. S. Tautz: *Scanning Quantum Dot Microscopy*, Phys. Rev. Lett. **115**, 026101 (2015)

[127] C. Wagner, M. F. B. Green, M. Maiworm, P. Leinen, T. Esat, N. Ferri, N. Friedrich, R. Findeisen, A. Tkatchenko, R. Temirov and F. S. Tautz: *Quantitative imaging of electric surface potentials with single-atom sensitivity*, Nat. Mater. **18**, 853 (2019)

[128] J. Repp: *private communication, University of Regensburg* (2019)

[129] T. L. Cottrell: *The Strength of Chemical Bonds*, Butterworths Scientific Publications, London (1954)

[130] S. W. Benson: *Bond energies*, J. Chem. Educ. **42**, 502 (1965)

[131] K. Christmann: *Interaction of hydrogen with solid surfaces*, Surf. Sci. Rep. **9**, 1 (1988)

[132] F. Natterer, F. Patthey and H. Brune: *Quantifying residual hydrogen adsorption in low-temperature STMs*, Surf. Sci. **615**, 80 (2013)

[133] A. A. Khajetoorians, M. Valentyuk, M. Steinbrecher, T. Schlenk, A. Shick, J. Kolorenc, A. I. Lichtenstein, T. O. Wehling,

R. Wiesendanger and J. Wiebe: *Tuning emergent magnetism in a Hund's impurity*, Nat. Nanotechnol. **10**, 958 (2015)

[134] J. A. Gupta, C. P. Lutz, A. J. Heinrich and D. M. Eigler: *Strongly coverage-dependent excitations of adsorbed molecular hydrogen*, Phys. Rev. B **71**, 115416 (2005)

[135] M. B. Knickelbein, G. M. Koretsky, K. A. Jackson, M. R. Pederson and Z. Hajnal: *Hydrogenated and deuterated iron clusters: Infrared spectra and density functional calculations*, J. Chem. Phys. **109**, 10692 (1998)

[136] K. Takahashi, S. Isobe and S. Ohnuki: *Chemisorption of hydrogen on Fe clusters through hybrid bonding mechanisms*, Appl. Phys. Lett. **102**, 113108 (2013)

[137] R. Temirov, S. Soubatch, O. Neucheva, A. C. Lassise and F. S. Tautz: *A novel method achieving ultra-high geometrical resolution in scanning tunnelling microscopy*, New J. Phys. **10**, 053012 (2008)

[138] C. Weiss, C. Wagner, C. Kleimann, M. Rohlfing, F. S. Tautz and R. Temirov: *Imaging Pauli Repulsion in Scanning Tunneling Microscopy*, Phys. Rev. Lett. **105**, 086103 (2010)

[139] C. Weiss, C. Wagner, R. Temirov and F. S. Tautz: *Direct Imaging of Intermolecular Bonds in Scanning Tunneling Microscopy*, J. Am. Chem. Soc. **132**, 11864 (2010)

[140] E. K. Parks, K. Liu, S. C. Richtsmeier, L. G. Pobo and S. J. Riley: *Reactions of iron clusters with hydrogen. II. Composition of the fully hydrogenated products*, J. Chem. Phys. **82**, 5470 (1985)

Acknowledgment

At first, I want to thank my supervisor Prof. Dr. Franz J. Gießibl for giving me the opportunity to conduct fabulous fundamental research within his group. Furthermore I would like to thank him for giving me a free hand regarding the selection of experiments, for inspiring me both scientifically and personally and for enabling my research stay abroad. I really enjoyed working with such an enthusiastic, motivating and inspiring personality.

I would like to thank Prof. Dr. Rupert Huber for the second expertise on this thesis and for being an excellent lecturer during my undergraduate studies.

I was very happy that I got invited by Dr. Joseph A. Stroscio to work for five months in his sophisticated *Advances Measurement Laboratory* at the National Institute of Standards and Technology in Gaithersburg (USA). It was a delight to work with Dr. Johannes Schwenk, Dr. Sungmin Kim and Dr. William G. Cullen during the realization of the combined STM/AFM allowing measurements at 10 mK and up to 15 T. Furthermore I would like to thank Dr. Fereshte Ghahari and Dr. Daniel Walkup for their support during my research stay.

Special thanks are due to my office mate Dr. Ferdinand Huber: it was a pleasure to work with him in the team "LT2". I attained significant scientific and non-scientific knowledge through the teamwork with him and it will be hard to find such a colleague in the future.

Dr. Sonia Matencio, thank you for broadening my knowledge regarding chemical physics and physical chemistry and, furthermore, for being an unique member of the team "LT2" for a couple of years.

I would like to appreciate the immense work of Svitlana Polesya, Dr. Sergiy Mankovsky and Prof. Dr. Hubert Ebert who conducted the time-consuming DFT calculations which crucially helped to understand the experimental data on single Fe adatoms and small Fe clusters.

Furthermore I would like to thank Alexander Liebig, Korbinian Pürckhauer, Dominik Kirpal and Oliver Gretz for the pleasant scientific and non-scientific discussions and their great cooperativeness.

I want to thank Dr. Jay A. Weymouth for the recurrent discussions regarding various scientific topics and problems and, additionally, for the challenges on the squash court.

Thank you Petra Wild for taking care of all the paperwork including employment contracts, orders and much more of what I am not even aware of.

Additionally, I thank all permanent and temporal colleagues including visiting scientists from the group of Prof. Gießibl for the pleasant atmosphere and working environment.

I am forever grateful for the support of my whole family during my education. Special gratitude goes to my sister Anna, my brother Sebastian and, particularly, my mother Regine. You are the best! Finally I thank my girlfriend Marietheres for her unique support and encouragement: together, we celebrated the ups and she significantly softened the downs which occurred during the time of my graduation. Thank you so much!